To the Graduate Council:

I am submitting herewith a dissertation written by Jonathan D. Moore entitled "The Rheology of Chain Molecules Under Shear." I have examined the final copy of this dissertation for form and content and recommend that it be accepted in partial fulfillment of the requirements for the degree of Doctor of Philosophy, with a major in Chemical Engineering.

Peter T. Cummings, Major Professor

We have read this dissertation
and recommend its acceptance:

Accepted for the Council:

Associate Vice Chancellor and
Dean of The Graduate School

THE RHEOLOGY OF CHAIN MOLECULES UNDER SHEAR

A Dissertation
Presented for the
Doctor of Philosophy
Degree
The University of Tennessee, Knoxville

Jonathan D. Moore
December 1999

ACKNOWLEDGEMENTS

I must express enormous gratitude to my advisor Peter Cummings for the tremendous example, guidance, and insight that he has supplied me during my time of graduate study. He has truly played an instrumental role in each of the successes with which I have been blessed during my time at the University of Tennessee. I am also very grateful for his easy-going, approachable personality that attracted me to UT despite my ignorance of his scientific prowess and made my interactions with him these past five years extremely enjoyable. I also owe many thanks to Hank Cochran and Shengting Cui who were both intimately involved in guiding my research and from whose knowledge and skill I have benefited greatly. I would also like to thank Mark Dadmun for many helpful discussions regarding my research as well as the members of my committee, Paul Phillips and Charlie Moore. Teresa Finchum, our office supervisor, has helped me on many, many more occasions than I could even begin to count or remember. I am also very thankful for the advice and help I received from Phil LoCascio on many occasions as well as for my interactions with Ariel Chialvo and András Baranyai, from both of whom I had the opportunity to learn. During my time at UT, I had the opportunity to interact scientifically and socially with a multitude of post-docs and students. I have especially fond memories of courses taken early in my graduate career with Jason Zielke as well as many hours spent in the lab with Sunil Gupta and Sumeet Salaniwal. I also must thank the National Science Foundation for supporting my graduate studies in the form of a graduate fellowship as well as the Center for Compuatational Sciences at Oak Ridge National Lab, the National Energy Research Scientific Computing Center at Lawrence Berkeley National Lab, and Cray Research in Eagan, MN, for the generous allocations of supercomputer time that

made my research possible. Finally, special thanks are due my family: to my parents who set me on the academic course that culminates in this achievement and to my wife for all the support and encouragement she has provided (and for being "nerdy" enough to do Differential Equations homework with me on Friday nights when we were dating). I thank God for putting each of these people in my life and for blessing me with the abilities and opportunities that have made my success possible.

ABSTRACT

The rheology of chain molecules is a subject that comprises a wide variety of complex physical phenomena, challenging scientific questions, and fundamentally important practical applications. Computer simulation, molecular dynamics in particular, is a powerful tool to provide insight into these subjects on a molecular level. In this work, nonequilibrium molecular dynamics (NEMD) is employed to study linear and branched alkane chains in the melt state under transient and steady-state shearing conditions. This study focuses on three isomers of $C_{30}H_{62}$ (n-triacontane, squalane, and 9-n-octyldocosane) as well as a linear short-chain polyethylene ($C_{100}H_{202}$). A transferable united atom potential is used to model these alkane chains, and the simulations of planar Couette flow are performed using the SLLOD algorithm and a multitimestep simulation technique implemented on massively parallel computer architectures. The strain rates studied in this work (10^8-10^{12} s^{-1}) are extremely difficult to study experimentally yet typical of the severe conditions commonly found in engines and other machinery.

Compared to experiment, NEMD and the united atom model underpredict the kinematic viscosities of n-triacontane and 9-n-octyldocosane but accurately predict the values for squalane (within 15%) at temperatures of 311 and 372 K. In addition, the predicted kinematic viscosity index values for both 9-n-octyldocosane and squalane are in quantitative agreement with experiment and represent the first such predictions by molecular simulation. Thus, this same general potential model and computational approach can be used to predict this important lubricant property for potential lubricants prior to their synthesis, offering the possibility of simulation-guided lubricant design.

Simulations of $C_{100}H_{202}$ under steady-state shearing conditions reveal a pronounced

minimum in the hydrostatic pressure at an intermediate strain rate that is associated with a minimum in the intermolecular potential energy as well as transitions in the strain-rate-dependent behavior of several other viscous and structural properties of the system. Upon onset of shear, the stress overshoot curves calculated for C_{100} are in good quantitative agreement with Doi-Edwards theory if the terminal relaxation time is assumed to have the same strain-rate dependence as the calculated self-diffusion coefficient in the flow direction. This shear-enhanced diffusion offers a possible mechanism for strain-rate-dependent relaxation times in the fast flows of polymers.

Contents

List of Tables

List of Figures

Chapter 1

Introduction

Chain molecules, that is molecules whose basic molecular architecture consists of a large number of relatively small sub-units united together like links in a chain, have been the subject of numerous experimental and theoretical studies over the past several decades. With length and time scales that can range over many orders of magnitude, they pose challenging questions of not only fundamental science but also of practical interest in terms of the design and production of technologically important polymeric materials. In particular, a comprehensive understanding of the rheological behavior of chain molecules would be extremely valuable in a multitude of practical applications ranging from the design of advanced automobile engine lubricants to the improvement of techniques for polymer processing. Polymeric liquids are known to exhibit a wide variety of interesting responses to shear flow and deformation including shear thinning, shear-induced ordering, stress overshoot upon onset of shear, normal stress differences, and elastic recoil upon cessation of shear. Though clearly crucial to the behavior of a polymer melt or solution in many practical situations, these complex phenomena remain in need of more complete understanding and explanation.

Computer simulation, molecular dynamics in particular, is a powerful tool to be used to help shed light on these problems.

In a molecular dynamics (MD) simulation [3], the non-linear ordinary differential equations of motion for the dynamics of the molecules of interest are solved using standard numerical methods for initial-value problems, and the phase-space trajectories of the molecules are calculated as a function of time. The input to an MD simulation is typically the set of initial positions and momenta of the molecules, the parameters specifying the system's thermodynamic state (e.g. density and temperature), and the force fields governing the molecules' intramolecular and intermolecular interactions. During the course of the simulation, the thermophysical properties (such as pressure, energy, and viscosity) are calculated as time averages from microscopic expressions given in terms of the positions and momenta of the individual molecules. This ability to directly observe and study the dynamical behavior of individual molecules and thus gain molecular-level insight into a system's behavior is the key advantage of an MD simulation over analytic theory and many types of macroscopic experimental measurements. On the other hand, this necessity to accurately calculate the phase-space trajectories of each individual molecule in an MD simulation makes realistic MD studies of chain molecules in most cases challenging and in some cases impossible.

Consider the implications [4, 5] of the range of polymeric length and time scales. Unlike simple fluids far from phase transition which are homogeneous on a length scale of order 10 Å, polymeric liquids possess length scales several orders of magnitude larger. Lengths relevant to a single chain molecule in a system far from the critical point might range from a single chemical bond ($\sim$ 1 Å) to the persistence length ($\sim$ 10 Å) to the coil radius ($\sim 10^2$ Å). For a collection of such molecules in a dense solution or melt, lengths of order 10^3 Å and larger can become relevant. Since the simulation box must be larger than the system's longest characteristic length, many problems would

necessitate system sizes of 10^6 atoms or more. Equilibration of systems containing such a huge number of particles [6, 7] is possible for simple fluids at states far from phase transitions since fluctuations decay on picosecond timescales. This is not the case for chain molecules. For short, unentangled chains the relaxation time scales as the square of the number of sub-units [8]. Thus, even for chains of modest length, equilibration times can reach into the tens to hundreds of nanoseconds. Since the MD timestep must be much smaller than the system's shortest characteristic time (bond vibrations, $\sim 10^{-13}$ s or less for carbon-carbon bonds), 10^6-atom simulations covering timescales on the order of tens of nanoseconds are too computationally expensive to be practical. Phenomena occurring on even longer timescales are inaccessible to atomistic dynamical simulations.

In order to avoid these pitfalls in the dynamic simulation of polymeric systems, several different strategies are commonly used which involve some combination of smaller system sizes, shorter time scales, simplified polymer models, and coarse-grained simulation techniques. Rather than studying a many-chain system, one might choose to study the behavior of a single chain with length of order $N = 1000$ (where N is the number of monomeric units). Instead of simulating molecules of true polymeric length in atomistic detail, researchers often choose to study their oligomeric counterparts, typically in the range $C_4 - C_{30}$, in order to elucidate principles applicable to both the oligomer and polymer. The choice of the molecular potential model itself also has an effect on the system size. Explicit-atom (EA) potential models explicitly account for each and every atom (including hydrogens) that make up the chain molecules. At certain state conditions (i.e. reasonably high temperature), nanosecond EA simulations of chain-molecule melts with N up to 100 have been performed. However, most often some degree of coarse-graining is introduced into the molecular model, choosing computational savings at the expense of complete atomistic detail. In a united-atom

(UA) potential model, some number of atoms are collapsed into a single interaction site, thereby reducing the total number of sites in the simulation. For example, in a UA model for alkanes, each carbon and its attached hydrogens are treated as a single site. Such a model is still atomistically detailed with respect to the carbon atoms but not with respect to the hydrogens. In order to further reduce computational demands, additional model simplifications are often made, including the use of rigid bond lengths and bond angles or the restriction of the chains to a lattice. The concept of a UA model is carried one step further in bead-spring models. In such models, each site is taken to represent a number of units of the real polymer (typically 20 monomers or more) and serves as a center of hydrodynamic or systematic forces. The spring (typically with some upper limit on extensibility) connecting two such sites represents the chains' internal degrees of freedom. Bead-spring models of chain molecules are used in conjunction with both molecular dynamics simulations of dense melts and Brownian dynamics (BD) [9, 10] simulations of dilute polymer solutions, an example of a coarse-grained simulation technique. In the BD simulations, the solvent is treated as a continuous background which interacts with the polymer chains via viscous drag and stochastic forces that mimic collisions between the polymer and the solvent.

This introductory discussion of models is not intended to be comprehensive but rather to give a flavor of the balance that must be made when modeling chain molecules. On one extreme, one could employ a molecular model of such atomistic detail and realism that it becomes unfeasible to study a system on any but the shortest of time and length scales. On the other extreme, one could simplify the molecular model to such a degree that, though it requires much less CPU time to simulate, it no longer retains enough atomistic detail and complexity to accurately reproduce the phenomena of interest or provide any insight into the behavior of the

real-world molecules. For each application, one must choose the model and simulation technique that best balances these considerations. Let us now introduce several important applications to which the rheology of chain molecules is germane.

An understanding of the relationship between chemical structure and lubricant performance is highly desirable from both a fundamental and a practical perspective. From the standpoint of fundamental science, making the connection between microscopic and macroscopic properties is always an area of keen interest. In practical terms, such knowledge is crucial both to improve the performance of mineral oils and to guide the design of synthetic lubricants, driven by both long-term and contemporary motivations. Though they still make up less than five percent of the total lubricant market, demand for synthetics is increasing for many present-day applications because they provide greater stability and reliability leading to less wear on machinery and longer intervals between oil changes [11]. In addition, advances in automotive engine design to ensure improved efficiency and reduced emissions are expected to make severe demands on lubricants in the form of higher operating temperatures and, perhaps, higher strain rates, demands which most lubricants currently on the market will be unable to meet.

Since alkanes of intermediate molecular size ($C_{20} - C_{40}$) are the main constituents of lubricant basestocks, their rheological properties are of great concern in industrial lubricant applications. Certain general trends in the structure-property relationships of these molecules are well known. For example, though the viscosities of the straight chain paraffins vary little with temperature (a basic characteristic of a good lubricant), they are solids at room temperature. For this reason, most of the linear alkanes are removed from base oils during refining to improve their low-temperature performance. Much of what is known about the structure-property relationships of alkanes is based on API Research Project 42, a database containing physical properties of 273

pure hydrocarbons [2]. Among other properties, it contains viscosity measurements at a variety of temperatures for most of the 273 compounds and has been used to parameterize equations for correlation and prediction such as the viscosity-temperature equations by Mehrotra [12] and the model for zero-shear viscosity parameterized by Yahsi [13]. In addition to viscosity, viscosity index (viscosity-temperature behavior), flash point (high temperature behavior), and pour point (low temperature behavior) are the most important properties of a lubricant [14]. Denis analyzed the data in API 42 in an attempt to identify which molecular structures tend to provide the best compromise between the desirable properties of high viscosity index (minimal variation of viscosity with temperature) and low pour point [1]. Though the amount of data contained in API 42 is certainly extensive, it by no means provides a complete picture. In fact, of the greater than four billion possible alkanes containing thirty carbons, only two are represented in API 42. Hence, there appears to be insufficient data to predict how the details of molecular structure (such as the structural variation illustrated in Figure 1.1) will affect lubricant properties short of synthesis, formulation, and testing. Such a process is expensive and time-consuming.

Molecular simulation is emerging as an ideal alternative. Given a transferable intermolecular potential and a working molecular dynamics code of sufficient generality, only a few lines of code are necessary for the virtual synthesis of alkanes exhibiting any of the possible molecular architectures. Using the nonequilibrium molecular dynamics (NEMD) simulation technique [15], one may then study the strain-rate-dependent rheology of these systems. To date, most NEMD studies of the rheology of alkanes have focused on short and often linear molecules in the range $C_4 - C_{16}$ using models of varying complexity and realism. A few studies have addressed the rheology of linear alkanes in the mass range of interest. Morriss *et al.* (*n*-eicosane [16]), Travis and Evans (*n*-eicosane [17]), and Cui *et al.* (*n*-tetracosane [18]) have studied the

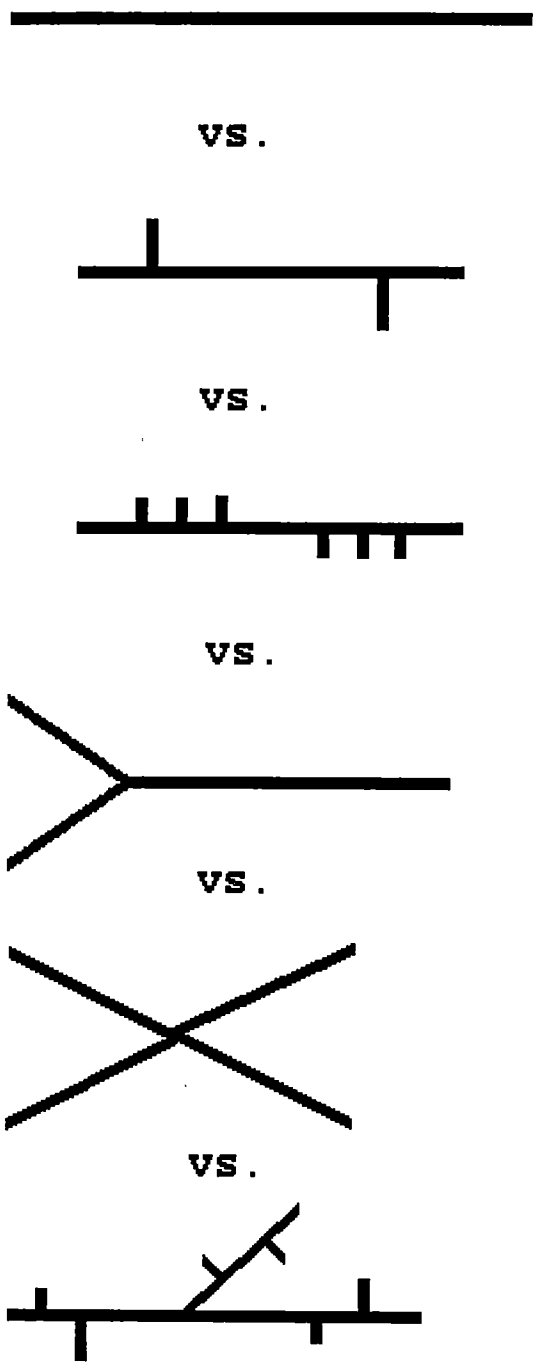

Figure 1.1: Example molecular architectures. The variation of lubricant performance with structures such as these is of both fundamental and practical interest.

behavior of molecules under shear as a function of strain rate but not temperature. Mondello and coworkers have reported the viscosity of *n*-triacontane calculated by NEMD at a single strain rate and temperature [19]. Though certainly of scientific interest, the properties of unbranched alkanes are less relevant to lubricants since most of the wax is removed from base oils, as mentioned previously. Only recently have researchers begun to use simulation to investigate the effect of branching on the rheology of alkanes of intermediate size. Mundy *et al.* (*n*-triacontane and 2,6,10,15,19,23-hexamethyltetracosane [20]) and Khare *et al.* (*n*-docosane, *n*-octacosane, and 5,12-dipropylhexadecane [21]) have compared the strain rate dependent viscosities of linear and branched alkanes at a single temperature, 450 K and 373 K respectively. Gupta and coworkers studied the rheology of confined films of *n*-tetracosane and squalane at a variety of strain-rates, temperatures, and wall spacings [22, 23, 24]. Lahtela *et al.* used NEMD to calculate the viscosities of six C_{20} isomers as a function of strain rate and temperature [25]. Though they used a somewhat inflexible model (fixed bond lengths and bond angles) and used the controversial $\dot{\gamma}^{0.5}$ extrapolation to obtain zero-shear viscosities, the general aim of their work is nevertheless admirable: a systematic study of the effect of branching on viscosity. In general, realistic study of the relevant systems ($C_{20} - C_{40}$) by molecular simulation has been limited by both high computational costs and the lack of potential models accurate over a wide range of physical conditions. However, recent advances in models [26] and algorithms [27] as well as the advent of massively parallel supercomputers have now made such studies possible. Furthermore, the severe conditions commonly found in engines and other machinery (film thickness < 1 μm, $\dot{\gamma} > 10^7$ s^{-1}, P $\simeq 10^9$ Pa [28, 29]) are extremely difficult to study experimentally and yet are quite readily accessible to simulation, NEMD in particular. In light of this, investigation by molecular simulation of the rheology of linear and branched alkanes in the mass range of interest (isomers of C_{30}

for example) is warranted, particularly if the study can probe both the Newtonian and shear-thinning regimes and include quantitative predictions of the temperature dependence of the molecules' viscosities.

We have chosen to study the effects of branching and temperature on the rheology of three C_{30} isomers: *n*-triacontane, 2,6,10,15,19,23-hexamethyltetracosane (squalane), and 9-*n*-octyldocosane. The two branched alkanes were chosen because they are the only two non-ringed isomers of C_{30} for which experimental density and viscosity data are available for comparison to and validation of our simulation results. Simulations were performed over a wide range of strain rates at the temperatures of 311 and 372 K to allow prediction of the kinematic viscosity index, a key performance measure used to categorize lubricants. Simulations for *n*-triacontane were only performed at 372 K since, experimentally, it is a solid at 311 K. In addition to the NEMD simulations, EMD simulations were performed if not already available in the literature (octyldocosane and triacontane) to provide additional data helpful in the rheological analysis.

In addition to their practical relevance to lubricant design, the rheological properties of a liquid of short, unentangled polymer chains at high shear rate also stimulate fundamental scientific interest since these properties are still not well understood. Experimental data are unavailable because of the difficulty of reaching the nonlinear viscoelastic regime in shear rate for short-chain systems. On the theoretical side, a successful theory of the rheological properties of short-chain polymers in the nonlinear regime has not been developed. The Rouse model is generally considered to provide a good description of the linear-response dynamics of short-chain polymeric systems in the liquid state [8]. This is substantiated by a large body of experimental work and molecular simulation results. Recent computer simulation studies suggest that the linear alkanes, in chain lengths of up to 100 carbon atoms, are well described

by the Rouse model, which accurately predicts the self-diffusion, segmental orientations, and equilibrium viscosity [19, 30, 31]. However, the Rouse model is essentially a linear theory with regard to the prediction of rheological properties. Its prediction of the nonlinear rheological response is qualitatively incorrect. For example, within the Rouse model, the viscosity is Newtonian at all shear rates $\dot{\gamma}$, contrary to the simulation results, where shear thinning has been observed at high shear rate. For the response to a step change from equilibrium to a constant, high shear rate (i.e., $\dot{\gamma} = 0$ for $t < 0$, $\dot{\gamma} =$ a fixed positive value for $t \geq 0$), the Rouse model predicts a linear response in both shear stress and first normal stress difference that is independent of the magnitude of shear deformation [8].

Reptation theory is generally considered to apply only to systems of high molecular weight polymers where entanglements exist [8, 32]. The well-known predictions of the theory for entangled polymeric liquids include viscoelastic behavior and the strong power law dependence of the Newtonian viscosity on the molecular weight $\eta \propto M^3$. The reptation model also predicts a well-defined transient response when a polymeric liquid is subjected to shear deformation. The original Doi-Edwards (DE) model predicts that for sufficiently high step shear start up ($\dot{\gamma}\tau_d > 2$, where τ_d is the disentanglement or reptation time), the shear stress exhibits an overshoot at a total strain $\gamma \equiv \int \dot{\gamma} dt = \dot{\gamma} t$ of about 2.0 and no overshoot in the first normal stress difference [33, 34]. An improved theory by Pearson *et al.* predicts a shear stress overshoot at a total strain of 2.3 and first normal stress overshoot at 4.3 [35]. These predictions have been corroborated by experiments [36]. Pearson *et al.* [35] provide a concise summary of the behavior of entangled polymers during the start-up of steady shearing. Recently, effort has been made by a number of authors [37, 38, 39, 40, 41, 42, 43, 44, 45] to modify DE in order to improve its predictions for various aspects of the nonlinear viscoelasticity of entangled polymer melts in general and to achieve consistency with

the empirical Cox-Merz rule in particular [37, 38, 39, 40].

These considerations motivate our interest in gaining a molecular-level understanding of the non-Newtonian rheology of alkane liquids and polymers using molecular models that preserve as much as possible of the details of the intermolecular interactions and intramolecular architecture. Molecular simulation studies of the rheology of polymeric systems have usually been limited to very small system sizes, short time-scales, simplified polymer models, and/or coarse-grained simulation techniques. Recently, equilibrium molecular dynamics (EMD) simulations of reasonably long-chain alkane liquids have been reported (e.g. $C_{100}H_{202}$) [30, 31] using the same types of realistic united atom [26, 31, 46] and explicit atom [47] potential models that have been used extensively to study shorter liquid alkanes. The demonstrated feasibility of EMD calculations on $C_{100}H_{202}$ provide impetus to perform NEMD simulations of C_{100} under various rheological tests. Such chains are long enough to be considered short polymers, yet short enough that entanglement is not expected to be a factor in their rheology. One such rheological experiment that we chose to simulate is the constant shear-rate start-up test used to study stress overshoot, a physical property which has not been studied enough experimentally or theoretically [48]. In addition to transient behavior, we have also studied the steady-state strain-rate-dependence of a variety of rheological, transport, and conformational properties of the C_{100} melt. Since EMD simulations of C_{100} using the SKS model have not been performed previously, we also studied various equilibrium properties (such as self-diffusion and orientational relaxation), though they are not the main focus of our research efforts.

Chapter 2

Literature review

Although no perfect organization of the literature of the rheology of chain molecules into exclusive categories such as experiment, analytic theory, and simulation is possible, these three categories are used to impose some structure on this review of the literature. In the following discussion, the viscosity (η), first normal stress coefficient (Ψ_1), and second normal stress coefficient (Ψ_2) are defined as usual [49, 50]

$$\eta = -\frac{\langle \sigma_{xy} \rangle}{\dot{\gamma}}, \tag{2.1}$$

$$\Psi_1 = -\frac{\langle \sigma_{xx} \rangle - \langle \sigma_{yy} \rangle}{\dot{\gamma}^2}, \tag{2.2}$$

and

$$\Psi_2 = -\frac{\langle \sigma_{yy} \rangle - \langle \sigma_{zz} \rangle}{\dot{\gamma}^2} \tag{2.3}$$

where x is the flow direction, y is the velocity gradient direction, $\dot{\gamma}$ is the strain rate characterizing the shear field, and σ is the stress tensor. The stress growth coefficients

(η^+, Ψ_1^+, and Ψ_2^+) are the time-dependent versions of these viscometric functions (η, Ψ_1, and Ψ_2) upon start-up of shear flow.

2.1 Experiments

2.1.1 Intermediate to long alkanes

In July of 1940 at The Pennsylvania State College, the American Petroleum Institute Research Project 42 began the synthesis and study of hydrocarbons of high molecular weight, primarily in the range of 25 to 60 carbons. The objectives of the project were to obtain data: 1) to allow conclusions to be made on the effect of chemical structure on physical properties, 2) to furnish data of value in identification of hydrocarbons or hydrocarbon mixtures isolated from petroleum, 3) to supply data for chemical engineering calculations on petroleum, and 4) to provide reliable methods for the preparation and purification of high molecular weight hydrocarbons.

Initial reports on the project [51, 52] were made at the API annual meetings, though U.S. entry into World War II delayed the presentation of the fourth report [53]. Results from the study were also published in journals [54, 55, 56, 57, 58] and Ph.D. theses and were summarized in a single report upon the conclusion of the project in 1966 [2]. A number of generalizations in the structure-property relationships among hydrocarbons were outlined in these various reports. For an *iso*paraffin, as the substituent chain is moved nearer the center of the molecule, the viscosity decreases rapidly while the kinematic viscosity index increases (i.e. less variation of viscosity with temperature) [51]. For the movement of a phenyl or cyclohexyl group along a 20-carbon straight chain from the end toward the center of the chain, the kinematic viscosity index decreases rapidly while the viscosity passes through a

maximum when the substituent group is at position 5 [52]. As molecular weight increases, so does viscosity and viscosity index [51]. *Iso*paraffins were also compared to napthenic and aromatic compounds. Substitution of two benzene rings for the two hexyl chains in 7-*n*-hexyleicosane doubles the viscosity while hydrogenation of these rings to napthene almost quadruples it relative to 7-*n*-hexyleicosane [51]. Multiple branching tends to lower the boiling point, density, and viscosity index [52]. Invariably, cyclization increases viscosity [52]; the effect is greater for cyclization to non-fused hydroaromatic rings than to aromatic ones. A "rule of thumb" was identified for the slope of hydrocarbon viscosity-temperature curves: the slope for a given hydrocarbon is approximately equal to the slope of the normal paraffin with the same number of carbon atoms as the longest straight chain of the hydrocarbon in question [53].

The viscosities of hydrocarbons (*iso*paraffinic, cycloparaffinic, and aromatic) and their mixtures were measured over a wide range of temperatures and pressures [56, 58]. The viscosity-temperature coefficient $1/\eta(\partial\eta/\partial T)_P$ increased with increased pressure, and the viscosity-pressure coefficient $1/\eta(\partial\eta/\partial P)_T$ decreased with increasing temperature [56]. Increased external pressure was found to enhance the changes in viscosity due to structural variations that were observed at atmospheric pressure [56]. A plot of log η versus P at constant T yielded three types of curves: 1) concave toward the pressure axis, 2) concave toward the pressure axis at low pressures then becoming linear with increasing pressure, and 3) convex toward the pressure axis over the entire pressure range. Branched paraffins exhibited behavior 1 while each of three behaviors was observed among the curves for hydrocarbons with ringed structures [58].

In addition to viscosity, viscosity index, flash point, and pour point are the most important properties of a lubricant [14]. Denis [1] examined the data in API 42 to determine the hydrocarbon structures that achieve the best compromise between the

high viscosity index and melting point. Such a choice is a compromise since, for example, *n*-alkanes tend to have both the highest viscosity index and highest melting point. Denis outlined the following generalizations: viscosity index decreases in the order *n*-alkanes > *iso*alkanes > cyclopentylalkanes > phenylalkanes > cyclohexyl alkanes, and melting point decreases as *n*-alkanes > phenylalkanes > *iso*alkanes > cyclopentylalkanes or cyclohexylalkanes. Denis highlighted the structures with viscosity index > 100 and melting point < 0 °C, typically compounds which have a long principal chain and a side chain that is highly branched or terminates in a saturated ring (see Figure 2.1), and identified schematically the hydrocarbon structures that possessed the best lubricant properties (see Figure 2.2).

Though the amount of data contained in API 42 is certainly extensive, it by no means provides a complete picture. This is illustrated by the fact that, of the greater than four billion possible alkanes containing thirty carbons, only two are represented in API 42. Hence, there appears to be insufficient data to predict how the details of molecular structure will affect lubricant properties short of additional synthesis, formulation, and testing.

In this discussion of the properties of intermediate sized hydrocarbons, the physical property called the viscosity index has been emphasized. A brief discussion of the meaning and origins of this quantity is warranted. The kinematic viscosity index (VI) is a widely-used industrial characterization of automotive lubricants. Dean and Davis proposed it as an indication of an oil's viscosity-temperature characteristics in terms of its Saybolt viscosities at 311 K (100 °F) and 372 K (210 °F) [59]. Two series of reference lubricating-oil fractions (H and L) were used for comparison. Series H exhibited little change of viscosity with temperature while the viscosities of series L oils exhibited large variation with temperature. Series H and L represented, respectively, the best and worst oils available in 1929. Series H oils were assigned a VI of

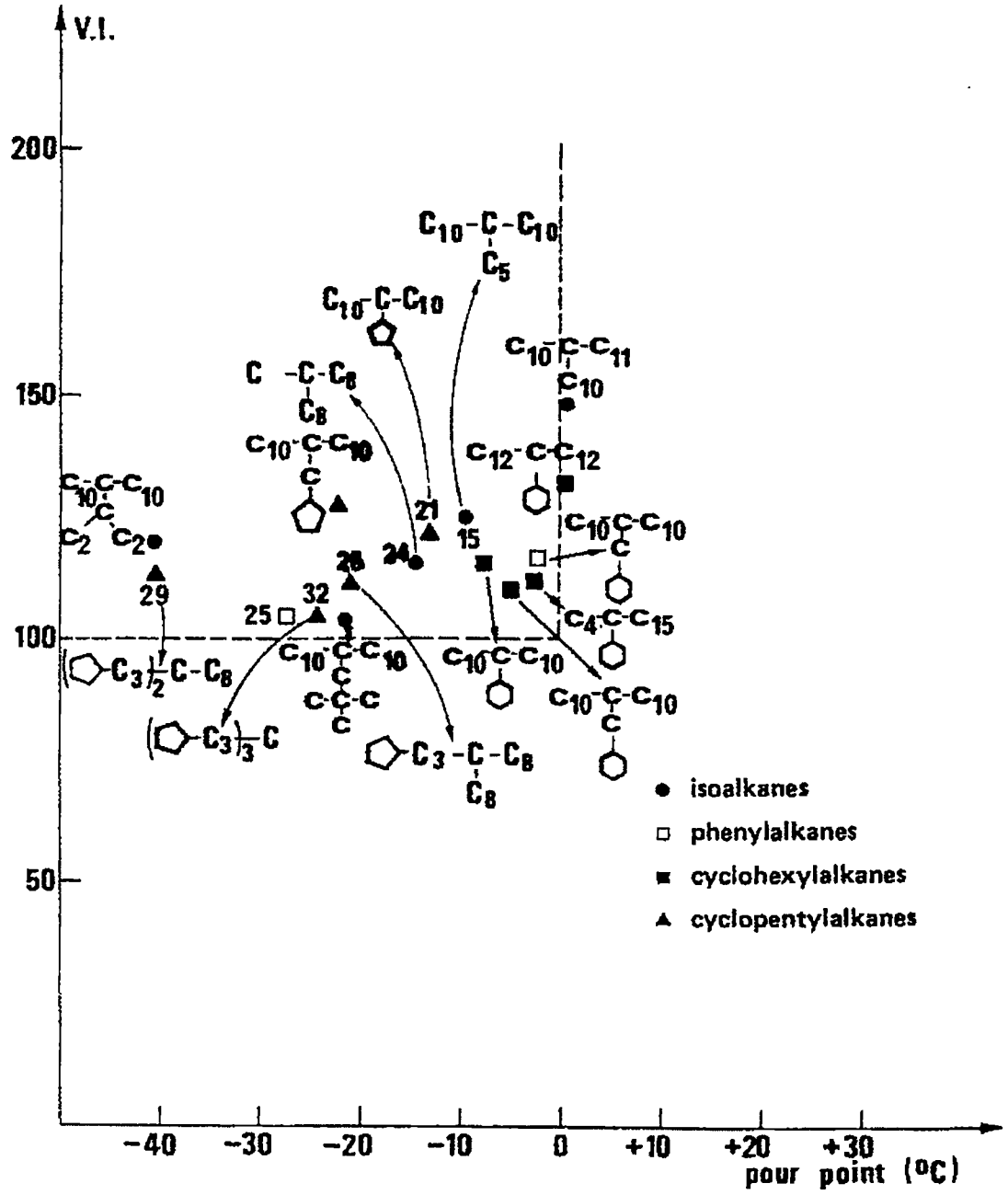

Figure 2.1: Hydrocarbons included in API 42 with viscosity index > 100 and melting point < 0 °C [1]. Although Denis labeled the abscissa as pour point, the data (from [2]) are actually melting points. Source: *Journal of Synthetic Lubrication*, 1:212, 1984.

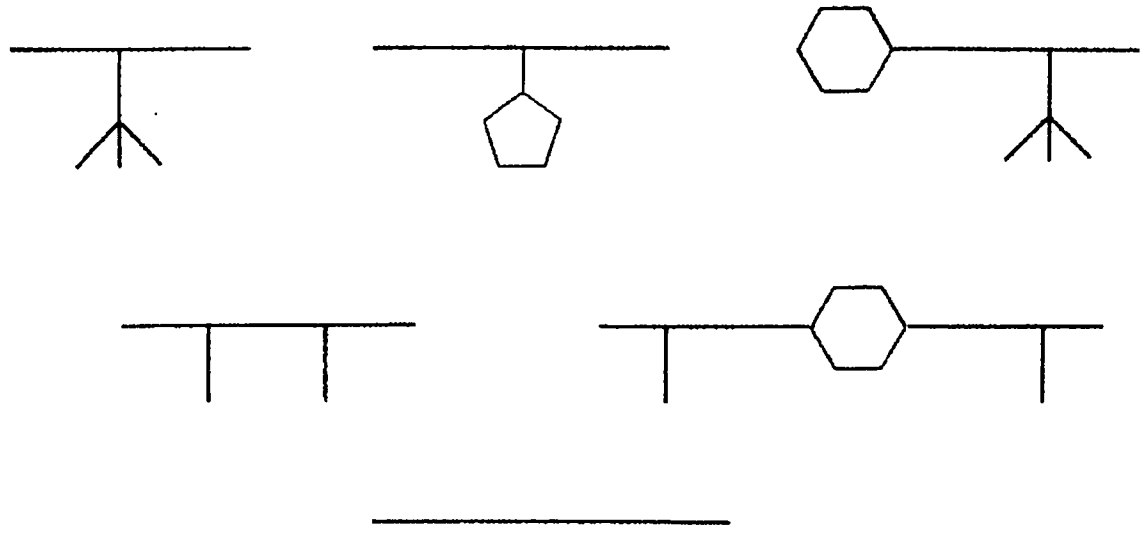

Figure 2.2: The best hydrocarbon structures, in terms of lubricant properties, as identified by Denis. Source: *Journal of Synthetic Lubrication*, 1:219, 1984.

100, series L a value of 0. The VI of an oil under test (T) was calculated from the equation

$$VI = \frac{L - U}{L - H} \text{x} 100 \tag{2.4}$$

where U is the kinematic viscosity (ν) at 311 K of the oil in question, L and H, respectively, are the kinematic viscosities at 311 K of the series L and H having the same kinematic viscosity at 372 K as the oil T. Thus, the higher the VI the less the viscosity of an oil is affected by temperature and, therefore, the better lubricant performance. Subsequently, Hardiman and Nissan [60] proposed revision to the VI system because it had reached the end of usefulness in its previous form. It had become necessary to give VI values to oils with better viscosity-temperature behavior than those represented by 100 on the VI scale. Hardiman and Nissan sought to make

the VI applicable at any two temperatures and to a wider range of oils. They reported the following empirical equation for the VI

$$VI = 3.63[60 - 10^n] \tag{2.5}$$

where n is given by

$$n = \frac{\log \nu_1 - \log k}{\log \nu_2} \tag{2.6}$$

Equation 2.6 is a rearrangement of the equation

$$\nu_1 = k\nu_2^n \tag{2.7}$$

where ν_1 is the kinematic viscosity in cSt at the lower temperature, ν_2 is the kinematic viscosity in cSt at the higher temperature, k is a function of the temperature range alone and is independent of the nature of the oil, and n, a constant characteristic for each oil, depends on the temperature range chosen. For the temperature range 311 to 372 K, Hardiman and Nissan determined k to be 2.714. They found good correlation between their suggested VI and that of Dean and Davis, theirs having the advantage of applicability to a wider range of oils. Though used subsequently in standard data compilations, such as API 42, the VI as defined by Hardiman and Nissan did not become the ASTM standard. Based on the kinematic viscosity of the oil at 313 K and 373 K, the present standard (ASTM D2270-93) is identical to that of Dean and Davis for oils with VI less than 100. A different formula, similar to the one proposed by Hardiman and Nissan, is used for oils with VI greater than 100.

2.1.2 Polymers

Though the subject of this study is the simulation of chain-molecule systems that, even in the longest case, would have to be considered only very short polymers, no experimental measurements or adequate theoretical approaches exist that treat the nonlinear viscoelastic behavior that has been routinely observed in NEMD simulations of these systems. For this reason, we will expand the scope of this literature review to include polymeric materials in general.

Pearson *et al.* measured the zero-shear viscosity (capillary flow or parallel-plate rheometer) and self-diffusion coefficient (pulsed field gradient NMR) of samples of linear polyethylene in the molecular weight range $200 < M < 120,000$ at 175 °C [61]. Below $M = 5,000$, $\eta \propto M^{1.8}$. Above $M = 5,000$, $\eta \propto M^{3.6}$. The diffusion coefficient, D, was characterized by $D \propto M^{-2}$ over the entire mass range. Correcting η according to the mass dependence of the density and radius of gyration, the product ηD agreed well with the Rouse model [62] at low M and approached the reptation model [8] from below at high M. Pearson *et al.* reported similar data for hydrogenated polybutadiene at 175 °C in the mass range 10^3 to 10^6 [63]. The authors again compared the product ηD as well as the individual values of η and D (corrected to a constant friction factor) to theory. At low M, the Rouse model agreed well with ηD, η, and D. At higher M there was evidence that relaxation mechanisms other than those considered in the Doi-Edwards model [8] made significant contributions to η and D.

Turning to properties beyond the linear regime, Menezes and Graessley studied five solutions of polybutadiene in simple shear flow [36]. Of the five, four were linear polymers with M ranging from 2×10^5 to 8×10^5, and one was a four arm star, all with narrow molecular weight distributions. They reported the stress growth coefficients η^+ and Ψ_1^+ upon onset of shear at a variety of strain rates in the range 0.108 s^{-1} to 21.4

s^{-1}. Overshoots in shear stress were observed when the product of the shear rate and the system's longest relaxation time ($\dot{\gamma}\tau_d$) exceeded a value of 1. Overshoots in normal stress were not observed until higher strain rates when the product $\dot{\gamma}\tau_R$ exceeded a value of 1 where τ_R is the Rouse relaxation time of the polymer estimated from linear viscoelastic measurements. Maxima in η^+ were observed for all five solutions, and maxima in Ψ_1^+ were observed for the linear chains but not the star molecule. In the opinion of the authors of the study, this was a consequence of the range of strain rates used rather than a fundamental difference between linear and branched chains. The startup curves were characterized by two times: t_d, the time for departure from the linear viscoelastic curve, and t_p, the time to reach the overshoot peak. The authors observed a constant departure strain of $\gamma_d = \dot{\gamma}t_d = 0.9$, in good agreement with the value of $\gamma_d = 1.0$ measure previously for a polystyrene solution [64]. In contrast, the strain at overshoot peak $\dot{\gamma}t_p$ for both shear viscosity (γ_{pS}) and first normal stress coefficient (γ_{pN}) depended on both shear rate (for $\dot{\gamma} > \tau_R^{-1}$) and solution. At low shear rates the values appeared to converge to $\gamma_{pS}^0 = 2.0 \pm 0.1$ and $\gamma_{pN}^0 = 5.0 \pm 0.2$. In similar measurements performed by Pearson *et al.* on concentrated polyisoprene solutions ($7 < M/M_e < 35$ where M_e is the molecular weight between entanglements), $\gamma_{pS}^0 = 2.3$ and $\gamma_{pN}^0 = 5.5$ [35].

Wagner and coworkers [65, 66, 67] studied a linear high-density polyethylene (HDPE) upon onset of shear and upon onset of extension. The HDPE melt was characterized by a weight-averaged molecular weight (M_W) of 104,000 g/mol and a number-averaged molecular weight (M_N) of 18,900 g/mol, and the shear rates ranged from 0.001 to 10 s^{-1} at 170 °C. Though Wagner *et al.* did not analyze the data in terms of the strain at the peak stress, the values appear to be $\gamma_{pS}^0 \approx 2$ and $\gamma_{pN}^0 \approx 20$. Wagner and coworkers observed that the HDPE sample behaved to a good approximation as a Doi-Edwards fluid under shear and a molecular stress function fluid [68]

with considerable strain hardening under extension.

In summary, the studies of Menezes and Graessley and Pearson *et al.* suggest the existence of three general regimes for the shear and normal stress overshoot of solutions of high molecular weight polymer with fairly narrow molecular weight distribution. Upon onset of shear for $\dot{\gamma} < \tau_d^{-1}$ where τ_d is the longest relaxation time in the system, η^+ and Ψ_1^+ monotonically approach their steady-state values. For $\tau_d^{-1} < \dot{\gamma} < \tau_R^{-1}$ where τ_R is the Rouse relaxation time, shear stress overshoot occurs at a strain in the range 2.0 to 2.3 independent of strain rate, no normal stress overshoot occurs. Finally, for $\dot{\gamma} > \tau_R^{-1}$ both η^+ and Ψ_1^+ pass through maxima during their approach to steady state, and the strain at overshoot increases with increasing strain rate. At the strain rates where the peak in Ψ_1^+ first begins to appear, it occurs at a strain in the range 5.0 to 5.5. The data of Wagner *et al.* for a melt of high molecular weight linear polymer with broad molecular mass distribution agrees with a peak in η^+ at $\gamma \approx 2$ but exhibits a delayed peak in Ψ_1^+ at $\gamma \approx 20$.

2.2 Theory

The dynamics of polymeric liquids is most often described in terms of the Rouse [62] and reptation [32, 33, 34, 69, 70, 71, 72] models. The Rouse model predicts a zero-shear viscosity $\eta_0 \propto N$, $D \propto N^{-1}$, and longest relaxation time $\tau_R \propto N^2$. There is ample experimental evidence, some of which has been mentioned elsewhere in this review, that, up to a critical chain length N_C, the long-time behavior of these properties of polymeric systems is in agreement with the Rouse model. For $N > N_C$, the behavior changes to $\eta_0 \propto N^{3.4}$ and $D \propto N^{-2}$ [73]. This change in behavior is usually explained in terms of reptation, the snake-like motion of a chain along its own contour due to the topological constraints caused by chain entanglements. The

reptation-based tube model of Doi and Edwards (DE) predicts $\eta_0 \propto N^3$ and $D \propto N^{-2}$. The Rouse model predicts a linear response in shear stress that is independent of the magnitude of the strain rate, both under transient and steady-state conditions. In contrast, the DE theory predicts shear thinning behavior at high shear rate with $\eta \propto \dot{\gamma}^{-1.5}$, $\Psi_1 \propto \dot{\gamma}^{-2}$, and $\Psi_2 \propto \dot{\gamma}^{-2.5}$ in the limit $\dot{\gamma} \to \infty$. For $\dot{\gamma} < \tau_d^{-1}$, η^+ monotonically approaches the steady-state viscosity upon onset of shear. For $\dot{\gamma} > \tau_d^{-1}$, a maximum is observed in η^+ occurring at a total strain $\gamma \approx 2$. The steady-state viscosity is reached at a strain $\gamma = \dot{\gamma}\tau_d$. The peak viscosity relative to steady-state increases with $\dot{\gamma}$. Overshoot is also observed for Ψ_2^+ but not Ψ_1^+, in contradiction with experiment.

DE theory assumes instantaneous and complete chain retraction, meaning that the length of the tube that a chain occupies remains constant in any flow. Marrucci and Grizzuti modified DE to allow chain retraction to be gradual and incomplete and, therefore, the tube to be stretched affinely by flow [74]. Thus, at sufficiently high shear rates ($\dot{\gamma} > \tau_R^{-1}$), the drag exceeds the elastic restoring force and the chain length passes through a maximum. The effect of chain stretching is to bring the model (DEMG) into better agreement with experiment by enhancing the overshoot in η^+, creating an overshoot in Ψ_1^+, and causing the strain at which the peak occurs to vary with strain rate [35, 75]. Recently, Remmelgas and coworkers [42] have developed a simple and tractable constitutive equation intended to mimic the DEMG model. The constitutive equation exhibits less shear thinning ($\eta \propto \dot{\gamma}^{-2/3}$) than DE (i.e. better agreement with experiment) as well as chain stretch at large shear rate (in contrast to DEMG).

As Mead *et al.* pointed out [43], a number of features of the nonlinear rheology of linear polymers are not described by the DE and DEMG theories. For a wide range of $\dot{\gamma} > \tau_d^{-1}$, shear stress is nearly constant for highly entangled melts or a

weak function of $\dot{\gamma}$ for less highly entangled systems. In contrast, DE and DEMG predict a maximum in shear stress followed by a decrease asymptotically proportional to $\dot{\gamma}^{-1/2}$. Also, at high shear rates in the shear-thinning regime, the η versus $\dot{\gamma}$ curves nearly merge into one with only week dependence on molecular weight (M). DE and DEMG predict that melt viscosity at high shear rate in the shear-thinning regime decreases with increasing M. In addition, stress relaxation after cessation of shear in the nonlinear regime depends on the prior strain rate while DE and DEMG predict that it should be insensitive to prior strain rate. Mead and Leal have modified DEMG to include a nonlinear finitely extensible force law [76, 77].

Recently, Marrucci suggested that chain stretching might not be needed to improve DE theory. Instead, he modified the tube model to include a relaxation mechanism termed "convective constraint release" (CCR) [37, 38]. Consider a monodisperse polymer melt in steady shear flow at a strain rate $\dot{\gamma} >> \tau_d^{-1}$ where τ_d is the longest relaxation time of the system. Typically, one would assume that perturbations in chain conformation would relax in a time of order τ_d. However, due to the high shear rate in this case, the tube surrounding the chain has been completely renewed by convection in a much shorter time of order $1/\dot{\gamma}$. That is, since on average the separation between chain centers of mass is of order R (the mean end-to-end distance), the relative velocity of two centers of mass is of order $R\dot{\gamma}$, and the "time spent together" is of order $R/(R\dot{\gamma}) = \dot{\gamma}^{-1}$. Tube renewal by diffusion and convection are considered to occur in parallel resulting in the equation for steady shear flow

$$\frac{1}{\tau} = \frac{1}{\tau_d} + \beta\dot{\gamma}\sigma \tag{2.8}$$

where τ is the relaxation time under flow conditions, β is an unknown numerical coefficient, and σ is the nondimensional shear stress. The resulting steady shear

stress versus $\dot{\gamma}$ curve possesses two qualitatively different behaviors depending on the value of β: either a CCR curve with increasing followed by decreasing stress that no longer approaches zero at high $\dot{\gamma}$ or a CCR curve that is a monotonically increasing function of shear rate. Unlike DE theory, the tube model with CCR is in approximate agreement with the empirical Cox-Merz rule

$$\eta(\dot{\gamma}) = |\eta^*(\omega)| \tag{2.9}$$

where η^* is the complex viscosity.

In addition to incomplete fulfillment of the Cox-Merz rule, the CCR modification of the DE theory does not address the deficiency of the limiting value ($\dot{\gamma} \to 0$) of the normal stress ratio $\Psi = -\Psi_2/\Psi_1 = 1/7$ (for DE theory with independent alignment approximation $\Psi = -\Psi_2/\Psi_1 = 2/7$) which recent accurate experimental data place at a larger value. Marrucci and Ianniruberto recently showed that the value of Ψ can only be raised by assuming that the tube cross-section becomes elliptical due to affine deformation [39]. This assumption also improves the fulfillment of the Cox-Merz rule. However, affine deformation of tube segments overpredicts the desired corrections. This suggests that, although the tube cross-section must become elliptical due to deformation, the change must not be affine (an assumption too complex to implement in the theory).

Mhetar and Archer have criticized the CCR results of Marrucci and Ianniruberto [40]. They believe that an oriented chain trapped in a cylinder is a more realistic picture at high shear rates than the Gaussian coil assumption. In the former case, the CCR renewal time is approximately $l/(r\dot{\gamma})$ where l and r are the length and radius of the cylinder. Mhetar and Archer suggest that under these conditions the renewal time might remain unchanged or increase with increasing $\dot{\gamma}$ since the ratio l/r is itself

a function of $\dot{\gamma}$. They have promoted a partial strand extension concept maintaining that chains subject to nonlinear step strain will only retract partially leading to significant chain stretch that should persist up until the time that the primitive chain escapes the deformed tube. They also show that primitive chain retraction reduces the number of entanglements between a deformed polymer chain and its neighbors thereby significantly enhancing molecular relaxation at high deformations. For this new model under steady shear, $\eta \propto \dot{\gamma}^{-1}$, $\Psi_1 \propto \dot{\gamma}^{-4/3}$, $\Psi_2 \propto \dot{\gamma}^{-7/3}$, and $-\Psi_2/\Psi_1(\dot{\gamma} \to 0) = 2/7$. The maximum in η^+ initially occurs at $\gamma = 2$ before increasing with strain rate. A weak overshoot also occurs in Ψ_1^+. Chain stretch due to incomplete retraction provides an additional source of stress that eliminates the stress downturn predicted by DE. Also, steady-state high-shear-rate stresses are in perfect agreement with the Cox-Merz rule. The model also predicts that the "stretch relaxation time" $\tau_s \propto \dot{\gamma}^{-0.5}$ at high $\dot{\gamma}$.

Recently, Mead, Larson, and Doi have reported a new simplified model for the CCR mechanism which, unlike the CCR mechanism of Marrucci, does account for the dependence of orientation and stretch on the tube coordinate of the chain [43]. This more complete model retains the successful features of DEMG while capturing many of the prominent nonlinear rheological properties in the $\dot{\gamma} > \tau_d^{-1}$ regime (such as a region of nearly constant shear stress) where the DE and DEMG theories fail. In fact, the shear-stress curves of Mead *et al.* are identical to those of Marrucci's CCR model for $\beta = 1$ in Marrucci's theory in the limit of very large τ_d/τ_R with $\dot{\gamma} \lesssim \tau_R^{-1}$.

Ait-Kadi and coworkers have made predictions for constant shear start-up using their recently developed rheological model for polymer melts and solutions [41]. They made the following observations: 1) the time to reach maximum overshoot is longer for Ψ_1^+ and Ψ_2^+ than for η^+, 2) the increase of Ψ_1^+ and Ψ_2^+ is slightly delayed compared to η^+, and 3) the height of the overshoot relative to steady state follows the trend

$\eta^+ > \Psi_2^+ > \Psi_1^+$ at the same shear rate.

Finally, Öttinger and Beris have recently proposed a thermodynamically consistent reptation model that avoids the independent alignment assumption made by Doi and Edwards and have made realistic predictions for the stress after double-step shear strain with flow reversal [44]. The fact that these last five articles which have been here reviewed were published in the first part of 1999 or the end of 1998 is striking evidence of the high level of interest that currently exists in the modeling of the nonlinear rheology of polymers.

2.3 Molecular dynamics simulations

Off-lattice models for chain-molecule melts can be generally categorized according to the amount of detailed molecular structure that the model retains. A natural division can be made between those that possess a high degree of atomistic detail (both explicit-atom and united-atom models) and those that do not (bead-spring models). Explicit-atom (EA) potential models explicitly account for each and every atom (including hydrogens) that make up the chain molecules. In a bead-spring model, each bead is taken to represent some number of units of the real polymer (typically 20 monomers or more). The springs are most often finitely extensible nonlinear elastic (FENE) springs with potential and force laws

$$u_{FENE}(Q) = -\frac{1}{2}HQ_0^2 \ln\left[1-(Q/Q_0)^2\right] \quad Q < Q_0 \tag{2.10}$$

$$= \infty \quad Q > Q_0 \tag{2.11}$$

and

$$\vec{F}_{FENE}(\vec{Q}) = \frac{-H\vec{Q}}{1-(Q/Q_0)^2} \quad Q < Q_0 \tag{2.12}$$

where $\vec{Q}$ is the vector between the centers of the adjacent beads, $Q = |\vec{Q}|$, Q_0 is the maximum allowable elongation of the spring, and H is the spring constant. FENE springs are favored since, like true macromolecules but unlike Hookean springs, they cannot extend indefinitely in a flow field. Such bead-spring models usually do not incorporate a potential governing the bending of the bond angles. Excluded volume is usually modeled by a shifted, truncated Lennard-Jones (LJ) 12-6 potential. The cut-off at $2^{1/6}\sigma$ ensures that this potential, often referred to as the WCA potential, is purely repulsive. The potential and force laws are given by

$$u_{WCA}(r) = 4\epsilon\left[\left(\frac{\sigma}{r}\right)^{12} - \left(\frac{\sigma}{r}\right)^{6} + \frac{1}{4}\right] \quad r \leq 2^{1/6}\sigma \tag{2.13}$$

$$= 0 \quad r > 2^{1/6}\sigma \tag{2.14}$$

and

$$\vec{F}_{WCA}(r) = \frac{24\epsilon}{\sigma}\left[2\left(\frac{\sigma}{r}\right)^{14} - \left(\frac{\sigma}{r}\right)^{8}\right]\frac{\vec{r}}{\sigma} \quad r \leq 2^{1/6}\sigma \tag{2.15}$$

where r is the distance between sites, ϵ is the characteristic energy parameter and σ is the bead diameter. In a united-atom (UA) potential model, some small number of atoms are collapsed into a single interaction site. For example, in a UA model for alkanes, each carbon and its attached hydrogens are treated as a single site. Though such a model is no longer atomistically detailed with respect the hydrogens, it is still atomistically detailed with respect to the carbon atoms. In contrast, a bead-spring model is not atomistically detailed with respect to either. UA models typically employ

a torsional potential of the form

$$V_t(\phi) = \sum_i a_i[\cos(\phi)]^i \tag{2.16}$$

governing the distribution of the dihedral angle ϕ where a_i is the constant in term i. Potentials for bond-angle bending

$$V_b(\theta) = \frac{-k_b}{2}(\theta - \theta_b)^2 \tag{2.17}$$

(where θ and θ_b are the bond angle and its equilibrium value and k_b is the bond-angle-bending force constant) and bond stretching

$$V_s(r) = \frac{-k_s}{2}(r - r_{eq})^2 \tag{2.18}$$

(where r and r_{eq} are the bond length and its equilibrium value and k_s is the bond-stretching force constant) are sometimes utilized in UA models, but often fixed bond lengths and bond angles are used. Sites on different molecules and sites on the same molecules separated by more than three bonds interact via a LJ 12-6 potential

$$u_{ij}(r) = 4\epsilon_{ij}\left[\left(\frac{\sigma_{ij}}{r}\right)^{12} - \left(\frac{\sigma_{ij}}{r}\right)^{6}\right] \tag{2.19}$$

where r is the distance between sites i and j, ϵ_{ij} is the well depth and σ_{ij} is the zero point of the potential between a site of type i and a site of type j. A large number of UA and EA parameterizations for alkanes have been proposed in the literature [26, 31, 46, 47, 78, 79, 80, 81, 82, 83, 84, 85, 86, 87, 88, 89]. The anisotropic united atom (AUA) model of Toxvaerd [82] attempts to improve on the UA description by taking into account the anisotropy of the interactions between methylene groups with the introduction of a displacement between the centers of force of the nonbonded interactions and the centers of mass of the united atoms.

In an equilibrium molecular dynamics (EMD) simulation, the zero-shear viscosity of a liquid can be calculated by integrating the autocorrelation time of the stress tensor over time

$$\eta = \frac{V}{k_B T} \lim_{\tau \to \infty} \int_0^\tau \mathrm{d}t \langle P_{xy}(t) P_{xy}(0) \rangle \tag{2.20}$$

where V is the volume of the simulation box, k_B is Boltzmann's constant, T is the temperature, t is time, and $\langle P_{xy}(t) P_{xy}(0) \rangle$ is the correlation function of the xy-component of the stress tensor. In a nonequilibrium molecular dynamics (NEMD) calculation, the shear-rate dependent viscosity η is determined from the constitutive relation

$$\eta = -\frac{\langle P_{xy} \rangle}{\dot{\gamma}} \tag{2.21}$$

where $\dot{\gamma}$ is the strain rate characterizing the shear field. If the x-direction is the flow direction and the y-direction is the velocity gradient direction, then $\dot{\gamma} = \partial u_x / \partial y$ where u_x is the streaming velocity in the x-direction. The first and second normal stress coefficients are defined as

$$\Psi_1 = -\frac{\langle P_{xx} \rangle - \langle P_{yy} \rangle}{\dot{\gamma}^2} \tag{2.22}$$

and

$$\Psi_2 = -\frac{\langle P_{yy} \rangle - \langle P_{zz} \rangle}{\dot{\gamma}^2}. \tag{2.23}$$

The stress growth coefficients (η^+, Ψ_1^+, and Ψ_2^+) are the time-dependent versions of these viscometric functions (η, Ψ_1, and Ψ_2) upon start-up of shear flow.

2.3.1 Simulations with bead-spring models

Kremer and Grest performed EMD simulations of bead-spring melts weakly coupled to a heat bath [90, 91, 92]. This work was an attempt to span the crossover regime from Rouse to reptation dynamics in these chain molecule systems. Chain lengths ranged from $N = 5$ to $N = 400$. In their simulation algorithm, each monomer in the system moved according to the equation of motion

$$\ddot{\mathbf{r}}_i = \nabla \sum_{j \neq i} U_{ij} - \Gamma \mathbf{r}_i + \mathbf{W}_i(t). \tag{2.24}$$

The interaction potential U_{ij} consisted of a purely repulsive LJ part and a FENE attraction. Γ was a small friction constant weakly coupling the monomers to a heat bath. $\mathbf{W}_i(t)$ was a Gaussian white-noise source. A particular density ($\rho^* = 0.85$) was chosen such that the tube diameter in the reptation picture would be small but relaxation times would be small enough to allow equilibration over a few million timesteps. Analysis of the diffusive motion in the simulated chain systems revealed an entanglement length N_e of approximately 35 beads. They found that the Rouse model provided an excellent description for chains shorter than N_e; the dynamics of longer chains was described by the reptation model. By further coarse-graining the chains to primitive chains, they were able to visualize the confinement, within the tube, of chain motion.

Xu *et al.* performed NEMD simulations, both at constant pressure and at constant volume, of monodisperse melts of linear (N=10, 20, or 50) and branched (backbone length of 23 beads with 3 equally spaced sidechains of length 1, 2, or 3) chains under shear [93]. Zero-shear viscosities of the linear chains scaled with N as predicted by the Rouse model. The viscosity behavior was similar in constant volume and constant pressure simulations with slightly different power law exponents (-0.42 for the former

and -0.4 for the latter). For the case of branched chains, Xu *et al.* observed that 2-bead branches yielded a Newtonian viscosity twice that of chains with 1-bead branches. A Newtonian viscosity was not observed for the chains with 3-bead branches at the shear rates covered by the study. However, at high strain rate, the curves for all three types of branched molecules collapse into a single line with power law exponent -0.36, suggesting the backbone length is the dominant factor determining the viscosity under those conditions. In a later publication [94], Xu *et al.* presented zero-shear viscosities determined by the Green-Kubo method in good agreement with those determined by NEMD.

Kröger and coworkers performed NEMD simulations of bead-spring model polymer melts under planar Couette flow [95]. A shifted, repulsive LJ potential was used to model excluded volume and FENE springs joined the beads to one another. Kröger *et al.* performed simulations for chains of 10, 30, 60, and 100 beads covering five decades in shear rate and placed emphasis on the underlying microstructural changes occurring in the liquids under shear. Non-negligible alignment of chain ends was observed, and inclusion of this effect in theoretical models led to better agreement with experimental data for polymer melts. Proportionality between stress and the alignment tensor was confirmed up to shear rates in the shear-thinning region, but higher strain rates revealed violations of the stress-optical law. Characteristic elliptical distortions of chain scattering patterns, seen in neutron scattering experiments, were observed in the simulations. Zero-shear viscosities scaled linearly with chain length for $N \leq 60$. Evidence was seen for an upturn at $N = 100$, but those simulations did not probe the Newtonian regime.

Kröger and coworkers performed NEMD simulations of bead-spring model polymer melts during onset of and relaxation from elongational flows in order to make comparison with experimental measurements. This study focused on cases of pronounced

deviation from the linear stress-optical law in an attempt to gain molecular-level insight into nonlinear viscoelasticity. Simulations were performed in the constant-NVT ensemble on a system of 8,400 total beads in chains of 30 beads each. Kröger *et al.* employed FENE springs and the shifted, repulsive LJ potential. The tensile stress upon onset of elongation and relaxation after elongation were observed as a function of elongation rate. The intramolecular contributions from nearest neighbors, intramolecular contributions from non-nearest neighbors, and intermolecular contributions were separated out for analysis. Kröger and coworkers confirmed the stress-optical rule for small elongation rates or high temperatures but observed violations for higher elongation rates and temperatures close to the glass transition. They determined that affine motion and the reorientational diffusion of segments determined the occurrence or non-occurrence of stress overshoot.

Kröger also performed studies of polymer melts under shear by NEMD for chains of length ranging from $N = 10$ to $N = 400$ [96]. Again, the FENE and shifted, repulsive LJ potentials were used. He observed power law behavior at high shear rates and made extrapolation to zero-shear viscosity. For N up to 100, as predicted by the Rouse model, the zero-shear viscosity increased linearly with N. For longer chains, the viscosity increased more strongly with N, though the error bars on the extrapolated values were quite large. Kröger and Voigt identified a mathematically rigorous geometrical criterion to model entanglements [97]. They defined the entanglement relation between two chains A and B as follows: for each chain A one defines a convex volume by connecting each point on curve A to each other point on A with a straight line segment. To be entangled, chain A must intersect the convex volume of chain B, and chain B must intersect the convex volume of chain A. Defined in this way, the entanglement is also associated with a certain section of the chain so that self-entanglements and multiple entanglements can be counted. Voigt performed

NEMD simulations of a monodisperse polymer melt with $N = 240$ at a dimensionless strain rate of $\dot{\gamma}^* = \dot{\gamma}(m\sigma^2/\epsilon)^{1/2} = 0.01$ under constant shear-rate start-up tests. Voigt monitored the mean squared bond force for monomers in the entangled region of the chain ($\langle F_B^2 \rangle_E$) in comparison to the mean value for the entire system ($\langle F_B^2 \rangle$). The sign of $\langle F_B^2 \rangle_E - \langle F_B^2 \rangle$ was always positive, and the loading of the entanglement network during stress-overshoot was related to a sharp rise in this quantity at short times. The difference between the mean squared values of the intermolecular forces ($\langle F_I^2 \rangle_E - \langle F_I^2 \rangle$) also had a positive sign.

2.3.2 Simulations with atomistically-detailed models

Though our dominant interest in this study of alkanes is in their rheological behavior under shear, a review of the literature related to the modeling of alkane chains by molecular dynamics simulation would be incomplete without at least some treatment of equilibrium (from which the zero-shear viscosity may be calculated) as well as nonequilibrium molecular dynamics simulations. Therefore, we will briefly highlight a number of EMD studies of alkanes before turning to our primary interest: NEMD of alkanes.

Yoon, Smith, Paul, and coworkers have completed numerous EMD simulations of UA and EA models of polyethylene over the past decade [46, 47, 98, 99, 100, 101, 102, 103, 104]. In one of their early efforts [98], they performed stochastic dynamics and molecular dynamics simulations of n-tridecane at 300 and 450 K using both UA (simulation of 750 ps duration) and EA (simulation of 200 ps duration) models. Nearly identical results for chain conformations were seen from both models. However, the EA model exhibited enhanced interchain packing and orientational correlations and, in contrast to the UA model, reproduced very closely the height and width of the

interchain peak in the experimental x-ray scattering profile. Yoon *et al.* also observed that the inclusion of explicit hydrogens decreased the self-diffusion coefficient by a factor of 6 to 8 compared to the UA model and brought it into reasonable agreement with experiment. Not calibrated for *n*-tridecane, these potentials yielded poor *P-V-T* behavior, prompting Smith and Yoon to perform additional 200 ps simulations with different EA and UA parameterizations at 312 and 450 K [47]. This new EA model produced results in good agreement with experimental pressures, x-ray diffraction patterns, self-diffusion constants, and C-H vector orientational correlation times. The UA model yielded a more extended chain structure than the previous UA model and enhanced local chain dynamics compared to the EA model. EMD simulations of 45 *n*-$C_{44}H_{90}$ molecules of approximately 100 ps in duration utilizing the EA model reproduced well the experimental *P-V-T* behavior and x-ray scattering profiles. Preliminary analysis of conformational transitions suggested strong correlations between neighboring bonds, especially the second and fourth neighbors. The poor performance of the UA model prompted Paul, Smith, and Yoon to optimize the potential parameters to reproduce the experimental pressure and heat of vaporization for *n*-tridecane at 312 K [46]. Simulations of *n*-$C_{44}H_{90}$ with the calibrated model yielded a dramatic change in the pressure suggesting that the non-bonded parameters optimized for *n*-$C_{13}H_{28}$ were unable to adequately reproduce experimental *P-V-T* behavior for other chain lengths. In order to overcome this, they adopted the SKS [26] energy parameters (ϵ) but kept their own size parameter (σ). Simulations of *n*-$C_{44}H_{90}$ (400 and 450 K, 45 chains) with this model yielded *P-V-T* behavior, chain conformations, and x-ray scattering profiles in good agreement with experiment. Self-diffusion was observed to be 30% faster than the experimental value. Smith *et al.* further examined the long-time molecular motions in the *n*-$C_{44}H_{90}$ system [100] and observed long-time tails for the local bond vector orientation autocorrelation functions that approached those of the

end-to-end vector autocorrelaton function, evidence of correlation between local bond vectors and relaxation of the chain backbone. Han, Jaffe, and Yoon pointed out that, based on MD and BD simulations of n-$C_{13}H_{28}$ (100 chains), n-$C_{44}H_{90}$ (45 chains), and n-$C_{100}H_{202}$ (64 phantom chains, i.e. chains that intersect or cross themselves freely), the polymethylene chains exhibited identical conformation characteristics in melts, phantom chains, and θ solvents [101]. They attributed this behavior to the lack of correlation between local chain conformations and intermolecular attractions.

Smith and coworkers continued their series of simulation studies by examining the short time dynamics (< 20 ps) of a system of 40 n-$C_{100}H_{202}$ chains (12,080 atoms for the EA case and 4,000 atoms for the UA case) at 509 K [102]. They made detailed comparison to incoherent dynamic structure factors determined from time-of-flight neutron scattering experiments and found that the decay of $S_{inc}(q,t)$ that occurred between 0.1 and 10 ps was the result of a combination of torsional librations and jumps. Paul *et al.* then performed longer EA (40 chains, 1.1 ns, 509 K) and UA (40 chains, 2 ns, 450 and 509 K) simulations of n-$C_{100}H_{202}$ [103]. This represented the first effort to simulate a fully equilibrated sample of chains long enough to follow Gaussian chain statistics (and therefore Rouse chain dynamics) using well-validated and realistic potential models. They observed very good agreement with experimental self-diffusion coefficients. The Rouse model consistently described chain rotational and translational diffusion, but Paul *et al.* observed systematic deviations in the static and dynamic behavior of the chains' internal modes. After accounting for the effect on the dynamic structure of a 20% difference between simulation and experimental self-diffusion coefficients by plotting the structure factor versus scaled time Dt where D is the self-diffusion coefficient, Paul and coworkers observed perfect quantitative agreement between simulation and neutron spin echo spectroscopy of the intermediate dynamic structure factor over the whole range of momentum transfer studied [30].

Based on these findings, they tested the experimental results for the deviations from Rouse behavior which they had previously observed in simulations. They concluded that the Rouse model is only capable of describing behavior on time scales on the order of the Rouse time or larger and on length scales of the chain radius of gyration or larger. Harnau *et al.* disagreed with this interpretation [105]. They suggested that C_{100} chains are too short (and therefore stiff) to exhibit the self-similar behavior on a broad length scale required by the Rouse model. They demonstrated that an extension of the Rouse model to account for molecular stiffness was able to reproduce the data of Paul *et al.* very well. Finally, Londono and coworkers compared neutron diffraction isotopic substitution experiments on three samples of polyethylene at 428 K to the C_{44} and C_{100} simulation data generated previously. They demonstrated that the differences in the HH intermolecular radial distribution functions observed for polyethylene, C_{44}, and C_{100} were not simply due to temperature differences.

Harmandaris *et al.* [31] have performed EMD simulations of polydisperse polyethylene melts of average molecular length C_{24}, C_{78}, and C_{156} and polydispersity indices of 1.09 using a UA potential model at $P = 1$ atm and $T = 450$ K. The self-diffusion coefficient D calculated for various chain lengths was in good agreement with experiment. The monomeric friction coefficient, extracted from D using the Rouse model, increased with increasing chain length before reaching a plateau in the range $60 < N < 80$. Zero-shear viscosities calculated from the monomeric friction coefficient and the Rouse model were in good agreement with experiment, and friction coefficients extracted from the decay of the end-to-end vector autocorrelation function were in good agreement with those extracted from diffusion for $N > 40$. Brown and coworkers [106] also performed simulations of C_{100} using a UA model but did not observe full configurational relaxation within the simulation run of 2 ns. van Zon and de Leeuw [107] have recently performed EMD simulations of C_{100} poly(butadiene) (20

chains) using a realistic united atom potential model in order to study glass transition.

Boyd and coworkers have performed a number of EMD simulations of polyethylene as well as polybutadiene consisting of a single long chain (e.g. $N = 768$) coiled up in the cubic simulation box [108, 109, 110, 111, 112]. They have recently adopted the anisotropic UA representation of Toxvaerd [82], adjusting the nonbonded potential parameters to agree with experimental P-V-T behavior. They have been particularly interested in studying the onset of vitrification [108, 109, 110, 112] and small penetrant diffusion [113, 114, 115, 116] and have performed a 90 ns simulation of polyethylene (1 molecule, $N = 768$) on a workstation cluster [111].

Parallel to the work of Paul, Smith, and Yoon, Mondello, Grest, and coworkers have performed extensive EMD simulations of linear and branched alkanes. Rather than an interest in polyethylene, their primary motivation was an interest in chains typical of lubricant basestocks. Using an extension of the SKS UA potential model as well as Toxvaerd's AUA model, they performed EMD simulations of n-decane, n-hexadecane, and squalane at a variety of temperatures in order to study translational and rotational diffusion in addition to intramolecular dynamics [78]. Comparisons of conformational properties suggested that the UA model is less sensitive than the AUA model to changes in the torsional potential. Diffusion data were compared to experimental results. Predictions from the AUA model tended to be in fairly good agreement with experiment while the UA model significantly overestimated the diffusion coefficients. Despite this, the UA appeared to predict well the temperature dependence of the diffusion coefficients. Mondello and coworkers also performed EMD simulations of the branched alkanes 10-n-hexylnonadecane and 5,14-di-n-butyloctadecane at variety of temperatures again comparing the UA and AUA models [117]. Once again, the UA model overestimated experimental diffusion data. Mondello *et al.* observed that the temperature dependence of diffusion is affected by the number and

length of an alkane's branches. An increase in the number of branches and/or their length increased the temperature dependence which Mondello *et al.* attributed to the reduced dynamical flexibility of the molecule. Mondello and Grest also calculated zero-shear viscosities for *n*-decane and *n*-hexadecane by the Green-Kubo formalism and made comparison to experiment. Unexpectedly, viscosity values calculated for the UA and AUA were much closer to each other than the corresponding diffusion coefficient values, for which the AUA model was superior. Both models underestimated the viscosity at temperatures close to the melting point. They also discussed the relative merits of EMD versus NEMD for viscosity calculations and drew similar conclusion to Cui *et al.* who also performed Green-Kubo calculations for *n*-decane and *n*-hexadecane [118, 119]. Kostov *et al.* compared the MD data of Mondello *et al.* to time correlation functions predicted by a theory developed for calculating the memory functions of flexible polymers [120]. The theory agreed with simulation for all correlation functions and all times if a scale factor was used to modify the friction factor predicted from simulation and the Rouse model. This was true for both linear and branched alkanes. For C_{44}, scaling was no longer necessary.

Mondello *et al.* performed extensive EMD and NEMD studies of linear alkanes in the range C_6 to C_{66} [19] in order to investigate the crossover from short-chain to Rouse behavior. They employed the UA models of Siepmann *et al.* [26] and Paul *et al.* [46] and the AUA model of Toxvaerd [82]. Mondello *et al.* performed a series of simulations ($6 \leq N \leq 66$, where N is the number of carbons per chain) at constant density ($T = 448$ K, $\rho = 0.766$ g/mL independent of chain length) using SKS alone, simulations at experimental density for $P \approx 0.1$ MPa and $T = 400$ K for *n*-C_{16}, *n*-C_{24}, *n*-C_{30}, and *n*-C_{44} using all three models, as well as rotational isomeric state (RIS) simulations for $34 \leq N \leq 2000$. They examined how the ratio $\langle R^2 \rangle / 6 \langle R_g^2 \rangle$ (equal to 1 for a Gaussian chain, where R^2 is the squared end-to-end distance and R_g^2 is the

squared radius of gyration) was affected by chain length. Due to the rigidity of short chains, the ratio increased with increasing N up to $N = 16$. For $N \geq 16$, increased chain flexibility caused the ratio to decrease with increasing N. The deviation from Gaussian statistics was less than 2% for $N \geq 600$. At constant density, self-diffusion coefficients (D, determined from the limiting slope of the center-of-mass mean-squared displacement) and rotational relaxation times (τ_1, determined from the orientational relaxation of the longest principal axis of the molecule's ellipsoid of inertia) were calculated from EMD simulations, and the Newtonian viscosity was determined by NEMD at a strain rate expected to fall in the plateau region. Three equations from the Rouse model for estimation of the monomeric friction coefficient were used: in terms of the diffusion coefficient

$$\zeta_D = \frac{k_B T}{ND}, \tag{2.25}$$

in terms of the rotational relaxation time (τ_1) and end-to-end distance (R)

$$\zeta_\tau(R) = \frac{3\pi^2 k_B T \tau_1}{N\langle R^2 \rangle} \tag{2.26}$$

where k_B is Boltzmann's constant, and in terms of the rotational relaxation time and radius of gyration (R_g)

$$\zeta_\tau(R) = \frac{\pi^2 k_B T \tau_1}{2N\langle R_g^2 \rangle}. \tag{2.27}$$

ζ_D was found to vary nearly linearly with N, and ζ_τ was much larger than ζ_D for small N. Additionally, Mondello *et al.* compared three equations to estimate the Newtonian viscosity from the Rouse model in terms of D

$$\eta_D(R) = \frac{\rho RT\langle R^2 \rangle}{36MD} \tag{2.28}$$

and

$$\eta_D(R_g) = \frac{\rho RT\langle R_g^2 \rangle}{6MD} \tag{2.29}$$

and τ_1

$$\eta_\tau = \frac{\pi^2 RT\tau_1}{12M} \tag{2.30}$$

where M is the molecular weight and ρ is the density. According to the Rouse model, these estimates of ζ and η should be equivalent; Mondello and coworkers found this to be the case for $N \geq 66$. While the other estimates of η only agreed with the NEMD results for $N = 66$, $\eta_\tau \approx \eta_{NEMD}$ for all N. Since approximately 10 times less CPU time was required to determine τ_1 than η_{NEMD}, Mondello *et al.* suggested that determination of τ_1 is an efficient alternative to NEMD for the estimation of the Newtonian viscosity of unentangled linear chains. Self-diffusion at atmospheric pressure was examined with increasing N for all three models, and comparison was made to experiment. Both the UA model of Paul *et al.* and the AUA model agreed well with experiment while the SKS model consistently overestimated D by 15-50 %. Both the experiments and the models revealed a stronger dependence of D on N than predicted by the Rouse model.

Also, Mondello, Grest, and a number of other co-authors have performed EMD simulations of a variety of oligomeric analogs ($30 < N < 33$) of hydrocarbon polymers to determine thermodynamic and structural properties with applications to the miscibility of polymer blends [121, 122, 123, 124]. In order to correlate cohesive energy densities to chain architecture, they identified the two most relevant features of chain architecture: the number of consecutive backbone carbons without side groups and the side group size.

Mundy and coworkers used the Green-Kubo formalism to calculate the shear viscosity of *n*-decane at $T = 480$ K in excellent agreement with experiment [125]. They also used Green-Kubo to calculate the viscosities of *n*-decane and 4-propylheptane at 480 K and a variety of densities, accurately predicting the pressure derivative of

the viscosity. The only prior molecular-simulation-based calculation of the pressure derivative of viscosity was by Cummings and Varner, Jr. [126] who studied water. Padilla and Toxvaerd have performed a number of EMD studies of alkane diffusion including *n*-butane, *n*-pentane, and *n*-decane [127, 128, 129]. They concluded that diffusion of the molecule along its backbone is favored for decane but not pentane. Daivis and Evans have also performed EMD studies of *n*-butane near its boiling point. As Mondello and Grest also observed for *n*-decane and *n*-hexadecane, Daivis and Evans observed a slight system-size dependence of the self-diffusion coefficient for butane. Also, Dysthe *et al.* have recently performed EMD simulations of linear and branched alkanes [130, 131]. They demonstrated that the effects of integration time step, potential cut-off, and system size are small compared to the computational precision in most cases. They also demonstrated that MD can quantitatively predict the viscosity of a seven-component natural gas and showed that mixtures can be treated representatively even when only one or two of a species are present in the simulated system.

Rowley and Ely [132, 133, 134] studied isomeric effects in the *n*-butane/*iso*butane and *n*-hexane/cyclohexane/benzene systems using NEMD. This work was motivated by the failure of corresponding states theory to predict the viscosity of low molecular weight branched and cyclic hydrocarbons. For the butanes, they used the Ryckaert-Bellemans potential [86] with fixed bond lengths and angles. The only difference between the models used for *n*-butane and *iso*butane was the geometric arrangement. Though the opposite trend was seen in experiments, the simulated viscosity of *iso*butane was lower than that of *n*-butane, evidence that purely structural differences cannot explain the experimental trend. They speculated that in the simulations the branched molecule had a lower viscosity at low shear rates because it did not produce as much "drag" as the longer *n*-butanes, some of which had orientations perpen-

dicular to the shear. They identified molecular alignment as the primary cause of shear-thinning in the fluids and suggested that the lack of large orientational alignment for *n*-butane accounted for its smaller shear-thinning slope. By increasing the σ parameter of the *iso*butane model by 2.5%, Rowley and Ely were able to produce substantially better agreement with experiment.

Rowley and Ely continued this study by simulating *n*-hexane, cyclohexane, and benzene using six equivalent sites. Since the simulated viscosities of *n*-hexane and cyclohexane were in good agreement with experimental values, they concluded that the difference in viscosity between those two molecules was primarily structural. The benzene viscosities were significantly higher than experiment, suggesting important non-structural effects. Though the linear alkane tended to orient with the flow field, cyclohexane experienced little shear induced ordering since its chair geometry insured that it spanned multiple shear planes. At low strain rates, benzene tended to align in stacked layers that slid over one another, while at higher strain rates tumbling motions in the x-y plane occurred.

Lee and Cummings also addressed the subject of branching in butanes by NEMD simulations of planar Couette flow [135]. They employed two UA models and an EA model generated from the amalgamation of several models. The UA models used were the Ryckaert-Bellemans [86] and Chynoweth *et al.*'s modification of it [87, 136, 137]. They found that the UA models in general predict the viscosity of *n*-butane well. However, as did Rowley and Ely, Lee and Cummings calculated a lower viscosity for *iso*butane than *n*-butane, in contrast with experiment. The EA model did not yield quantitative agreement for either the branched or linear alkane. On the other hand, it did predict a higher viscosity for *iso*butane than for *n*-butane.

Clarke and Brown [138] attempted to show how torsional motions can affect the rheological properties of liquids of chain molecules by comparing the constant-NVT

shear-flow behavior at 200 K and 300 K of *n*-hexane and "flexane", identical to *n*-hexane except that its torsional potentials were set to zero. They used the UA potential of Ryckaert and Bellemans [86] with rigid bond lengths and bond angles. Equilibrium viscosities were estimated by extrapolation to $\dot{\gamma} = 0$. At 200 K, removal of torsional barriers reduced the equilibrium viscosity of hexane by a factor of 2. Increasing hexane's temperature to 300 K produced the same effect. They attributed these effects to the dynamic coupling of torsional flexibility with the molecular translational motions determining shear viscosity. At the highest strain rates, the viscosity tended to be the same regardless of temperature and flexibility which Clarke and Brown attributed to decoupling due to structural changes occurring under high rates of strain.

Edberg, Morriss, and Evans [139] performed NEMD simulations of *n*-butane (292 K) and *n*-decane (481 K) at constant volume. They used a model similar to that used by Clarke and Brown with rigid bond lengths and bond angles. They performed linear extrapolation in $\dot{\gamma}^{0.5}$ to $\dot{\gamma} = 0$ to determine Newtonian viscosities approximately 25% above the experimental value for butane and in good agreement with experiment for decane. The observed signs of the normal stress differences ($\Psi_1 > 0$ and $\Psi_2 < 0$) were in agreement with the experimental trends for polymers though the value of their ratio ($-\Psi_1/\Psi_2 \approx 1$) was larger than the experimental value ($-\Psi_1/\Psi_2 \approx 0.4$) [49, 50]. For both molecules, Edberg *et al.* observed shear thinning followed by second Newtonian viscosities at intermediate strain rates. Chynoweth *et al.* [140] studied *n*-butane using an increased system size and a simulation of longer duration as well as a wider range of shear rates. Rather than rigid bond lengths and angles, they employed bond-stretching and bond-angle-bending potentials. In contrast to the results of Edberg *et al.* , they observed a linear dependence of viscosity on $\dot{\gamma}^{0.5}$ that held over the entire range of strain rates studied. When plotted in the form $\log \eta$ vs. $\log \dot{\gamma}$, their

results revealed clear evidence of a first Newtonian region. Morriss and coworkers [16] compared the rheology of *n*-decane and *n*-eicosane. In comparison to their previous decane simulations [139], larger systems sizes were used to eliminate the harmonic stress response seen previously, and the WCA potential (rather than LJ) was used to model excluded volume. They studied the influence of shear on a variety of properties including viscosity, normal stress differences, shear dilatancy, internal energy, dihedral transition rates, constraint forces, and molecular orientation. They studied a wider range of strain rates and observed a region of shear-thickening behavior for both molecules at dimensionless shear rates $\dot{\gamma}^* > 1.0$ where $\dot{\gamma}^* = \dot{\gamma}(m\sigma^2/\epsilon)^{1/2}$. They speculated that this observation may have been due to the use of an NVT ensemble. The average alignment angle to the flow direction for both molecules decreased with increasing strain rate from the linear-regime value of 45°, decreasing more rapidly for eicosane than for decane.

Davis, Evans, and Morriss [141] extended their study to branched alkanes, comparing the rheology of 5-butylnonane and *n*-tridecane. They performed steady state simulations of planar Couette flow and again observed shear thickening behavior at $\dot{\gamma}^* > 1.0$ for both molecules. For $0.05 \leq \dot{\gamma}^* \leq 0.5$, they observed shear thinning with power law exponents of -0.38 for the branched alkane and -0.43 for the linear molecule. At the lowest shear rates simulated, which were still in the shear-thinning regime, the viscosity of the branched alkane was greater than that of the linear one, opposite the trend in experimental zero-shear viscosities for 5-butylnonane and *n*-tridecane. Daivis *et al.* speculated that this was a result of the more rapid decrease with increasing strain rate of the linear alkane's viscosity compared to the branched alkane as well as the likelihood that the linear alkane had a smaller critical strain rate for the transition from Newtonian to non-Newtonian behavior. Again, the signs of Ψ_1 and Ψ_2 were consistent with experiment. The ratio $-\Psi_1/\Psi_2$ increased with

increasing strain rate from 0.25 to 0.55 for the linear alkane and from 0.4 to 0.75 for the branched one. Interpreting the molecules' shapes in terms of equivalent ellipsoids of inertia, Daivis *et al.* observed that the linear molecule elongated and became a prolate ellipsoid as strain rate increased. In contrast, the branched molecule flattened and became a oblate ellipsoid.

Daivis and Evans [142] revisited the surprising occurrence of shear thickening at high strain rate seen in their previous simulations of linear and branched alkanes by performing NEMD simulations of *n*-decane in the NPT ensemble, once again with fixed bond lengths and bond angles. They found that the shear-thickening behavior observed in constant-volume simulations did not occur under constant pressure. In addition, they performed simulations at strain rates in the Newtonian regime and found good agreement between the Newtonian viscosity and that calculated from EMD simulations using the Green-Kubo formalism. This result was also confirmed by Mundy *et al.* who performed NEMD simulations of liquid *n*-decane in the NVT (EMD and NEMD) and NPT (NEMD) ensembles [125, 143] at $T = 480$ K. They used a multiple timestep algorithm [27] and also introduced a bond-stretching potential. Like Daivis and Evans, Mundy *et al.* observed different shear-thinning behavior between the NPT and NVT ensembles, but they did not observe shear thickening at any strain rate in either. They speculated that the shear-thickening behavior seen by Daivis and Evans may have been a result of their choice of thermostats.

Cui and coworkers [144] performed simulations of *n*-decane at the same state conditions studied by Mundy *et al.* The extrapolated zero-shear viscosity determined by Cui *et al.* was in good agreement with their EMD results using the Green-Kubo formalism and with experimental data. Like Mundy *et al.* , Cui *et al.* used a multiple timestep algorithm [27] and a bond-stretching potential. Cui *et al.* followed up this work with an NEMD study of three normal alkane systems: decane (298 K), hexade-

cane (300 K and 323 K), and tetracosane (333 K) [18]. Among the three systems, the slope of the log-log plot of viscosity versus strain rate varied from -0.33 to -0.41. Also, the viscosities of the three molecules overlapped at the highest strain rates. Cui *et al.* suggested that this high-strain-rate behavior was likely a consequence of these relatively short, stiff chains sliding past one another fairly easily when highly aligned. They calculated the alignment angle for the three systems as a function of strain rate. For all three systems, the alignment angle decreased sharply with increasing strain rate at low strain rates and asymptotically approached a limiting value at high strain rates. This limiting value decreased with increasing chain length. Cui and coworkers also calculated rotational relaxation times from EMD simulations of hexadecane at the two statepoints in terms of the orientational relaxation of the end-to-end vector. Using the values they calculated for hexadecane and those for decane and tetracosane determined by Mondello and Grest [78], Cui *et al.* observed that the inverse of this longest relaxation time was a good indicator of the transitional strain rate between Newtonian and non-Newtonian behavior.

Padilla and Toxvaerd performed simulations of *n*-decane [145] under planar Couette flow using the AUA model for alkanes [82] with fixed bond lengths but varying bond angles. Consistent with previous studies, they observed shear-thinning followed by shear-thickening behavior. Their results indicated that the viscosity depended mainly on the shape of the intermolecular potential and was relatively insensitive to the shape of the torsional potential. Also consistent with previous studies, they observed a consistent decrease of the mean square end-to-end distance with increasing strain rate for $\dot{\gamma}^* > 1.0$, and they offered the following explanation. The planar Couette flow field imposes a velocity profile on the fluid. In this field, a chain experiences tension when it is exposed to several layers moving at different velocities. Reduction of this tension can be achieved both by alignment with the flow field and by defor-

mation of the chain. The latter mechanism is dominant at high shear rates and the former at lower ones. The coupling of torsional motion and transport properties was further examined by Travis *et al.* using the method of frozen distribution sampling (FDS) [146]. This method involves comparing the dynamical properties of two fluids; one has dihedral angles which may vary continuously, and the other has fixed torsional angles with the same equilibrium distribution as the first liquid. Travis *et al.* used this method in conjunction with MD and NEMD studies of liquid *n*-butane and observed no significant coupling between torsional motion and shear viscosity or torsional motion and self-diffusion.

Lahtela *et al.* [147] performed NEMD simulations of 3-methylhexane in order to study the influence of potential models on simulated viscosity. They compared the results of three UA models as well as three different torsional potentials at three densities. The state points covered in the constant-NVT NEMD simulations ranged from $T = 350$ K and $\rho = 0.575$ g/mL to $T = 250$ K and $\rho = 0.645$ g/mL over a fairly narrow range of strain rates ($3.5\text{x}10^{10}$ s$^{-1} < \dot{\gamma} < 14.1\text{x}10^{10}$ s^{-1}). Lahtela *et al.* observed that relatively small changes in the intermolecular potential parameters of the branched methyl group produced large changes in viscosity. In contrast, viscosity was seen to be fairly insensitive to the details of the torsional potential and the intermolecular parameters of the main-chain methyl groups. They rationalized their observations by suggesting that side branches are unable to completely align with the flow field and drag as layers move past one another.

Allen and Rowley attempted to evaluate several intermolecular potential models for viscosity calculations on linear and branched alkanes (*n*-butane, *n*-octane, *n*-dodecane, 2-methylpropane, 2,2-dimethylbutane, 2,2-dimethylpropane, and cyclopentane) [148]. They performed NEMD simulations in the NVT ensemble and compared the Ryckaert-Bellemans UA [86], OPLS UA [79], and OPLS EA [149] potential mod-

els. Bond lengths and bond angles were kept rigid. Allen and Rowley estimated zero-shear viscosities using $\eta = \eta_0 - A\dot{\gamma}^{1/2}$ for extrapolation. At higher densities, they found that the UA models tended to underpredict viscosity in comparison to experiment. In general, the EA model tended to overestimate viscosity. Allen and Rowley hypothesized the following explanation for these observations. In the EA model, protruding hydrogen atoms interact with molecules in different velocity planes as they shear past one another. This causes additional drag, especially at higher densities. The fluid viscosity is further raised by the energy used to rotate hydrogens out of neighboring shear planes. In contrast, the UA descriptions are unable to model this mechanism of momentum transfer since they are isotropic about the carbon centers and do not explicitly model the hydrogens. The property-dependence of the OPLS UA model was assessed by performing simulations at the same state conditions that were used for its parameterization (done by comparison to experimental energies and densities). Property dependence of OPLS was a problem for branched alkanes but less so for linear and planar ones. They also performed simulations to assess the effect of the torsional potential on viscosity, including branched alkanes that were free to rotate and branched alkanes rigidly fixed in the lowest energy state. Discrepancies in the results for these two altered models suggested that the torsional potential can significantly affect the predicted viscosities for branched alkanes.

Khare *et al.* performed NEMD simulations of *n*-hexadecane, *n*-docosane, *n*-octacosane, 5,12-dipropylhexadecane (DPHD), and a mixture of 20 weight % *n*-$C_{36}H_{74}$ with 80 weight % *n*-hexadecane using the SKS UA potential [26]. Rather than using a harmonic bond-stretching potential, Khare *et al.* chose to use FENE springs to model bonds. Predicted viscosities tended to underestimate experimental values. Shear thinning was observed with power law exponents between -0.37 and -0.43 for the linear alkanes and -0.45 for DPHD. The viscosity of DPHD was higher than the nor-

mal alkane with same backbone length (n-hexadecane) as well as the normal alkane with the same molecular weight (n-docosane). Khare *et al.* estimated that branching resulted in a viscosity enhancement by a factor of approximately two. Power-law behavior was also seen in Ψ_1 with exponent ranging from -1.3 to -1.45 for the linear alkanes and -1.41 for DPHD. The ratio $-\Psi_1/\Psi_2$ was approximately a constant value in the range 0.4 to 0.5 but showed a slight tendency to increase at high strain rates. In terms of the effect of shear on chain configurations, the long normal alkanes (n-$C_{22}H_{46}$ and n-$C_{28}H_{58}$) exhibited a maximum in the mean square radius of gyration while the value for DPHD was essentially constant.

Chynoweth and coworkers [136] chose to focus on the rheology of n-hexadecane. They adopted the Ryckaert-Bellemans [86] potential model which they augmented with bond-stretching and bond-angle-bending potentials. They performed constant-NVT NEMD simulations at $T = 204$ K and $\rho = 0.896$ g/mL and observed power-law behavior with an exponent of -0.45 for the viscosity and -1.44 for the first normal stress coefficient. They found that the inverse of relaxation time τ predicted by results from the Rouse model agreed very well with the observed critical strain rate for onset of shear-thinning behavior. The extrapolated zero-shear viscosity (3.1 mPa s) was smaller than the experimental value (8.34 mPa s), prompting Chynoweth *et al.* to modify the intermolecular potential parameters [87]. The parameters were adjusted to yield accurate heats of vaporization and pressures for hexadecane as a function of ρ and T, and additional NEMD simulations were performed with the newly parameterized model. Slightly different power law exponents were observed: -0.53 for viscosity and -1.5 for first normal stress coefficient. The new zero-shear viscosity (5.6 mPa s) was an improvement but still underestimated the experimental value. In addition to these high T, high ρ simulations, Chynoweth *et al.* also performed runs at high T, low ρ ($T = 204$ K and $\rho = 0.842$ g/mL) and at low T, low ρ ($T = 100$ K and

$\rho = 0.871$ g/mL) in an attempt to study the strain-rate-dependent viscosity-pressure (α_P) and viscosity-temperature coefficients (α_T) [137]. They observed dramatic reductions in α_T and α_T at high shear rates which they suggested could prove to be of great importance in lubrication applications.

Mundy *et al.* [20] studied two isomers of C_{16}, 2,2,4,4,6,8,8-heptamethylnonane and *n*-hexadecane, using a UA model [80] including bond-stretching, bond-angle-bending, and torsional potentials. Simulations were performed at 380 K and $P = 1$ atm using a constant-NPT NEMD algorithm. Though no experimental viscosity data was available for heptamethylnonane, it was chosen because its bulk density is similar to *n*-hexadecane. Mundy *et al.* reported viscosity versus strain rate data including points in the Newtonian region. At high strain rates in the shear-thinning region, the viscosities of the two isomers tended to be equal. The Newtonian viscosity of 2,2,4,4,6,8,8-heptamethylnonane was larger than that of *n*-hexadecane. Mundy *et al.* also performed simulations of *n*-triacontane and squalane at 450 K and $P = 1$ atm. Though the Newtonian viscosities of the C_{30} isomers at 450 K were in qualitative agreement with that of *n*-hexadecane at 380 K, Mundy *et al.* were unable to observe a statistical difference between the data for triacontane and squalane.

Lahtela and coworkers [25] performed NEMD simulations of various isomers of $C_{20}H_{42}$ under shear using the OPLS [79] UA model with rigid bond lengths and bond angles. Simulations were performed over a fairly narrow range of strain rates ($5\text{x}10^{10}$ $s^{-1} < \dot{\gamma} < 14\text{x}10^{10}$ s^{-1}) at three temperatures (310, 290, and 270 K). Zero-shear viscosities were obtained by extrapolation of viscosity according to $\dot{\gamma}^{0.5}$. A comparison of the viscosities of *n*-eicosane, 2-methylnonadecane, 6-methylnonadecane, and 10-methylnonadecane was used to comment on the effect of sidechain position. Movement of the "branch" from the first to the second carbon significantly increased the viscosity. Further movement of the branch toward the center of the chain had only a

weak effect. A comparison of the viscosities of *n*-eicosane, 10-methylnonadecane, 8-*t*-butylhexadecane, and 8-cylcopentylpentadecane elucidated the effect of varying the type of sidechain. Increasing the size of the sidechain resulted in a large increase in the viscosity. The increase from 8-*t*-butylhexadecane to 8-cylcopentylpentadecane was much larger than that from 10-methylnonadecane to 8-*t*-butylhexadecane, evidently due to the different effects in the shear planes of the different sidechain geometries.

Travis and Evans [17] performed NEMD of *n*-eicosane in an attempt to characterize the effects of atomic and center-of-mass thermostats. In an NEMD simulation, a thermostatting mechanism is required to remove viscous heat to allow relaxation to a nonequilibrium steady state. An *unbiased* thermostat does not affect the average streaming velocity (translation, vibrational, or rotational) of the fluid. A thermostat that is *homogeneous* thermostats all of the fluid's degrees of freedom homogeneously. Both of these are desirable properties. Inhomogeneous thermostatting can lead to degrees of freedom that are much "hotter" than others. In this study, Travis and Evans compared the results of simulations with an unbiased, inhomogeneous center-of-mass thermostat (COMT) and a biased, inhomogeneous atomic thermostat (MSAT). The model employed for *n*-eicosane included fixed bond lengths and bond angles and the WCA intermolecular potential. They observed that the COMT yielded shear thickening for $\gamma^* = \dot{\gamma}(m\sigma^2/\epsilon)^{1/2} > 1$ while the MSAT yielded shear thinning over the entire range. Since a homogeneous, unbiased thermostat for molecular liquids was not available, they concluded that the interpretation of the very high shear rate rheology is obscured due to its sensitivity to the method of thermostatting.

Chapter 3

Molecular model and simulation method

To study the behavior of chain molecules under shear, we have employed a united atom model in conjunction with the nonequilbiurm molecular dynamics (NEMD) simulation method to model alkane melts of intermediate (isomers of C_{30}) to long (C_{100}) molecular size.

3.1 Potential model

The potential model for linear alkanes is essentially the same as the united atom model proposed by Siepmann *et al.* (SKS) [26], with the modification that the fixed bond length is replaced by a stiff harmonic bond-stretching potential. For branched alkanes, we use the extension of SKS as proposed by Mondello and Grest [78] in which the intermolecular potential parameters, ϵ and σ, proposed by Siepmann *et al.* for

the terminal methyl groups on linear alkanes are also used for methyl groups in chain branches.

In the model the CH_3, CH_2, and CH groups are treated as spherical interaction sites with interaction centers located at the centers of the carbon atoms. The interaction between sites on different molecules and between sites separated by more than three bonds on the same molecule is described by the well-known Lennard-Jones (LJ) potential with a cut-off distance of $2.5\sigma_{CH_2}$ (9.825 Å).

$$u_{ij}(r) = 4\epsilon_{ij}\left[\left(\frac{\sigma_{ij}}{r}\right)^{12} - \left(\frac{\sigma_{ij}}{r}\right)^{6}\right] \tag{3.1}$$

The LJ size and energy parameters are found in Table 3.1.

The Lorenz-Berthelot (LB) combining rules $[\epsilon_{ij} = (\epsilon_i\epsilon_j)^{1/2}, \sigma_{ij} = (\sigma_i + \sigma_j)/2]$ are used for the unlike interactions. Siepmann and coworkers fit the value of ϵ_{CH_2} to yield the correct increase in critical temperature for n-alkanes containing 8-16 carbons and then adjusted ϵ_{CH_3} to achieve the best absolute values of the critical temperatures of the same alkanes [80]. Mondello and Grest chose parameters for CH similar to those in OPLS [79]. The intramolecular interactions include a bond-stretching term, a bond-bending term, and a torsional term characterizing the preferred orientation and rotational barriers around all non-terminal bonds. The bond stretching is described

Table 3.1: Lennard-Jones potential parameters

Group	σ (Å)	ϵ/k_B (K)
CH_3	3.93	114
CH_2	3.93	47
CH	3.81	40

by a harmonic potential of the form

$$V_s(r) = \frac{-k_s}{2}(r - r_{eq})^2 \tag{3.2}$$

with an equilibrium bond length of $r_{eq} = 1.54$ Å and a force constant $k_s/k_B = 452\,900$ K/Å^2 [125] where k_B is Boltzmann's constant. The bond-angle bending is governed by a harmonic potential of the form

$$V_b(\theta) = \frac{-k_b}{2}(\theta - \theta_b)^2 \tag{3.3}$$

with the force constant $k_b/k_B = 62\,500$ K/rad^2 and equilibrium bond angle $\theta_b = 114°$ [150]. Two torsional potential parameterizations are used: one for $X - CH_2 - CH_2 - Y$ and one for $X - CH - CH_2 - Y$, where the nature of the X and Y groups are ignored. The torsional potentials are of the form

$$V_t(\phi) = \sum_i a_i[\cos(\phi)]^i \tag{3.4}$$

and were taken from OPLS. For branched alkanes, as suggested by Mondello and Grest, an *ad hoc* harmonic potential

$$V_i(\psi) = \frac{-k_i}{2}(\psi - \psi_i)^2 \tag{3.5}$$

is introduced to prevent the unphysical umbrella inversion of the sp_3 bond at the tertiary carbon branch points [78]. The intramolecular potentials are illustrated in Figure 3.1 and the parameters are summarized in Table 3.2.

In an NEMD calculation, the shear-rate dependent viscosity η is determined from the constitutive relation

$$\eta = -\frac{\langle P_{xy} \rangle}{\dot{\gamma}} \tag{3.6}$$

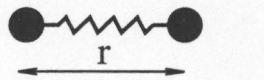

Bond stretching $V_s(r) = \frac{-k_s}{2}(r - r_{eq})^2$

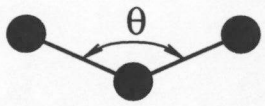

Bond bending $V_b(\theta) = \frac{k_b}{2}(\theta - \theta_b)^2$

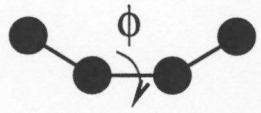

Torsion $V_t(\phi) = \sum_i a_i[\cos(\phi)]^i$

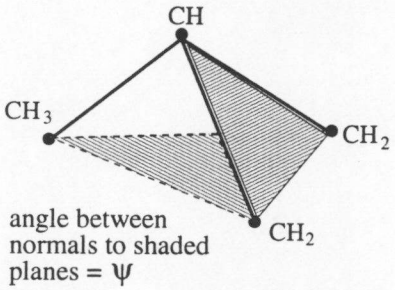

sp_3 bending $V_i(\psi) = \frac{-k_i}{2}(\psi - \psi_i)^2$

Figure 3.1: Intramolecular interaction potentials.

Table 3.2: Intramolecular interaction parameters

Potential Parameter	Value	Units
bond-stretching		
r_{eq}	1.54	Å
k_A/k_B	452 900	K/Å^2
bond-bending		
k_b/k_B	62 541	K/rad^2
θ_b	114.0	degrees
sp_3 inversion		
k_i	40 258.4	K/rad^2
θ_i	27.25	degrees
torsional $X - CH_2 - CH_2 - Y$		
a_0/k_B	1009.98	K
a_1/k_B	2018.96	
a_2/k_B	136.38	
a_3/k_B	-3165.32	
torsional $X - CH - CH_2 - Y$		
a_0/k_B	409.63	K
a_1/k_B	901.79	
a_2/k_B	195.76	
a_3/k_B	-1848.36	

where $\langle P_{xy} \rangle$ is the average of the xy-component of the pressure tensor P and $\dot{\gamma}$ is the strain rate characterizing the shear field. We have chosen the x-direction to be the flow direction and the y-direction to be the flow gradient direction, so $\dot{\gamma} = \partial u_x / \partial y$ where u_x is the streaming velocity in the x-direction. The first and second normal stress coefficients are calculated according to the equations

$$\Psi_1 = -\frac{\langle P_{xx} \rangle - \langle P_{yy} \rangle}{\dot{\gamma}^2} \tag{3.7}$$

and

$$\Psi_2 = -\frac{\langle P_{yy} \rangle - \langle P_{zz} \rangle}{\dot{\gamma}^2}. \tag{3.8}$$

Since the streaming velocity is applied to the atomic sites in our NEMD simulation, we calculate the pressure tensor P according to the atomic formalism:

$$PV = \sum_{i,a} m_{ia} \vec{v}_{ia} \vec{v}_{ia} + \frac{1}{2} \underbrace{\sum_{i,a} \sum_{j,b}}_{i \neq j} (\vec{r}_{ia} - \vec{r}_{jb}) \vec{f}_{ia,jb} + \sum_{i,a} \delta \vec{r}_{i,a} \vec{f}_{ia}^{(\text{intra})} \tag{3.9}$$

where indices i and j refer to molecules i and j; indices a and b refer to interaction sites a and b in molecules i and j, respectively; $\vec{f}_{ia,jb}$ is the interaction force between site a on molecule i and site b on molecule j; $\delta \vec{r}_{i,a}$ is the position vector of site a on molecule i relative to the center of mass of molecule i; $\vec{f}_{ia}^{(\text{intra})}$ is the total intramolecular force on site a of molecule i; and m_{ia}, $\vec{r}_{ia}$, and $\vec{v}_{ia}$ are the mass, position, and velocity, respectively, of the site a on molecule i. Since the total intramolecular force sums to zero for any given molecule, the last term in Equation 3.9 does not depend on the choice of origin in the determination of $\delta \vec{r}_{i,a}$.

3.2 Simulation method

The equations of motion used to simulate alkanes under planar Couette flow are the SLLOD equations [15] (incorporating a Nosé thermostat),

$$\dot{\vec{r}}_{ia} = \frac{\vec{p}_{ia}}{m_{ia}} + \dot{\gamma} y_{ia} \hat{x} \tag{3.10}$$

$$\dot{\vec{p}}_{ia} = \vec{F}_{ia} - \dot{\gamma} p_{y,ia} \hat{x} - \dot{\zeta} \vec{p}_{ia} \tag{3.11}$$

$$\dot{\zeta} = \frac{p_\zeta}{Q} \tag{3.12}$$

$$\dot{p}_\zeta = F_\zeta, \tag{3.13}$$

where $\vec{r}_{ia}$, $\vec{F}_{ia}$, and $\vec{p}_{ia}$ are the coordinates of, force on, and momentum of atom a in molecule i, y_{ia} and $p_{y,ia}$ are its y-components, and m_{ia} is the mass. The strain rate of the imposed shear field is denoted $\dot{\gamma}$, $\hat{x}$ is a unit vector in the x-direction, ζ, p_ζ, and Q are the variables related to the Nosé thermostat

$$F_\zeta = \sum_{i,a} \frac{p_{ia}^2}{m_{ia}} - 3Nk_BT \tag{3.14}$$

$$Q = 3Nk_BT\tau^2 \tag{3.15}$$

where τ is the Nosé thermostat time constant, T is the absolute temperature, and N is the total number of atoms in the system. The equations of motion were integrated using a multiple time step technique, the details of which can be found in the works of Tuckerman *et al.* [27] and Cui *et al.* [144]. All of the intramolecular interactions

were treated as fast motions (smaller time step of 0.47 fs) and the intermolecular interaction as the slow motion (larger time step of 2.35 fs).

Chapter 4

Results and discussion

This study of the rheology of chain molecules under shear has focused on two main aspects: linear and branched alkane chains of intermediate length (C_{30}) and a linear short-chain polyethylene (C_{100}). The C_{30} study focused on the comparative rheology of a linear alkane (*n*-triacontane) and two branched alkanes (9-*n*-octyldocosane and 2,6,10,15,19,23-hexamethyltetracosane which is commonly called squalane). The molecular architectures of the two branched alkanes are illustrated in Figure 4.1. The two branched alkanes were chosen because they are the only two non-ringed isomers of C_{30} for which experimental density and viscosity data [2] are available for comparison to and validation of our simulation results. Simulations were performed over a wide range of strain rates at the temperatures of 311 and 372 K to allow prediction of the kinematic viscosity index, a key performance measure used to categorize lubricants. Simulations for *n*-triacontane were only performed at 372 K since, experimentally, it is a solid at 311 K. In addition to the NEMD simulations, EMD simulations were performed if not already available in the literature (octyldocosane and triacontane) to provide additional data helpful in the rheological analysis. The demonstrated fea-

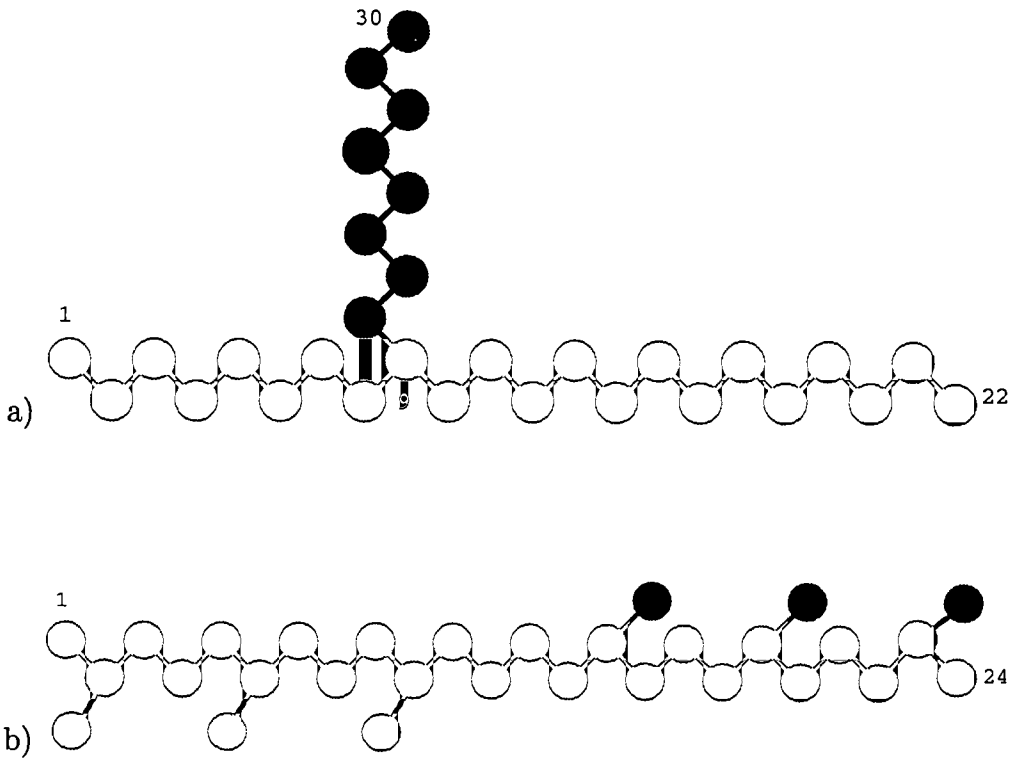

Figure 4.1: Branched alkanes studied. (a) 9-*n*-octyldocosane and (b) squalane.

sibility of EMD calculations on $C_{100}H_{202}$ [30, 31] provided impetus to perform NEMD simulations of C_{100} both under steady-state shear and constant-shear-rate start-up tests. C_{100} is long enough to be considered a short polymer, yet short enough that entanglement is not expected to be a factor in its rheology. The simulations were performed at 448 K since at that temperature experimental density, diffusion, and viscosity data were available for various linear polyethylenes [61]. The interesting behavior observed in the C_{100} simulations upon onset of shear prompted comparison to predictions from the Doi-Edwards model for entangled polymers as well as a study of shear-enhanced diffusion in the C_{100} system.

4.1 Isomers of $C_{30}H_{62}$

The constant-NVT simulations involved 100 $C_{30}H_{62}$ molecules (i.e. 3000 united atoms) at temperatures of 311 and 372 K and the corresponding experimental densities at 0.1 MPa pressure [2] (see Table 4.1). The density for n-triacontane at 372 K was estimated by interpolation between n-octadocosane and n-dotriacontane. Subsequent to equilibration, the equilibrium properties of the systems were accumulated as well as the nonequilibrium properties at reduced shear rates $\dot{\gamma}^* = \dot{\gamma}(m\sigma^2/\epsilon)^{1/2}$ranging from 0.0005 to 1.0 at which the results are not expected to depend significantly on the details of the thermostat [17, 151]).

This section is divided into two main subsections: Subsection 4.1.1 which describes equilibrium properties (4.1.1.1 translational diffusion and 4.1.1.2 rotational diffusion) and Subsection 4.1.2 which describes nonequilibrium properties (4.1.2.1 viscosity, 4.1.2.2 chain configurations and shear-induced alignment, and 4.1.2.3 energy and hydrostatic pressure).

Table 4.1: State points simulated

Molecule	T (K)	ρ (g/mL)
n-triacontane	372	0.7596
9-n-octyldocosane	311	0.7999
	372	0.7609
squalane	311	0.7979
	372	0.7592

4.1.1 Equilibrium properties

In addition to rheological properties, several equilibrium properties are also of interest, including the self-diffusion coefficient and rotational relaxation time. In particular, the rotational relaxation time is important because it aids in analyzing viscosity vs. strain rate data in terms of the critical strain rate for transition from Newtonian to non-Newtonian behavior [136, 152]. Also, both properties can be used in conjunction with results from the Rouse model [62] of unentangled polymer melts to predict the zero-shear viscosity for linear chains [19]. The average hydrostatic pressure (trace of the pressure tensor with no long-range corrections), squared radius of gyration, and percentage trans bonds data calculated by EMD are given in Table 4.2 including results for squalane reported by Mondello and Grest [78] (the numbers in parentheses represent the statistical uncertainty in the least significant digits). These values are averaged over runs of 4.0 ns for 9-n-octyldocosane at both temperatures and 3.3 ns for n-triacontane. The hydrostatic pressures of n-triacontane at 372 K and 9-n-octyldocosane at both temperatures are nearly equal (approximately 30MPa). Mondello and Grest interpreted the large negative pressure calculated for squalane as well as its temperature dependence as evidence of the limitations of the model used

Table 4.2: Equilibrium properties: average hydrostatic pressure, squared radius of gyration, and percentage trans bonds

	311 K			372 K		
Molecule	P (MPa)	R_g^2 (Å^2)	% Trans	P (MPa)	R_g^2 (Å^2)	% Trans
n-triacontane	-	-	-	31.6(3)	65.6(2)	69.5(1)
9-n-octyldocosane	30.0(6)	44.3(1)	67.9(1)	29.9(2)	43.1(1)	65.0(1)
squalane [78]	-66.2(6)	49.0(5)	-	-55.0(3)	46.0(3)	-

for squalane. For both 9-n-octyldocosane and squalane, the squared radius of gyration is somewhat smaller at 372 K than at 311 K. The increased flexibility at the higher temperature allows these relatively short and stiff chains to assume more compact conformations. At 372 K, 9-n-octyldocosane with its single long branch assumes the most compact conformation, n-triacontane is least compact, and squalane with its multiple methyl branches is slightly less compact than 9-n-octyldocosane.

4.1.1.1 Translational diffusion

The self-diffusion coefficients of the alkane melts are estimated from EMD simulations in terms of the limiting slope of the mean squared displacement (MSD) of the chain centers of mass as a function of time based on the Einstein relation

$$2tD = \frac{1}{3}\langle |r_i(t) - r_i(0)|^2 \rangle \tag{4.1}$$

where D is the self-diffusion coefficient and r_i is the position of the center of mass of molecule i. The notation $\langle ... \rangle$ is indicative of the fact that the MSD was averaged over the 100 molecules in each system as well as 1980, 7045, and 5550 different time origins and corresponding initial positions $r_i(0)$ for the 9-n-octyldocosane at 311 K, 9-n-octyldocosane at 372 K, and n-triacontane at 372 K runs, respectively. Each

time origin was separated from the previous one by 1.175 ps at 311 K and 0.47 ps at 372 K. In Figures 4.2 - 4.4, the MSD curves are plotted versus time for *n*-triacontane at 372 K and 9-*n*-octyldocosane at 311 and 372 K. The dashed lines are the simulation data, and the solid lines are fits to the data. The diffusion results (including results for squalane reported by Mondello and Grest [78]) are summarized in Table 4.3. The model overpredicts the experimental self-diffusion coefficients for squalane by approximately 30 % at these two temperatures [78]. The value predicted for *n*-triacontane is approximately 60 % larger than the experimental one [153]. Such overprediction of the self-diffusion coefficient is typical of the SKS united atom model. Better agreement with experiment for linear chains has been achieved [19, 78] by either introducing a displacement between the centers of force of nonbonded interactions and the centers of mass of the united atoms (the so-called "anisotropic united atom" model) [128, 129] or by using a different torsional parameterization and slightly larger LJ size parameter [46]. The author has been unable to find experimental data for the diffusivity of 9-*n*-octyldocosane.

Table 4.3: Equilibrium results: translational and rotational diffusion

	311 K			372 K		
Molecule	D (10^{-6} cm^2/s)	τ_1 (ns)	τ_2 (ns)	D (10^{-6} cm^2/s)	τ_1 (ns)	τ_2 (ns)
n-triacontane	-	-	-	5.92 [3.68][a]	0.44	0.21
9-*n*-octyldocosane	0.89	0.68	0.64	3.70	0.25	0.18
squalane [78]	0.62 [0.48][b]	2.85	2.24	3.39 [2.60][b]	0.46	0.19

a. number in brackets is the experimental value interpolated from data in [153]

b. number in brackets is the experimental value from [78]

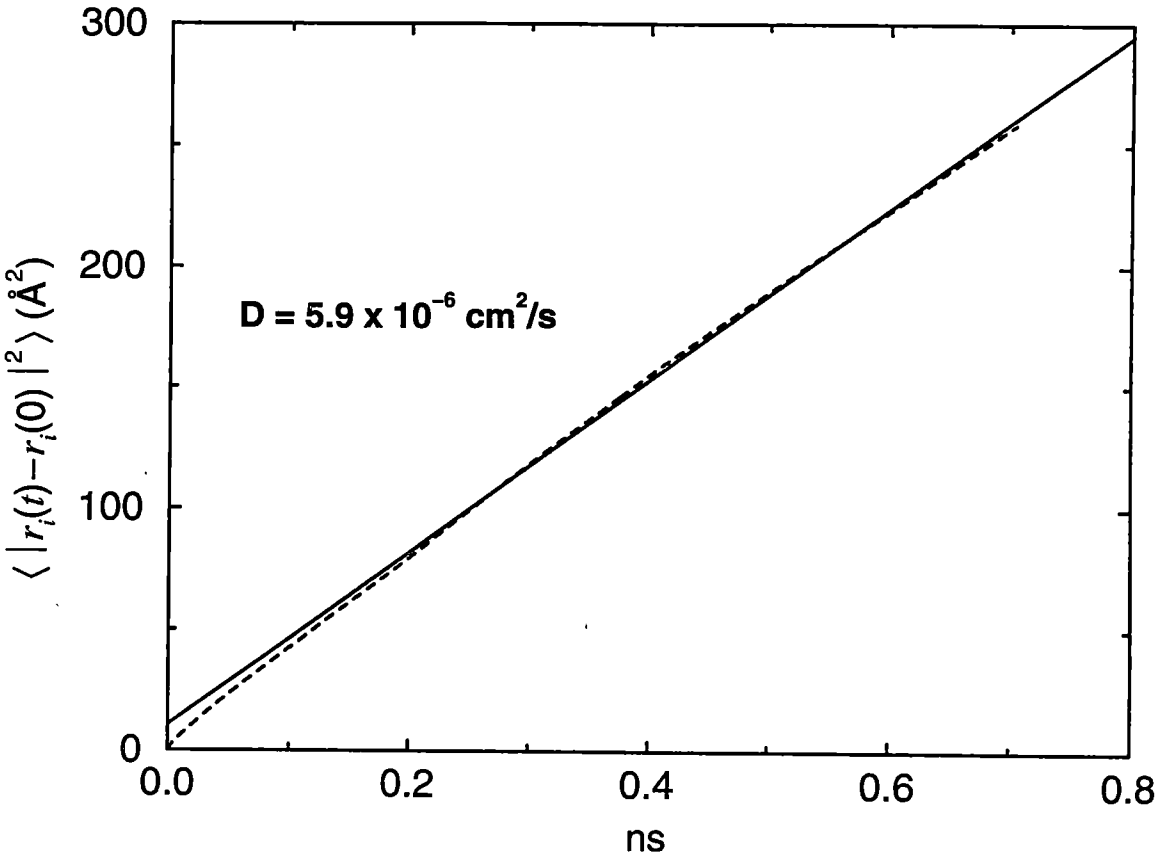

Figure 4.2: Average mean squared displacement of the centers of mass of the n-triacontane chains vs. time at 372 K. The dashed line is the simulation data, and the solid line is a fit to the data. The self-diffusion coefficient from the limiting slope is $D = 5.9 \times 10^{-6}$ cm^2/s.

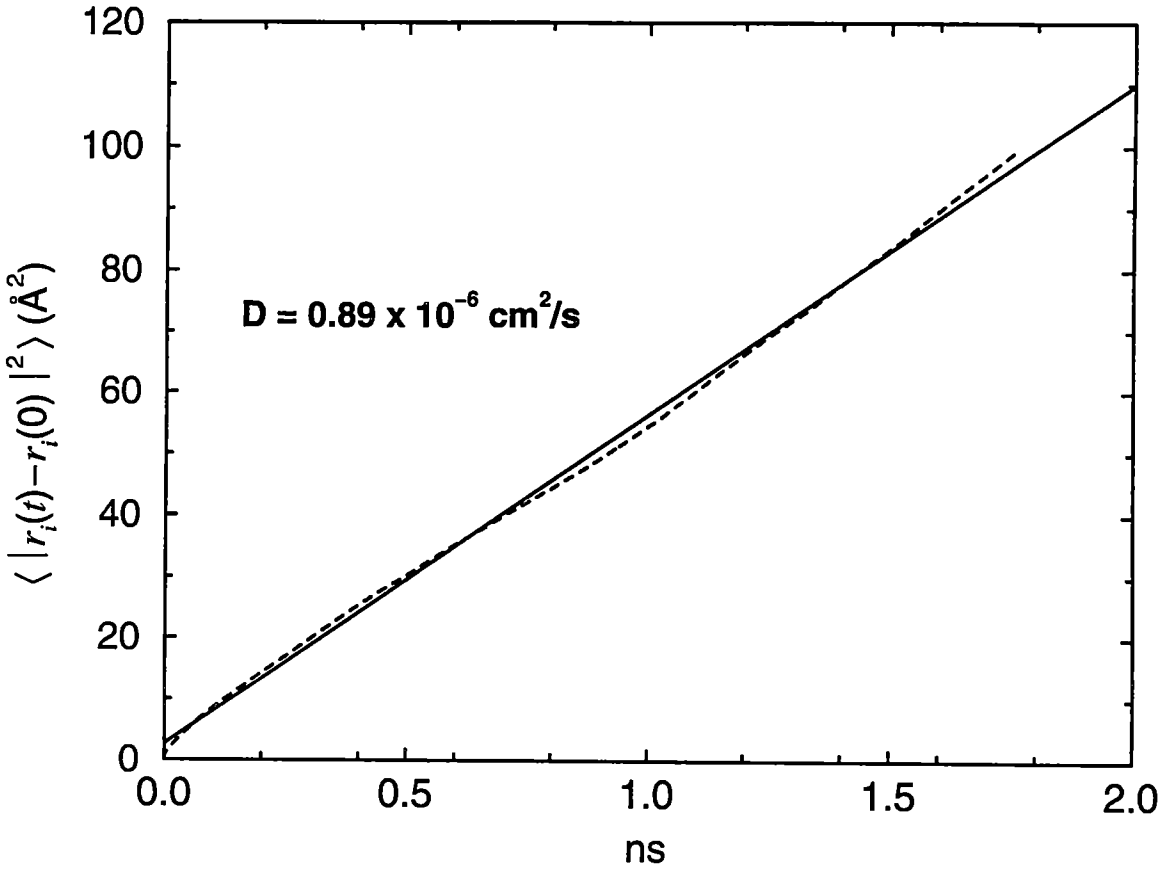

Figure 4.3: Average mean squared displacement of the centers of mass of the 9-*n*-octyldocosane chains vs. time at 311 K. The dashed line is the simulation data, and the solid line is a fit to the data. The self-diffusion coefficient from the limiting slope is $D = 0.89 \times 10^{-6}$ cm^2/s.

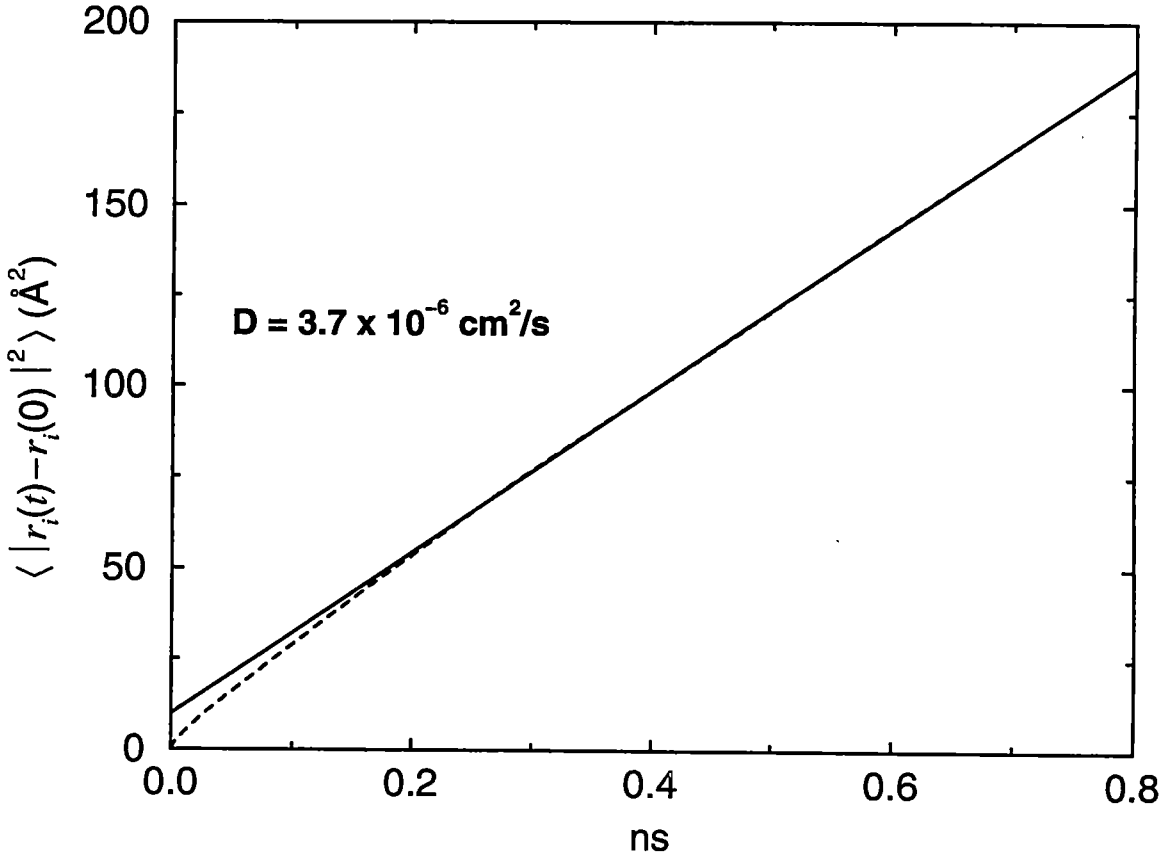

Figure 4.4: Average mean squared displacement of the centers of mass of the 9-*n*-octyldocosane chains vs. time at 372 K. The dashed line is the simulation data, and the solid line is a fit to the data. The self-diffusion coefficient from the limiting slope is $D = 3.7 \times 10^{-6}$ cm^2/s.

4.1.1.2 Rotational diffusion

The global rotational motion of the molecules is characterized by the orientational relaxation of the longest principal axis (e_1) of each molecule's ellipsoid of inertia. The first- and second-order angular correlation functions are given by

$$P_1^{e_1}(t) = \langle e_1(t) \cdot e_1(0) \rangle \tag{4.2}$$

and

$$P_2^{e_1}(t) = \frac{1}{2}(3\langle [e_1(t) \cdot e_1(0)]^2 \rangle - 1). \tag{4.3}$$

The same numbers and frequencies of time origins that were used for the translational diffusion calculations were also used for the rotational relaxation time calculations. Ignoring the short-time behavior, the functions exhibit exponential decay as seen in Figures 4.5 - 4.7 for the various molecules, and the results are summarized in Table 4.3. For isotropic rotational diffusion, $\tau_1/\tau_2 = 3$ is expected [154, 155]. For each case given in Table 4.3, τ_1/τ_2 is significantly less than 3, indicating that the orientational relaxation of the molecules is spatially constrained [156]. $\tau_1/\tau_2 \approx 2$ for squalane and n-triacontane at 372 K and approaches a value of 1 for squalane at 311 K and 9-n-octyldocosane at both temperatures. Previous NEMD studies [136, 152] have demonstrated that the transition from Newtonian to shear-thinning behavior of alkane liquids of length up to C_{24} occurs at a critical strain rate ($\dot{\gamma}_c$) approximately equal to $1/\tau_1$. Thus, our EMD results suggest that the transition to non-Newtonian behavior will occur at smaller strain rates for squalane than for 9-n-octyldocosane at both the temperatures studied, while at 372 K the transition should occur at approximately the same strain rate for squalane and n-triacontane.

Mondello and coworkers [19, 157] have compared the various estimates of the zero-

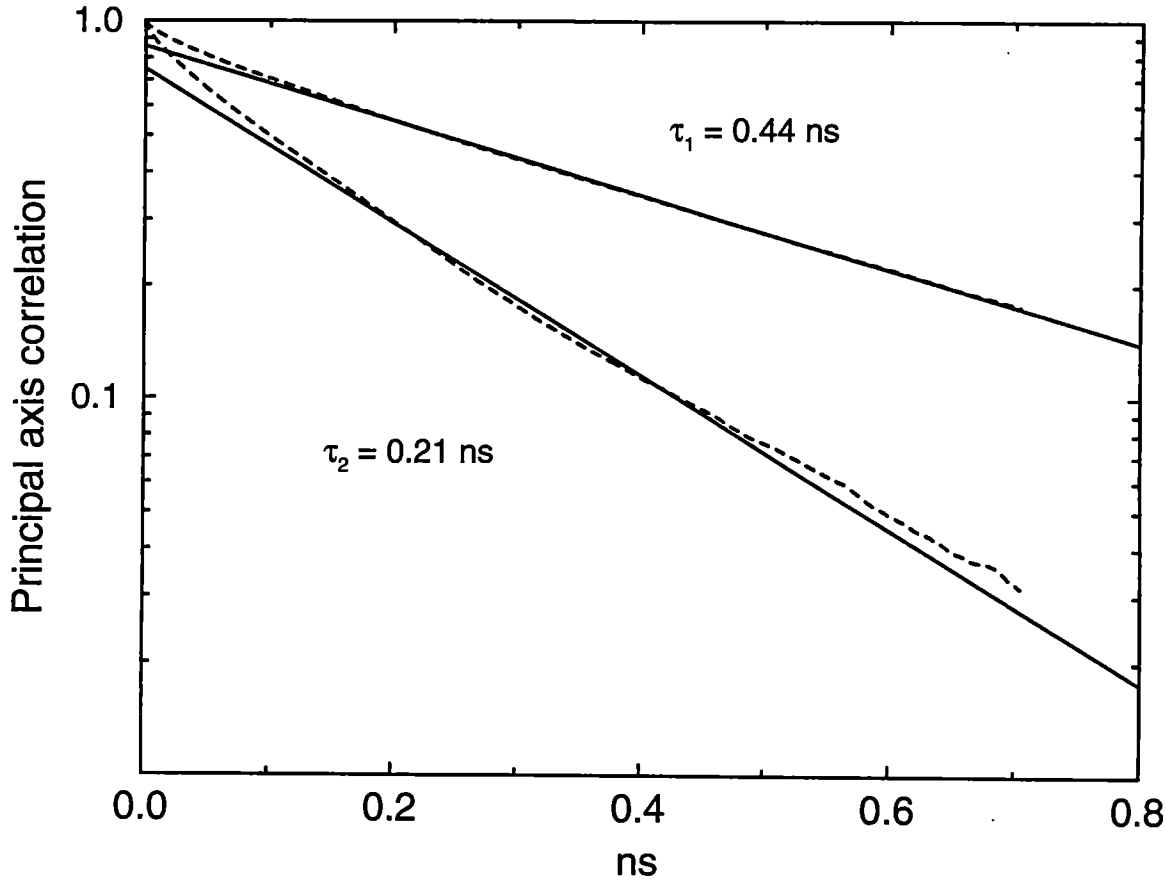

Figure 4.5: First- and second-order angular correlation functions vs. time for n-triacontane at 372 K. The dashed line is the simulation data, and the solid line is a fit to the data. The characteristic relaxation time of the first-order function is $\tau_1 = 0.44$ ns. The characteristic relaxation time of the second-order function is $\tau_2 = 0.21$ ns.

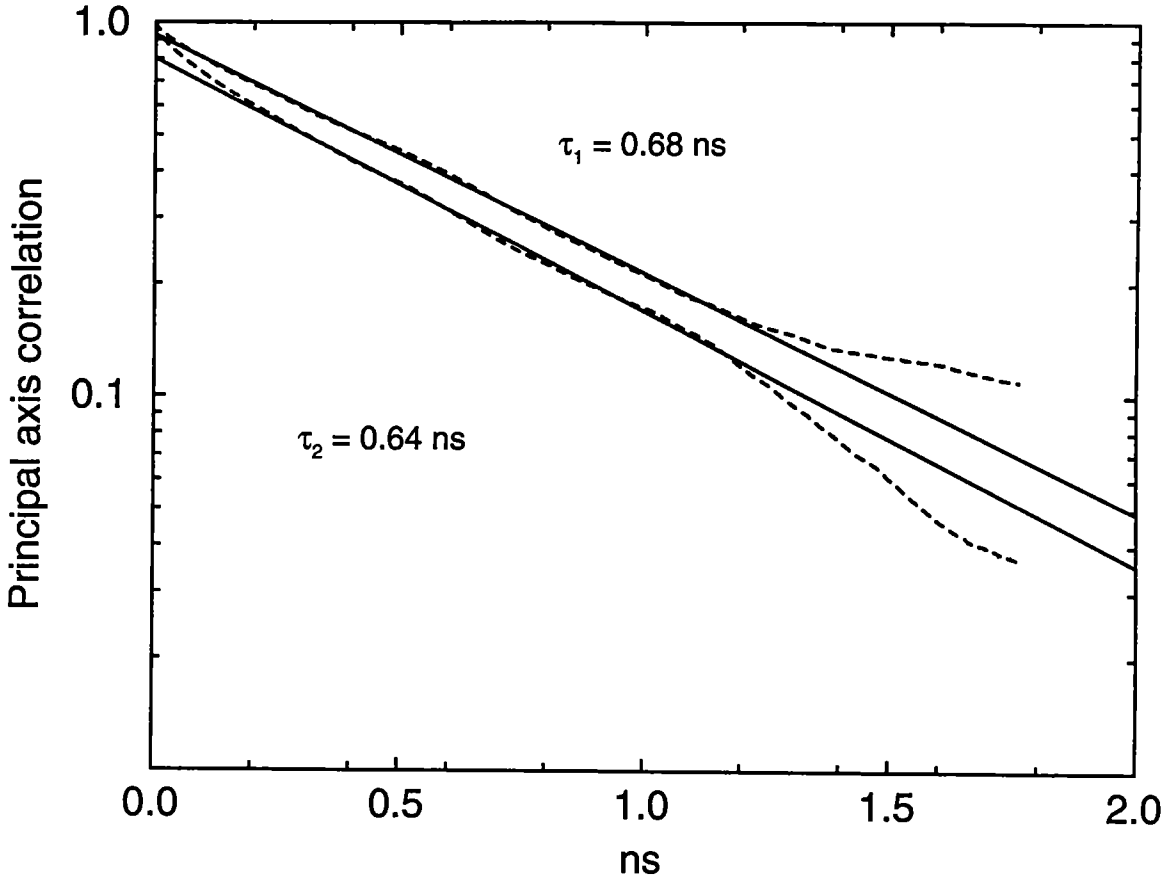

Figure 4.6: First- and second-order angular correlation functions vs. time for 9-*n*-octyldocosane at 311 K. The dashed line is the simulation data, and the solid line is a fit to the data. The characteristic relaxation time of the first-order function is $\tau_1 = 0.68$ ns. The characteristic relaxation time of the second-order function is $\tau_2 = 0.64$ ns.

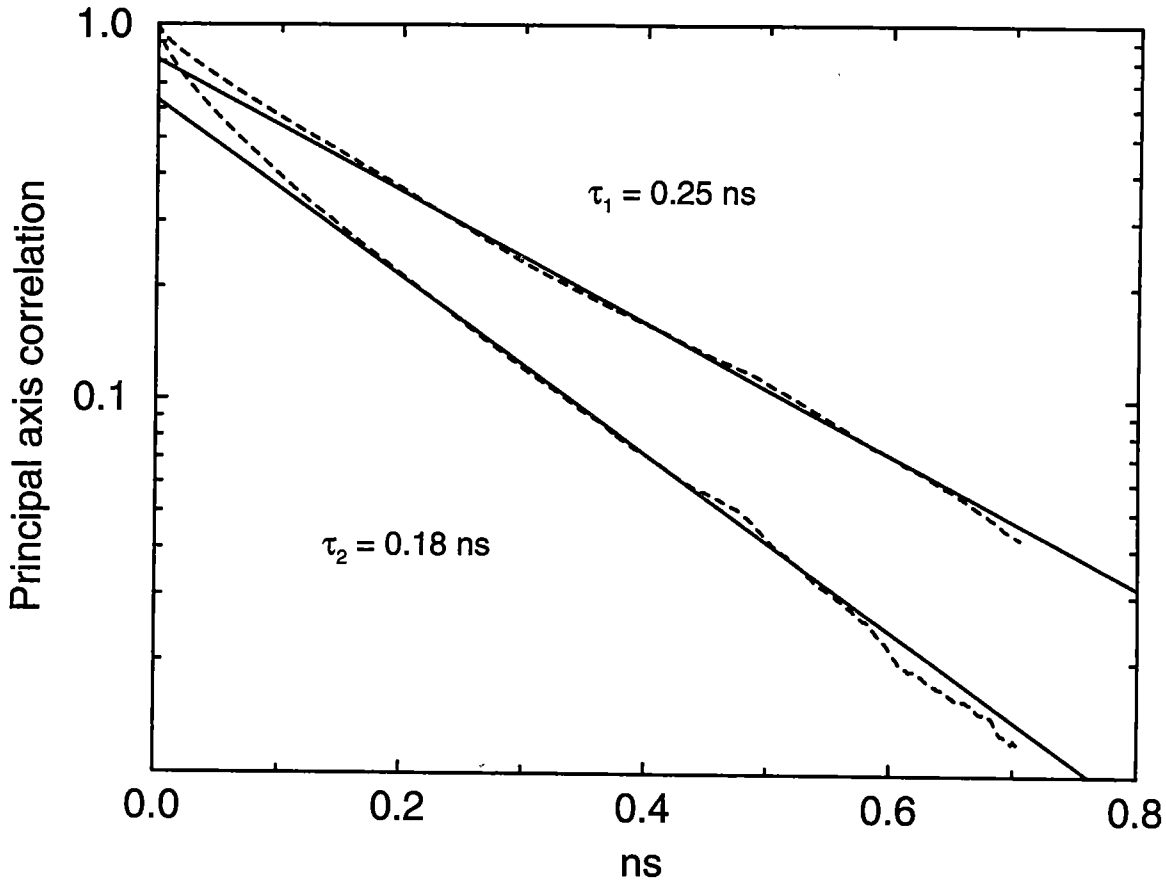

Figure 4.7: First- and second-order angular correlation functions vs. time for 9-*n*-octyldocosane at 372 K. The dashed line is the simulation data, and the solid line is a fit to the data. The characteristic relaxation time of the first-order function is $\tau_1 = 0.25$ ns. The characteristic relaxation time of the second-order function is $\tau_2 = 0.18$ ns.

shear viscosity based on the Rouse model (see Equations 2.28- 2.30) and properties from EMD simulations to the viscosity calculated by NEMD at a strain rate less than $\dot{\gamma}_c = \tau_1^{-1}$ for alkanes ranging from $C_{10}H_{22}$ to $C_{66}H_{134}$. They found that $\eta_D \approx \eta_{NEMD}$ only for C_{66} while $\eta_\tau \approx \eta_{NEMD}$ (within 20%) for all of the systems studied. Estimates of the zero-shear kinematic viscosity ($\nu = \eta/\rho$) of *n*-triacontane at 372 K using the properties from our EMD simulation are 2.66×10^{-6} m^2/s from Equation 2.28, 1.69×10^{-6} m^2/s from Equation 2.29, and 1.36×10^{-6} m^2/s from Equation 2.30.

4.1.2 Nonequilibrium properties

4.1.2.1 Viscosity

Kinematic viscosity is plotted in Figure 4.8 as a function of strain rate. Error bars are suppressed for clarity since they are smaller than the symbols except at certain of the lowest strain rates. In all cases, the viscosity shows shear thinning behavior over most of the range of strain rates and a Newtonian plateau at the lowest strain rates. The dashed lines extending from the symbols on the horizontal axis up to the filled triangles indicate τ_1^{-1} for the molecule and state corresponding to the symbol from which it extends. Thus, the transition from Newtonian to non-Newtonian behavior correlates well with the inverse of the rotational relaxation time. Though the Newtonian plateaus of *n*-triacontane and 9-*n*-octyldocosane are indistinguishable from each other at 372 K, their viscosities are clearly distinguishable in the shear thinning region, indicating that the transition to shear thinning occurs at a lower strain rate for *n*-triacontane than for 9-*n*-octyldocosane. This conclusion is also supported by the τ_1^{-1} data. The zero-shear viscosity in each case is estimated by averaging the values at strain rates which appear to fall within the Newtonian plateau. Each value in the plateau region is considered an independent prediction of the zero-shear viscosity, and

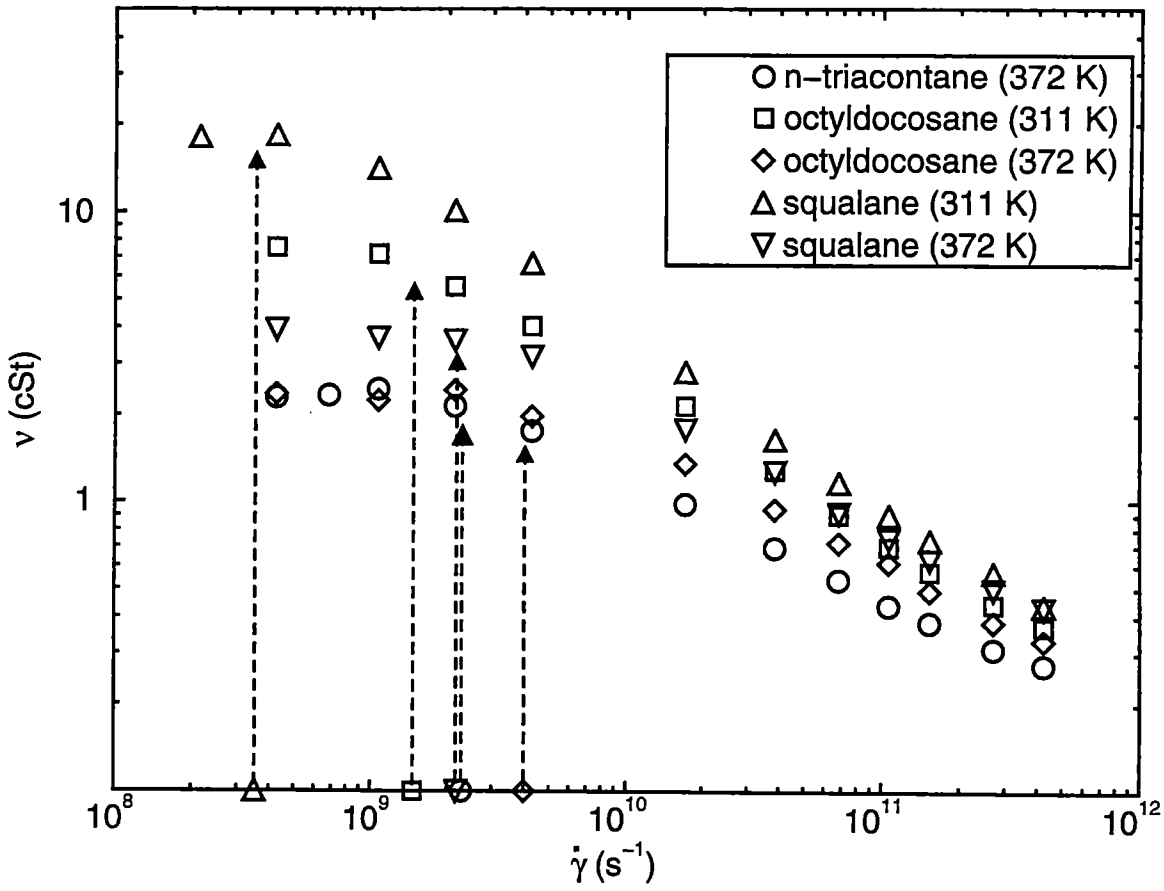

Figure 4.8: Kinematic viscosity vs. strain rate for *n*-triacontane, 9-*n*-octyldocosane, and squalane. The dashed lines extending from the symbols on the horizontal axis up to the filled triangles indicate τ_1^{-1} for the molecule and state corresponding to the symbol from which they extend.

the uncertainty in the zero-shear value is estimated by considering the scatter in the plateau viscosities relative to their average. The strain rates and viscosities considered to fall within the plateau region are given in Table 4.4, and the corresponding predictions of the zero-shear viscosity and kinematic viscosity index (VI) are given in Table 4.5 along with the experimental values. The experimental zero-shear viscosity for n-triacontane was estimated by interpolation between n-octadocosane and n-dotriacontane. The kinematic viscosity index (VI) is a widely-used industrial characterization of automotive lubricants. Based on the kinematic viscosity of the oil at 40 and 100 °C, the VI is an attempt to quantify an oil's viscosity-temperature behavior. The higher a lubricant's viscosity index, the less the lubricant's viscosity varies with temperature. VI values in Table 4.5 were calculated according to the ASTM standard (ASTM D2270-93 and ASTM D341-93). The uncertainty in the VI values was estimated by propagating the uncertainty in the zero-shear viscosities (assumed to be 5 % in for the experimental measurements). Compared to experiment, the united atom model underpredicted the kinematic viscosities of n-triacontane and 9-n-octyldocosane but accurately predicted the values for squalane (within 15 %). In addition, the VI values predicted by NEMD and the united atom model are in quantitative agreement with experiment. That is, even though the united atom model did not accurately predict the viscosities for 9-n-octyldocosane, it still did an excellent job of predicting the dependence of its viscosity on temperature. Also, the zero-shear viscosity for n-triacontane predicted from the value of τ_1 from simulation and results from the Rouse model was within 16 % of the value determined by NEMD.

In Figure 4.8 the ν versus $\dot{\gamma}$ curves exhibit a clear trend, though quite widely separated at low strain rate (except for n-triacontane in comparison to 9-n-octyldocosane at 372 K), to converge in the limit of high strain rate. Such a trend has been observed in simulations of alkanes [18] and experimentally for various silicone oils [158]

Table 4.4: Shear rates within the Newtonian plateau

Molecule and State	Strain Rate (s^{-1})	Reduced Strain Rate $\dot{\gamma}(m\sigma^2/\epsilon)^{1/2}$	Kinematic Viscosity (10^{-6} m^2/s)	Run Length (ns)
n-triacontane	4.251×10^8	0.001	2.29(18)	21.7
372 K	6.809×10^8	0.0016	2.33(14)	14.3
	1.063×10^9	0.0025	2.44(9)	12.7
	2.126×10^9	0.005	2.14(5)	14.0
9-n-octyldocosane	4.251×10^8	0.001	7.53(30)	15.8
311 K	1.063×10^9	0.0025	7.16(21)	6.4
9-n-octyldocosane	4.251×10^8	0.001	2.35(21)	19.8
372 K	1.063×10^9	0.0025	2.23(12)	9.4
	2.126×10^9	0.005	2.42(11)	3.2
squalane	2.126×10^8	0.0005	18.1(28)	9.4
311 K	4.251×10^8	0.001	18.3(17)	7.0
squalane	4.251×10^8	0.001	3.93(48)	4.6
372 K	1.063×10^9	0.0025	3.79(46)	4.5
	2.126×10^9	0.005	3.55(13)	5.4

Table 4.5: Zero-shear viscosities and VI

Molecule and Source	Kinematic Viscosity (10^{-6} m^2/s) 311 K	Kinematic Viscosity (10^{-6} m^2/s) 372 K	Kinematic Viscosity Index
n-triacontane NEMD	-	2.3 ± 0.1	-
n-triacontane expt. [2]	-	4.4 ± 0.2	-
9-n-octyldocosane NEMD	7.3 ± 0.2	2.3 ± 0.1	153 ± 34
9-n-octyldocosane expt. [2]	14.4 ± 0.7	3.6 ± 0.2	143 ± 45
squalane NEMD	18.2 ± 0.1	3.8 ± 0.2	103 ± 18
squalane expt. [2]	20.9 ± 1.0	4.2 ± 0.2	116 ± 30

and polystyrene solutions [159]. The power law exponents of the shear thinning region are -0.40 (n-triacontane, $T = 372$ K), -0.55 (9-n-octyldocosane, $T = 311$ K), -0.44 (9-n-octyldocosane, $T = 372$ K), -0.59 (squalane, $T = 311$ K), and -0.45 (squalane, $T = 372$ K). Since the curves tend to converge at high strain rates, the power law exponents are necessarily larger at the lower temperature (where the zero-shear viscosities are higher). Kinematic viscosity divided by zero-shear kinematic viscosity versus $\dot{\gamma}\tau_1$ is plotted in Figure 4.9. As is evident from this figure, except for values of the zero-shear viscosity and rotational relaxation time, the ν versus $\dot{\gamma}$ curves vary little with molecular architecture at a single temperature. Comparing the basic curve shapes at the two temperatures, the primary effect of decreasing temperature is to strengthen the shear thinning behavior (i.e. larger magnitude of the power law exponent).

The fact that the united atom model predicted quantitatively accurate zero-shear viscosities for squalane but significantly underpredicted those of n-triacontane and 9-n-octyldocosane (performance more typical of united-atom-model predictions of

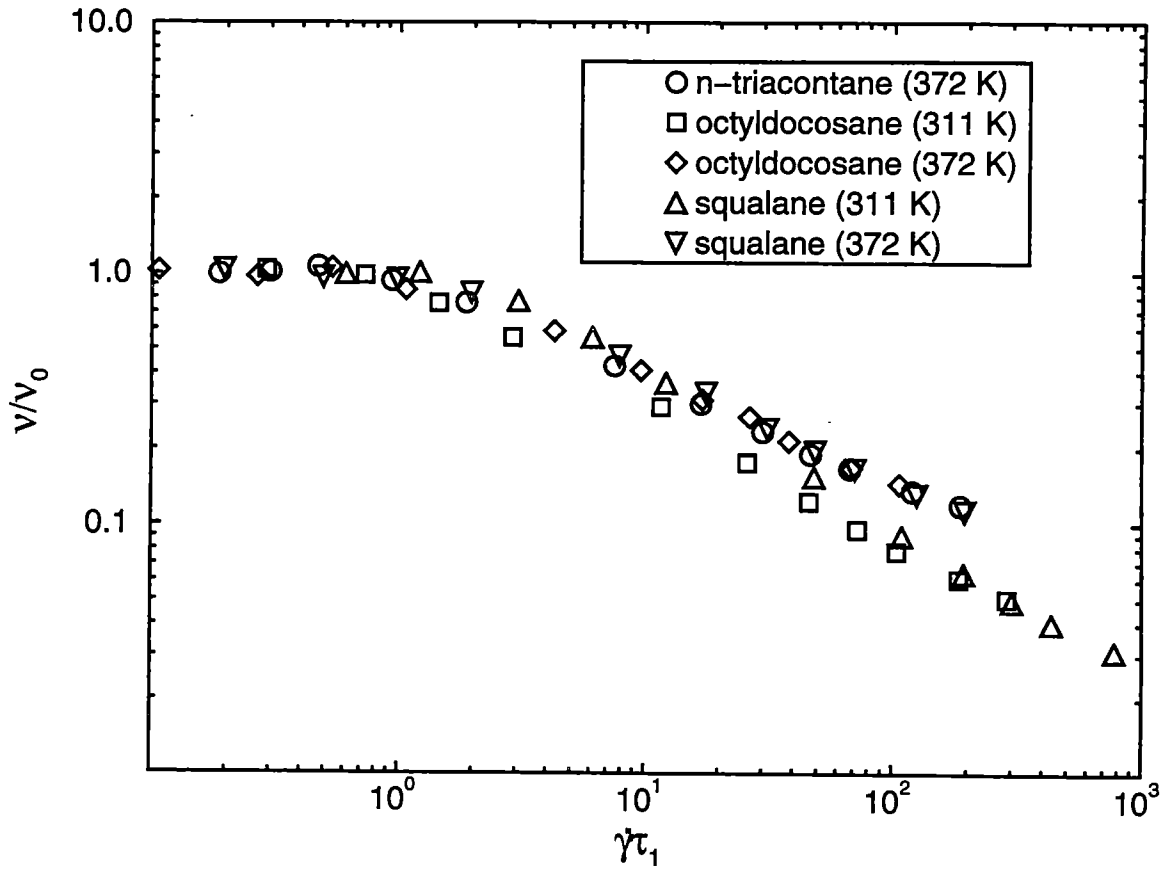

Figure 4.9: Kinematic viscosity divided by zero-shear kinematic viscosity vs. $\dot{\gamma}\tau_1$ for *n*-triacontane, 9-*n*-octyldocosane, and squalane.

alkane viscosities) merits some further discussion. Allen and Rowley [148] hypothesized that the common deficiency of united atom models in predicting alkane viscosities may be due in part to their inability to model the additional drag caused by the interaction of hydrogen atoms on molecules in different velocity layers as they shear past one another; that is, in some sense, the "smoothness" in the united atom representation of alkanes introduced by not explicitly modeling the hydrogens leads to underprediction of alkane viscosities. We have considered the possibility that the "knobby-ness" of squalane's molecular architecture caused by the six methyl sidebranches somehow alleviated this "smoothness" problem leading to quantitatively accurate viscosity predictions for squalane. However, this explanation is inconsistent with the observations of Mundy *et al.* [20] who performed simulations of squalane (T = 450 K, P = 1 atm) using a different extension of the SKS model to branched alkanes ($\sigma_{CH_3} = \sigma_{CH_2}$ = 3.93 Å, σ_{CH} = 3.85 Å, ϵ_{CH_3}(methyl sidechain) = 78 K, ϵ_{CH_2} = 47 K, ϵ_{CH} = 32 K) [80]. At least in the limit of low strain rate, they were unable to observe a statistical difference between the viscosity of squalane and that of n-triacontane (simulated at the same T and P). In a note added in proof [80], Siepmann *et al.* provided revised parameters for branched alkanes (σ_{CH_3} = 3.77 Å, σ_{CH_2} = 3.93 Å, σ_{CH} = 4.1 Å, ϵ_{CH_3} = 98.1 K, ϵ_{CH_2} = 47 K, and ϵ_{CH} = 12 K). We have performed a simulation of squalane (T = 372 K, $\dot{\gamma} = 1.063 \times 10^9$ s^{-1}) using this latter LJ parameterization for comparison. Compared to the parameterization due to Mondello and Grest at the same strain rate (R_g^2 = 48.7 Å, P = −31.5 MPa, $\nu = 3.6 \times 10^{-6}$ m^2/s), this LJ parameterization for squalane yielded a somewhat smaller R_g^2 and significantly different pressure and kinematic viscosity (R_g^2 = 45.5 Å, P = 37.2 MPa, $\nu = 2.3 \times 10^{-6}$ m^2/s). Thus, it seems probable that the success of Mondello and Grest's parameterization for squalane is due to their use of the large methyl energy parameter from SKS (for normal alkanes, ϵ_{CH_3} = 114 K) as the energy parameter for

the many methyl branches of squalane. Use of either of the smaller methyl energy parameters from parameterizations for branched alkanes (ϵ_{CH_3}(methyl branch) = 78 K or ϵ_{CH_3} = 98.1 K) evidently lead to viscosity predictions in poorer agreement with experiment for squalane itself but which are more consistent with the performance of the model for other linear and branched alkanes. This is consistent with the observation of Lahtela *et al.* that small changes in the intermolecular potential parameters of the branched methyl group in 3-methylhexane produced large changes in viscosity [147]. Martin and Siepmann have recently revised their united atom model for branched alkanes [88], but quantitative viscosity predictions will likely require either an explicit atom model (Chen and Siepmann have recently published such a model for normal alkanes [89]) or an anisotropic united atom (AUA) potential. However, Green-Kubo calculations by Mondello and Grest suggest that the AUA potential of Toxvaerd does not perform significantly better than SKS in terms of viscosity predictions (using the Green-Kubo relation) for normal alkanes of length up to $C_{16}H_{34}$ despite the AUA's superior performance in terms of the self-diffusion coefficient.

4.1.2.2 Chain configurations and shear-induced alignment

Molecular configurations and alignment in these alkane systems show significant strain-rate-dependence at the high rates of shear covered in this study. The squared radius of gyration as a function of $\dot{\gamma}$ divided by its average value for $\dot{\gamma} < \tau_1^{-1}$ is plotted in Figure 4.10. We chose to normalize by the low-$\dot{\gamma}$ values rather than the equilibrium ones because otherwise we would have to rely on the EMD results of Mondello and Grest which yielded R_g^2 values for squalane somewhat smaller than the low-$\dot{\gamma}$ values determined from our simulations. Previously [18], Cui *et al.* attributed the small difference between their low-$\dot{\gamma}$ R_g^2 for *n*-decane and the EMD value of Mondello

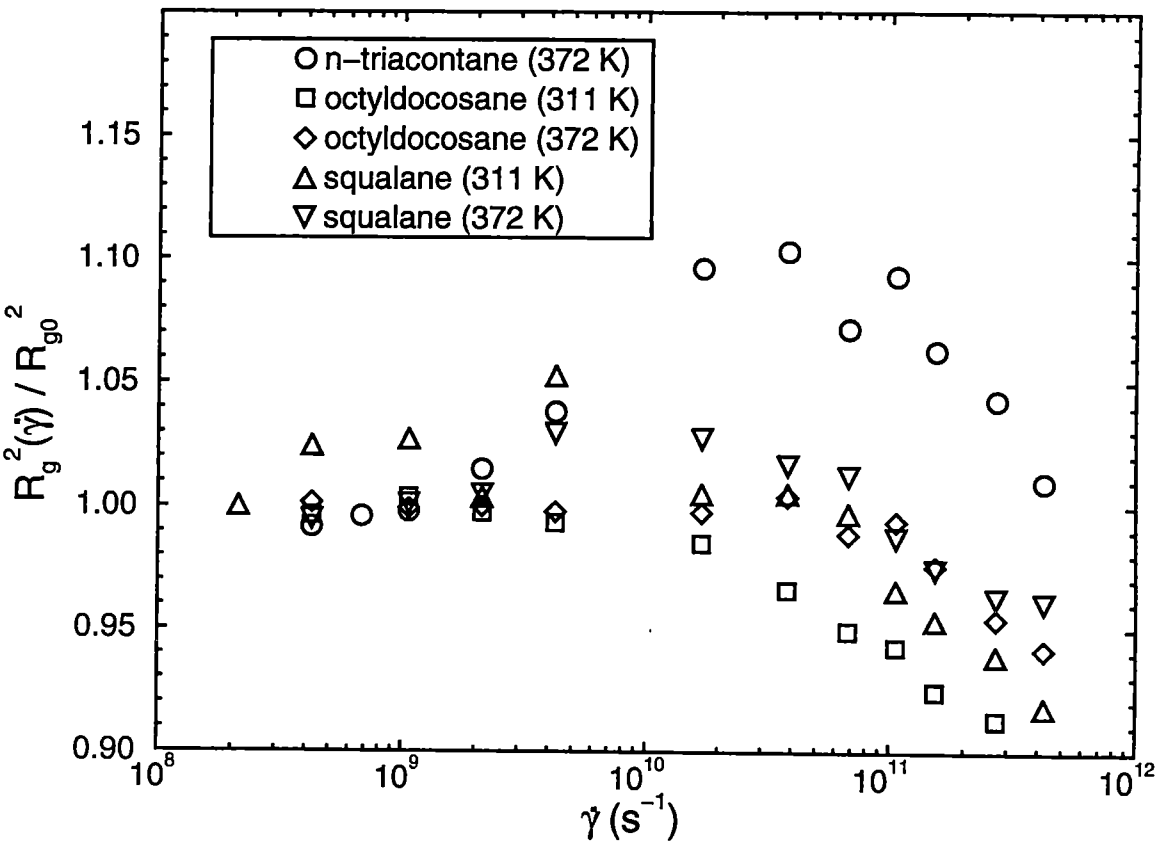

Figure 4.10: Squared radius of gyration (R_g^2) divided by its value at low shear rate (R_{g0}^2) vs. $\dot{\gamma}$ for n-triacontane, 9-n-octyldocosane, and squalane plotted as a function of strain rate.

and Grest to the slightly increased flexibility of the model due to the bond vibrational potential used by Cui *et al.* and in the present work. Consistent with the conclusions of previous NEMD studies of alkanes [16, 18, 21, 136, 145], R_g^2 for the linear alkane shows a maximum at intermediate strain rates. As was also observed by Khare *et al.* for 5,12-dipropylhexadecane [21], R_g^2 for 9-*n*-octyldocosane does not show a maximum as a function of $\dot{\gamma}$. Squalane, with its many short side-branches, shows a slight maximum in R_g^2, behavior intermediate between that of the long, linear alkane and the long-branched alkane. Padilla and Toxvaerd [145] rationalized the occurrence of a maximum in R_g^2 as a competition between two mechanisms to relieve chain tension due to chains traversing multiple shear planes in the shear field: alignment of the chains with the flow field (the dominant mechanism at the lower strain rates) and deformation of the chain (the dominant mechanism at the higher strain rates). In each case in Figure 4.10, the average chain dimension decreases with increasing $\dot{\gamma}$ at high $\dot{\gamma}$. Since the presence of branches would inherently hinder the ability to minimize a chain's exposure to multiple shear planes, it may not be surprising that the variation of R_g^2 with $\dot{\gamma}$ is less dramatic for the branched alkanes. In all cases the variation is fairly modest: at most a 10% increase or decrease.

One measure of the structural order in the system is the order tensor, which is defined as [160, 161]

$$S = \frac{3}{2}\langle \frac{1}{N}\sum_{i=1}^{N}(e_i e_i - \frac{1}{3}l)\rangle \tag{4.4}$$

where e_i is the unit vector along the end-to-end direction of the molecule i, l is a second-rank tensor with a value of 0 for the off-diagonal elements and a value of 1 for the diagonal elements, and the summation is over all N molecules in the system. The angle braces indicate an ensemble average. The eigenvector corresponding to

the largest eigenvalue (the order parameter) of the order tensor gives the preferential orientation of the molecules relative to the flow field. This alignment angle is plotted versus strain rate in Figure 4.11. Clearly, shear thinning in these systems is accompanied by the alignment of molecules with the flow direction. At low $\dot{\gamma}$, the alignment angle increases with decreasing $\dot{\gamma}$ as it approaches linear-regime behavior. At high $\dot{\gamma}$, it approaches a small limiting value between 6 and 11°. Cui *et al.* [152] associated the sharp decrease in the alignment angle with the transition from Newtonian to shear-thinning behavior and observed that the limiting value of the angle at high $\dot{\gamma}$ is dependent on the length of the molecule's backbone. This observation is confirmed here for the *n*-$C_{30}H_{62}$ isomers; as the chain-backbone length increased from 9-*n*-octyldocosane to squalane to *n*-triacontane, the limiting alignment angle decreased from approximately 10.5 to 7.7 to 6.8 °. Cui *et al.* suggested that this trend results from the need of longer molecules to better align with the flow field in order to dissipate the viscous force among them. The limiting high-$\dot{\gamma}$ value of the alignment angle is seen here to vary only slightly with temperature for the same molecule; for both 9-*n*-octyldocosane and squalane, the angle at 372 K is only slightly larger than the value at 311 K.

4.1.2.3 Energies and hydrostatic pressure

In Figures 4.12 - 4.15, the various average potential energies per molecule are plotted as a function of strain rate. At low strain rate, in most cases, the average energies vary over a fairly wide range. In contrast, at high strain rates the curves exhibit a certain amount of convergence; the bond-stretching + intramolecular-LJ energies and bond-angle-bending energies are segregated according to temperature while the torsional and intermolecular-LJ are segregated according to molecular identity. In

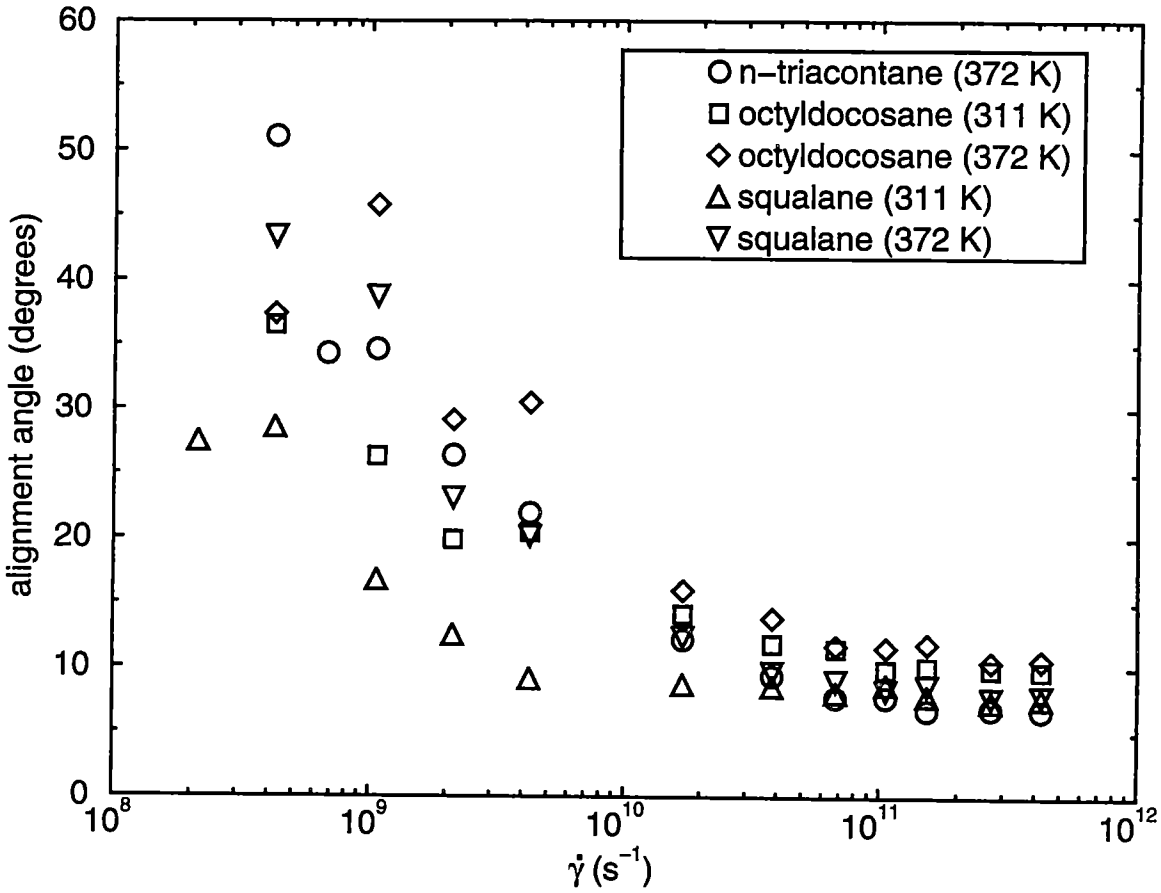

Figure 4.11: The alignment angle with the flow field of the end-to-end vector for n-triacontane and of the backbone of 9-n-octyldocosane and squalane.

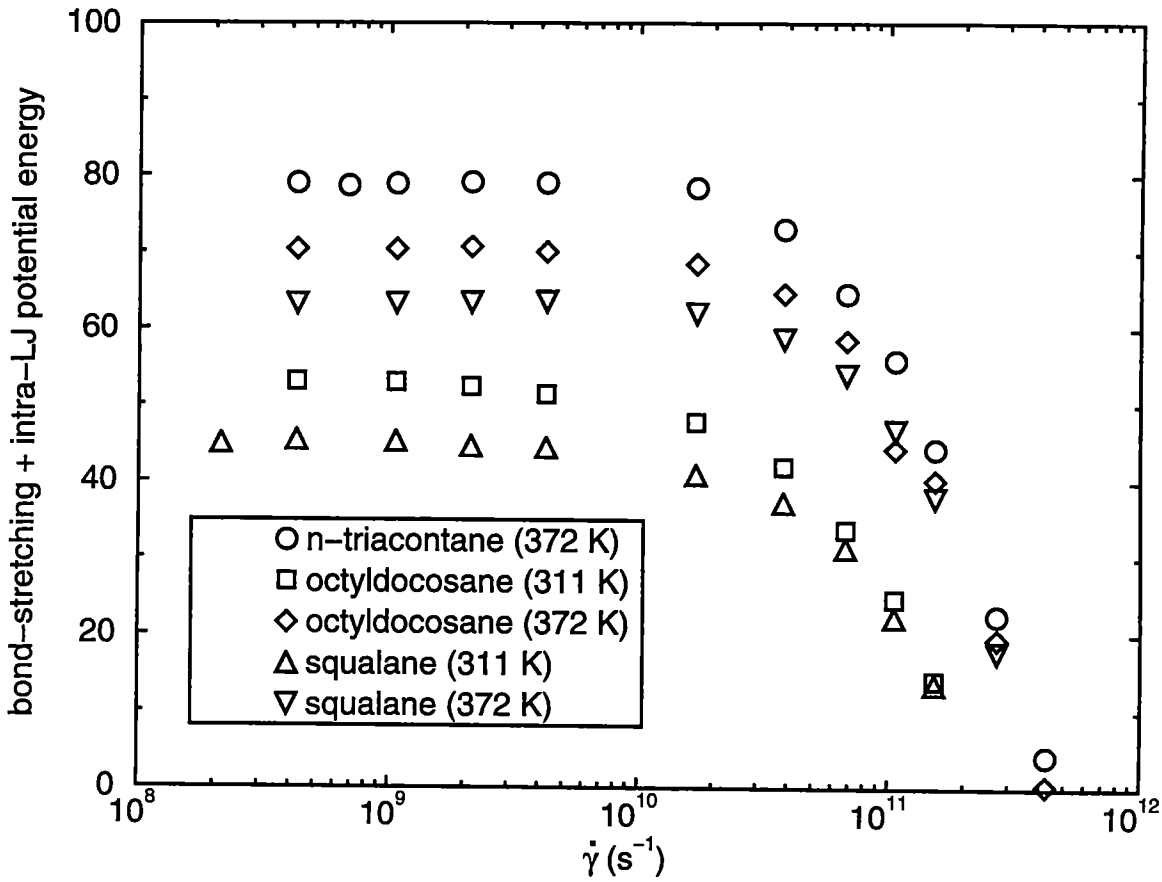

Figure 4.12: Bond-stretching + intramolecular LJ potential energy per molecule (reduced units) as a function of $\dot{\gamma}$ for n-triacontane at 372 K.

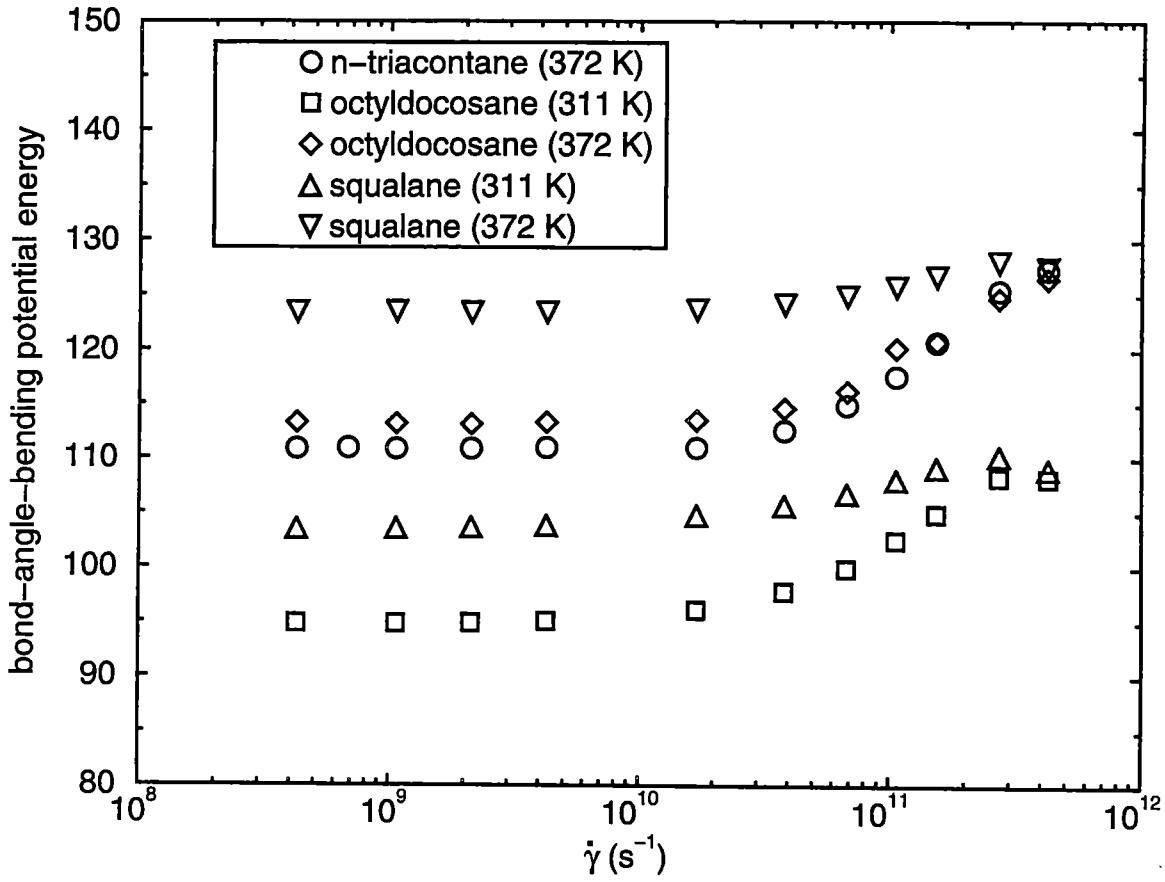

Figure 4.13: Bond-angle-bending potential energy per molecule (reduced units) as a function of $\dot{\gamma}$ for n-triacontane at 372 K.

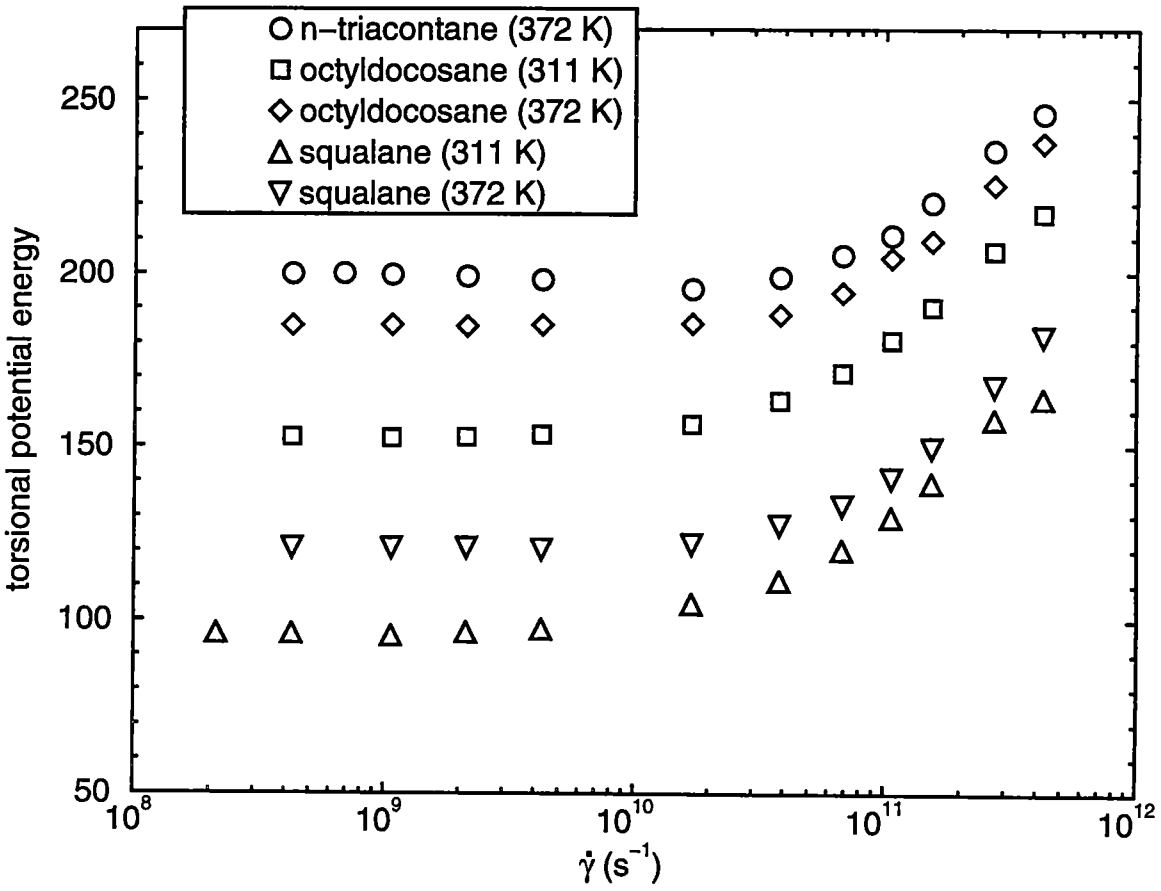

Figure 4.14: Torsional potential energy per molecule (reduced units) as a function of $\dot{\gamma}$ for n-triacontane at 372 K.

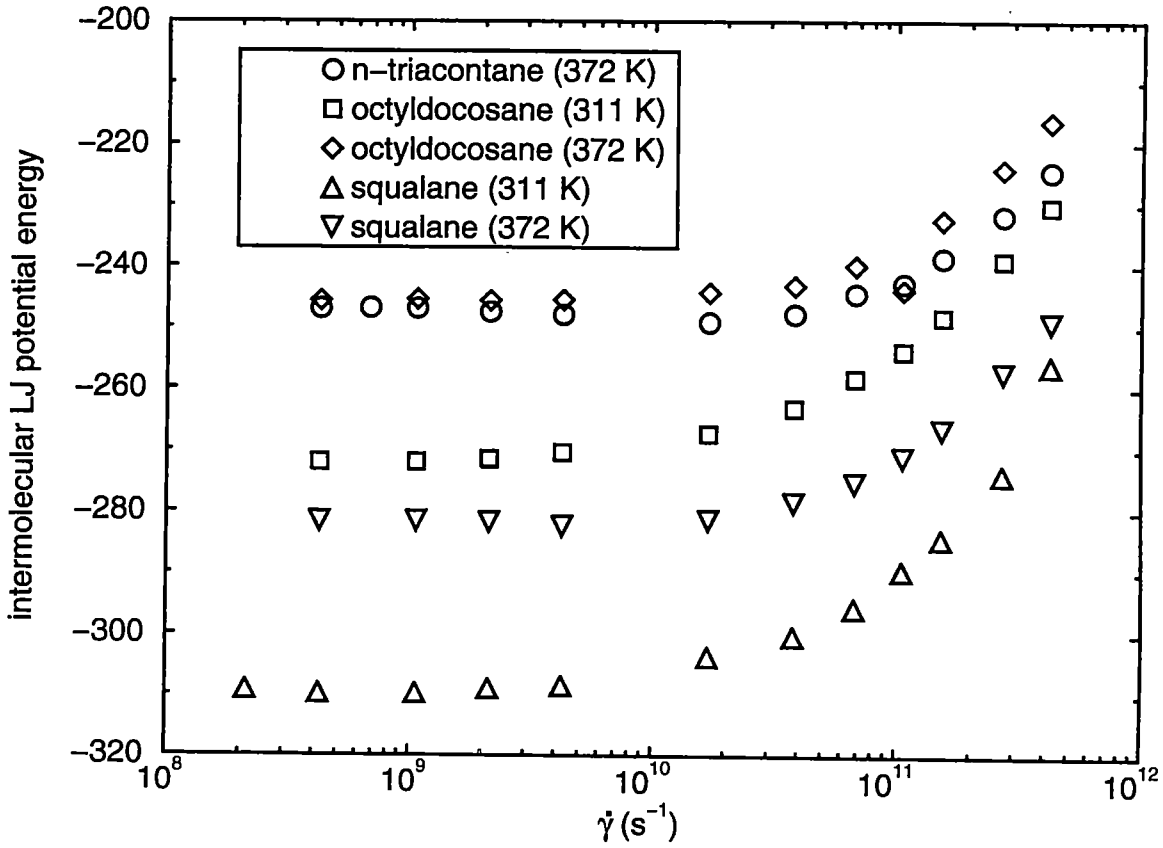

Figure 4.15: Intermolecular LJ potential energy per molecule (reduced units) as a function of $\dot{\gamma}$ for n-triacontane at 372 K.

Figure 4.16, the hydrostatic pressure is plotted vs. strain rate. Shear dilatancy is seen at high rates of shear in all cases with P $\propto \dot{\gamma}^p$ where p is equal to 0.57 (n-triacontane, 372 K), 0.52 (9-n-octyldocosane, 311 K), 0.54 (9-n-octyldocosane, 372 K), 1.15 (squalane, 311 K), and 1.53 (squalane, 372 K). Such a variety in the shear dilatancy is consistent with previous simulation studies that have yielded a diversity of results for alkanes [16, 18, 136, 138, 144]. Though not particularly obvious in Figures 4.15 and 4.16, both the intermolecular-LJ energy and hydrostatic pressure of n-triacontane pass through minima at $\dot{\gamma} = 1.70 \times 10^{10}$ s^{-1}. Khare *et al.* observed similar behavior for n-octacosane [21]. These minima seem to occur at or just prior to the strain rate corresponding to the maximum in R_g^2 and are only observed for the normal alkanes.

4.2 Linear short-chain polyethylene

This section is divided into three main subsections: Subsection 4.2.1 which describes equilibrium properties (4.2.1.1 average chain dimensions, 4.2.1.2 translational diffusion, and 4.2.1.3 rotational diffusion), Subsection 4.2.2 which describes steady-state properties under planar Couette flow (4.2.2.1 viscometric properties, 4.2.2.2 average chain dimensions and shear-induced alignment, 4.2.2.3 hydrostatic pressure and potential energy, and 4.2.2.4 shear-enhanced self-diffusion), and Subsection 4.2.3 which describes the transient behavior upon onset of shear(4.2.3.1 stress overshoot: molecular-level origins, 4.2.3.2 stress overshoot: strain-rate dependence, 4.2.3.3 stress overshoot: chain-length dependence, and 4.2.3.4 stress overshoot: shear-induced ordering). The constant-NVT simulations involved either 200 (EMD) or 400 (NEMD) $C_{100}H_{202}$ molecules (i.e. 20,000 or 40,000 united atoms) at a temperature of 448 K and $\rho = 0.75$ g/mL, estimated from the data in Pearson *et al.* [61]. The 200-molecule sim-

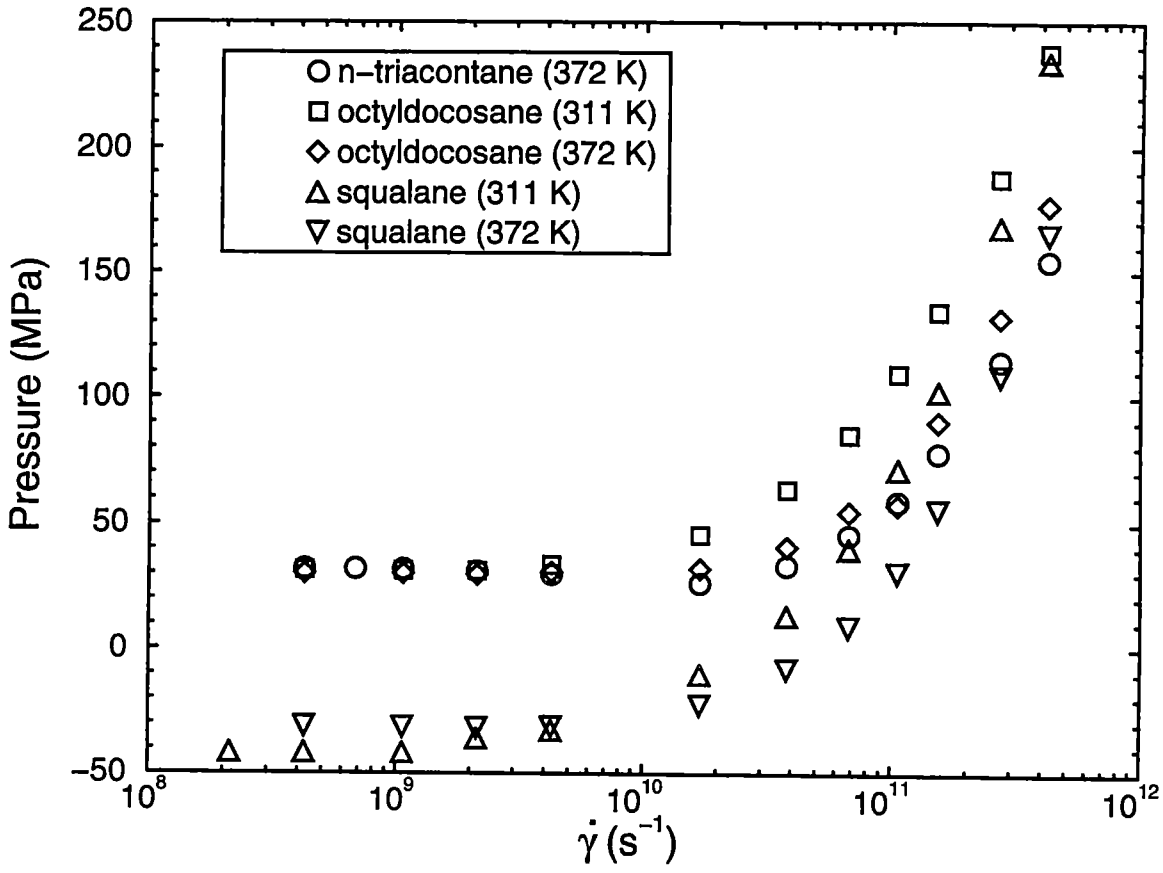

Figure 4.16: Hydrostatic pressure as a function of $\dot{\gamma}$ for *n*-triacontane, 9-*n*-octyldocosane, and squalane at 372 K.

ulation involved a cubic box with a boxlength of 85.3 Å. The 400-molecule simulation involved a box 85.3 Å in the y- and z-directions but 170.6 Å in the x-direction (i.e. the flow direction). The system was equilibrated for 7 ns. Subsequent to equilibration, the equilibrium properties of the system were accumulated over a period of 5.6 ns as well as the nonequilibrium properties at at reduced shear rates $\dot{\gamma}^* = \dot{\gamma}(m\sigma^2/\epsilon)^{1/2}$ ranging from 0.00036 to 1.0 at which the results are not expected to depend significantly on the details of the thermostat [17, 151]). The initial 400-molecule configuration was generated by simply replicating the equilibrated 200-molecule configuration in the x-direction.

The united atom potential model parameters used in the two EMD studies mentioned previously (HMT [31] and PSY [46]) are summarized in comparison to SKS in Tables 4.6 and 4.7. Note that Theodorou and coworkers employ a Fixman potential to make the model sample the configuration-space probability density characteristic of a flexible molecule in the limit of infinitely stiff bond-stretching force constant.

Table 4.6: Lennard-Jones potential parameters for polyethylene

Model	Group	σ (Å)	ϵ/k_B (K)
SKS	CH_3	3.930	114
	CH_2	3.930	47
PSY	CH_3	4.009	114
	CH_2	4.009	47
HMT	CH_3	3.940	49
	CH_2	3.940	49

Table 4.7: Intramolecular interaction parameters for polyethylene

Potential	SKS	PSY	HMT	Units
bond-stretching				
r_{eq}	1.54	1.54	1.54	Å
k_A/k_B	452 900	∞	∞	K/Å^2
bond-bending				
k_b/k_B	62 500	62 500	57 950	K/rad^2
θ_b	114.0	114.0	112.0	degrees
torsional				
a_0/k_B	1010	873.6	1116	K
a_1/k_B	2019	2265	1462	
a_2/k_B	136.4	384.5	-1578	
a_3/k_B	-3165	-3523	-368	
a_4/k_B			3156	
a_5/k_B			-3788	

4.2.1 Equilibrium properties

Though the primary interests of this study lie in the area of rheology, several equilibrium properties are of interest as well, including the average chain dimension, the self-diffusion coefficient, and rotational relaxation time. The average chain dimension and diffusion coefficient are important because they help gauge the agreement or lack thereof between properties predicted by the potential model and corresponding properties measured by experiment. The rotational relaxation time is important because it aids in analyzing viscosity vs. strain rate data. Finally, all three of the properties can be used in conjunction with results from the Rouse model of unentangled polymer melts to predict the zero-shear viscosity [19].

4.2.1.1 Average chain dimensions

For a linear Gaussian chain, its squared radius of gyration (R_g^2) is related to its squared end-to-end distance (R_{ee}^2) by the relation $R_g^2 = R_{ee}^2/6$. Based on averages accumulated during the course of the EMD run whose average pressure (no long-range corrections) was 23.7 MPa, the measured values for the $C_{100}H_{202}$ system were $R_g^2 = 300.5 \pm 0.2$ Å^2 and $R_{ee}^2 = 1776 \pm 2$ Å^2 which corresponds to $R_g^2 = R_{ee}^2/5.9$. This is closer to Gaussian-chain behavior than has been observed previously for a C_{100} melt as well as melts of shorter alkanes (see Table 4.8). The results from reference [19], reference [78], and this present work are based on the SKS model. The results from Paul *et al.* [46, 103] involve the PSY model. Clearly, as the length of the alkane chain increases, the average chain conformation becomes more like that of a Gaussian chain. Temperature seems to have little effect on this relationship between R_g and

Table 4.8: Conformational properties of various alkane chains

Molecule	T (K)	R_{ee}^2/R_g^2	C_N
$C_{24}H_{50}$ ‡	405	8.1	6.7
$C_{24}H_{50}$ ▽	448	8.0	6.5
$C_{44}H_{90}$ △	450	7.3	7.1
$C_{44}H_{90}$ ▽	448	7.3	7.4
$C_{66}H_{134}$ ▽	448	7.0	8.0
$C_{100}H_{202}$ ⊕	450	6.5	7.2
$C_{100}H_{202}$ ⊕	509	6.5	7.2
$C_{100}H_{202}$ †	448	5.9	7.6
Gaussian Chain	-	6.0	-
$C_\infty H_\infty$ •	413	-	7.8

† the present work; ‡ [78]; ▽ [19]; ⊕ [103]; △ [46]; • [162].

R_{ee}. For $C_{44}H_{90}$, the relationship is same for the two models. However, for $C_{100}H_{202}$ the two models are no longer in agreement.

The $C_{100}H_{202}$ simulation using SKS yields a value of $R_g^2/M = 0.21$ Å$^2/Da$, where M is the molecular weight, in excellent agreement with experimental values for higher M polyethylene (0.23 and 0.21 for M = 32,000 and M = 50,000 respectively [163]). However, Mondello *et al.* point out that, for SKS, extrapolation to $M \Rightarrow \infty$ yields $R_g^2/M = 0.28$ [19]. In Table 4.8 values of the characteristic ratio

$$C_N = \langle \frac{R_{ee}^2}{(N-1)l^2} \rangle \tag{4.5}$$

for various alkanes are also given, where N is number of monomers and l is the carbon-carbon bond length. The experimental value for high molecular weight polyethylene as obtained from small angle neutron scattering (SANS) is $C_\infty = 7.8 \pm 0.4$ at 413 K [162], in excellent agreement with the $C_{100}H_{202}$ simulation results described here. However, though the simulated system appears to behave much like systems of high molecular weight chains, at least conformationally, it may in fact be in less agreement with what would be expected for $C_{100}H_{202}$ itself; Paul *et al.* [103] used RIS techniques to correct the SANS result for chain length and extrapolated to 509 K to estimate a characteristic ratio of $C_{100} = 6.7 \pm 0.4$.

4.2.1.2 Translational diffusion

The self-diffusion coefficient of the $C_{100}H_{202}$ chains is estimated from the EMD simulation in terms of the limiting slope of the mean squared displacement (MSD) of the chain centers of mass as a function of time based on the Einstein relation

$$2tD = \frac{1}{3}\langle |r_i(t) - r_i(0)|^2 \rangle \tag{4.6}$$

where D is the self-diffusion coefficient and r_i is the position of the center of mass of molecule i. The notation $\langle ... \rangle$ is indicative of the fact that the MSD was averaged over the 200 molecules in the system as well as 404 different time origins and corresponding initial positions $r_i(0)$, one separated from the next by 4.7 ps. In Figure 4.17 MSD in units of Å^2 is plotted vs. time in ns. The plot covers 3.76 ns, during which time a chain diffuses an average of approximately 21.3 Å ($1.2 \times \langle R_g \rangle$). This would have to be considered near the lower limit of what is acceptable in terms of the distance diffused during the diffusion coefficient calculation. The dashed line is the simulation data, and the solid line is a fit to the data. The diffusion coefficient is estimated to be 1.85×10^{-6} cm^2/s, approximately twice the experimental value as estimated from the correlation $D = 1.65/\bar{M}_W^{1.98}$ cm^2/s based on experimental measurements [61]. In contrast, based on an EMD simulation containing 40 C_{100} chains at 509 K, Paul, Smith, and Yoon [103] predicted a diffusion coefficient within 4% of their estimate of the experimental value (obtained by using the Rouse prediction to correct for the molecular weight difference and correcting for the temperature dependence of the segmental friction). The good performance of the PSY model has also been confirmed by neutron spin echo data [30]. Harmandaris *et al.* [31], based on EMD simulations of a polydisperse melt involving 10 or 20 chains using the HMT model, reported a diffusion coefficient of C_{90} in excellent agreement with experiment. If the C_{90} experimental data is adjusted for the molecular weight difference using the Rouse model, the estimated experimental value for C_{100} at 448 K would be 1.26×10^{-6} cm^2/s. This would suggest that the SKS does not perform quite as poorly for D of C_{100} as reported above. However, it still represents an overprediction by nearly 50%, consistent with its performance for shorter molecules [19].

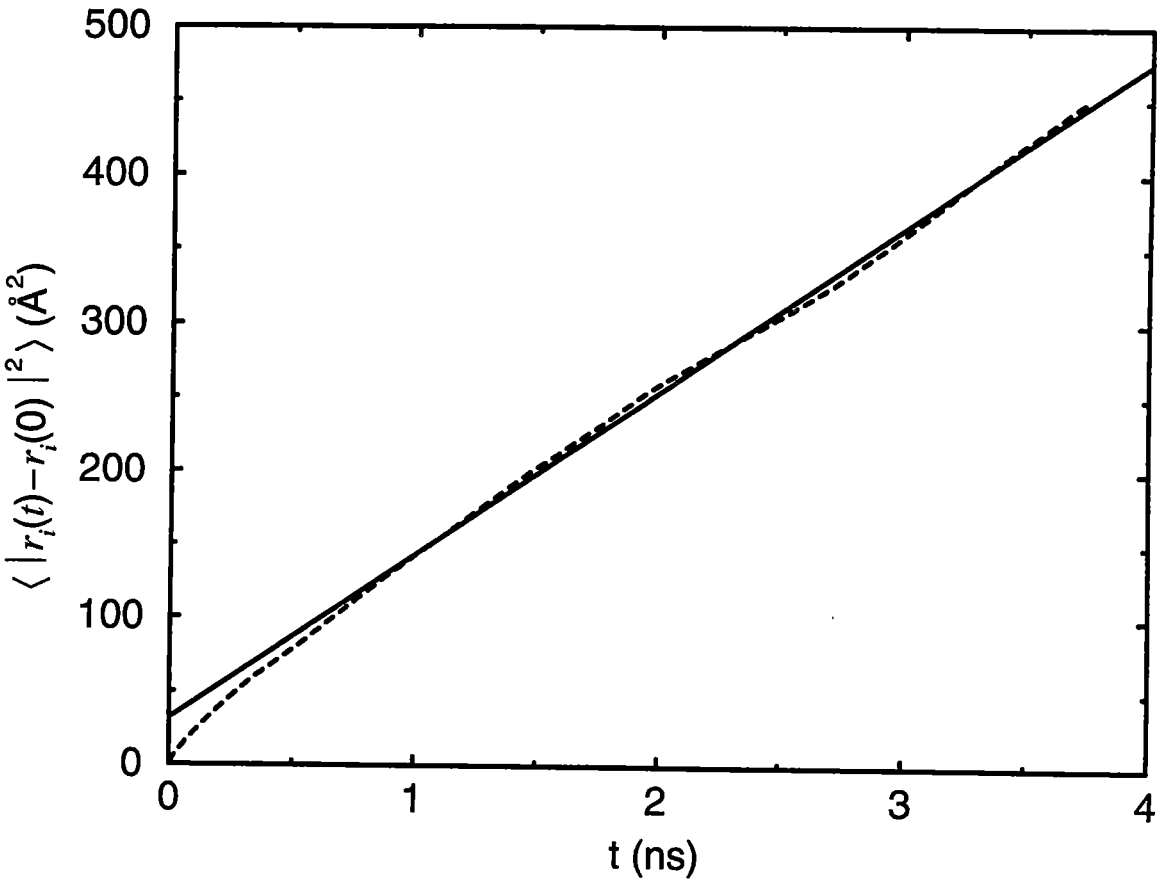

Figure 4.17: Average mean squared displacement of the centers of mass of the $C_{100}H_{202}$ chains vs. time at 448 K and ρ=0.75 g/mL. The dashed line is the simulation data, and the solid line is a fit to the data. The self-diffusion coefficient from the limiting slope is $D = 1.85 \times 10^{-6}$ cm^2/s.

4.2.1.3 Rotational diffusion

The global rotational motion of the molecules is characterized by the orientational relaxation of the longest principal axis (e_1) of each molecule's ellipsoid of inertia. In Figure 4.18 are plotted the first- and second-order angular correlation functions. In the figure, the decay of the functions is presented over a time period of 2.39 ns averaged over the 200 molecules and 500 different time origins and corresponding initial orientations $e_1(0)$, one separated from the next by 0.47 ps. The dashed line is the simulation data, and the solid line is a fit to the data. Ignoring the short-time behavior, the functions exhibit exponential decay with characteristic relaxation times of $\tau_1 = 3.3$ ns and $\tau_2 = 1.7$ ns. For isotropic rotational diffusion, $\tau_1/\tau_2 = 3$ is expected [154, 155]. In this case, $\tau_1/\tau_2 = 1.9$, which is smaller than the values calculated by Mondello and Grest [78] for C_{10} and C_{24} and may indicate that the orientational relaxation of the molecules is spatially constrained [156]. The time allowed for equilibration (7 ns) is approximately twice the rotational relaxation time (τ_1), indicating that the equilibration time was probably sufficient but at the lower end of the range of times that would be considered acceptable. Interestingly, τ_1 for C_{100} is 100 times larger than the value calculated for C_{10} at the same temperature but somewhat higher density ($\rho = 0.766$ g/cm^3) [19], consistent with τ_1 scaling at least approximately as the square of the number of carbons as predicted by the Rouse model [8].

Using results from the Rouse model, expressions for the zero-shear viscosity of the polymer melt can be written in terms of properties that can be measured during an EMD simulation (see Equations 2.28- 2.30). The resulting predictions are $\eta_D(R_{ee}) = \eta_D(R_g) = \eta_\tau = 5.4 \times 10^{-3}$ Pa s. The correlation due to Pearson *et al.* [61] $\eta = 2.1 \times 10^{-5}\bar{M}_W^{1.8} \times 10^{-3}$ Pa s ($M < 5000$) yields a zero-shear viscosity for C_{100} of

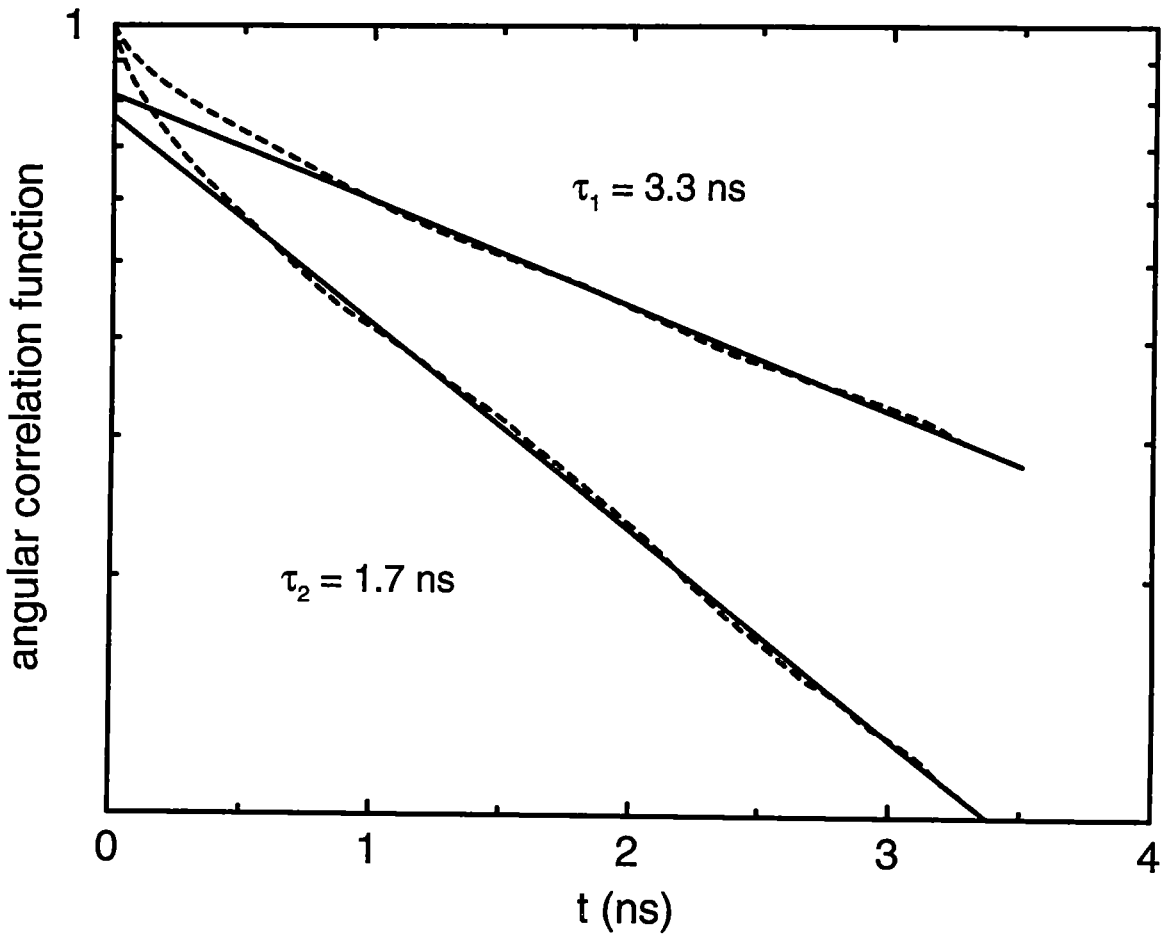

Figure 4.18: First- and second-order angular correlation functions vs. time for $C_{100}H_{202}$ at 448 K and ρ=0.75 g/mL. The dashed line is the simulation data, and the solid line is a fit to the data. The characteristic relaxation time of the first-order function is $\tau_1 = 3.3$ ns. The characteristic relaxation time of the second-order function is $\tau_2 = 1.7$ ns.

$\eta = 9.7 \times 10^{-3}$ Pa s, approximately twice the value predicted by EMD simulation and the Rouse model. This 50% underestimate of the viscosity is a fairly remarkable prediction since the model was fit to completely different physical properties (vapor-liquid equilibria of much shorter chains).

4.2.2 Steady-state shear

4.2.2.1 Viscometric properties

In Figure 4.19, shear viscosity is plotted versus strain rate for $C_{100}H_{202}$. The viscosities are averaged over simulation runs with durations (neglecting the time required to reach steady state) ranging from 0.25 ns at the highest strain rate to 2.8 ns at the lowest strain rate. The horizontal dashed line is the predicted zero-shear viscosity (η_T), mentioned previously, based on the EMD results and the Rouse model. The vertical dot-dashed line is the inverse of the rotational relaxation time. Shear thinning is observed over the entire range of strain rates with a power law exponent of -0.61 at the lower strain rates and -0.35 at the higher. The transition between the two power law regions occurs at approximately $\dot{\gamma} = 1.7 \times 10^{10}$ s^{-1}. Such a drastic change in the power law slope at intermediate strain rates has not been observed previously in NEMD studies of shorter alkane chains. The weaker shear thinning at higher strain rate may be the precursor of a second Newtonian regime. Such an "infinite-shear-rate viscosity" is usually not observed experimentally for concentrated solutions and melts because polymer degradation becomes a problem before sufficiently high shear rates are obtained [49]. Simulations at higher strain rates were not attempted because of concerns about possible artifacts due to the thermostat at higher strain rates (e.g. $\dot{\gamma}^* \geq 4$) [17, 151]. For polymeric liquids, power law exponents are generally reported in the range -0.4 to -0.9 [49]. The Doi-Edwards model for entangled polymers predicts

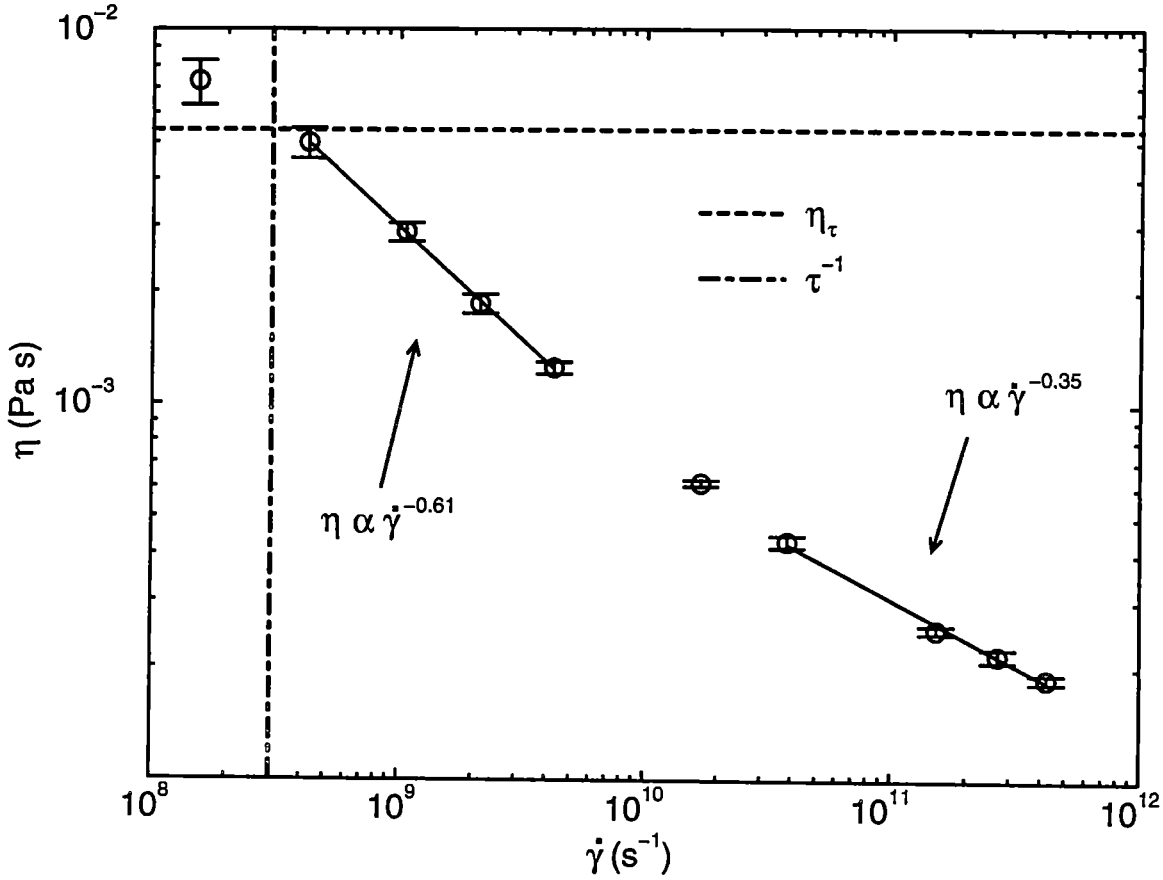

Figure 4.19: Viscosity vs. strain rate for $C_{100}H_{202}$ at 448 K and 0.75 g/mL. The horizontal dashed line is the predicted zero-shear viscosity based on EMD and the Rouse model, and the vertical dot-dashed line is the inverse of the rotational relaxation time. Two power-law regions are observed with a transition between the two occurring at $\dot{\gamma} \approx 1.7 \times 10^{10}$ s^{-1}.

$\eta \propto \dot{\gamma}^{-1.5}$ as $\dot{\gamma} \to \infty$ [34].

No judgement can yet be made regarding the observation (or lack thereof) of the Newtonian plateau for $C_{100}H_{202}$ at strain rates less than the inverse of the rotational relaxation time. The 2.8 ns run at the lowest strain rate, though quite lengthy in terms of the required computational resources, is of insufficient length to draw any conclusions. Typically, runs of up to an order of magnitude longer are required to achieve good estimates of the viscosity at such low strain rates. The error bar, estimated from the scatter in the block averages during the course of the simulation, is likely to be an underestimate of the true uncertainty in the simulation for such a relatively short run at such a low strain rate. Therefore, the result at the lowest strain rate is viewed as preliminary.

The first and second normal stress coefficients are plotted versus shear rate in Figure 4.20, and their ratio is plotted in Figure 4.21. Both coefficients exhibit shear thinning with a power law exponent of approximately -1.4. In comparison, the Doi-Edwards model for entangled polymers predicts $\Psi_1(\dot{\gamma}) \propto \dot{\gamma}^{-2}$ and $\Psi_2(\dot{\gamma}) \propto \dot{\gamma}^{-2.5}$ as $\dot{\gamma} \to \infty$ [34]. At the highest strain rate ($\dot{\gamma} = 4.3 \times 10^{11}$ s^{-1}), $-\Psi_2/\Psi_1 = 2/7$, the value predicted by the Doi-Edwards model (with "independent alignment," an approximation made for mathematical convenience) in the limit of low strain rates [34]. As strain rate decreases from $\dot{\gamma} = 4.3 \times 10^{11}$ s^{-1}, $-\Psi_2/\Psi_1$ also decreases before reaching a value of approximately 0.19, apparently independent of strain rate from 3.83×10^{10} to 4.3×10^{8} s^{-1}. The value of $-\Psi_2/\Psi_1$ is much higher at the lowest strain rate, but that simulation run is too short (and error bar too large) to influence any conclusions. The first normal stress difference ($\sigma_{xx} - \sigma_{yy}$) is plotted versus shear stress in Figure 4.22. Two regimes are evident: $\sigma_{xx} - \sigma_{yy} \propto \sigma_{xy}^{1.6}$ for $\dot{\gamma} \leq 4.3 \times 10^{9}$ s^{-1} and $\sigma_{xx} - \sigma_{yy} \propto \sigma_{xy}^{0.89}$ for $\dot{\gamma} \leq 1.7 \times 10^{10}$ s^{-1}. The value of 1.6 is consistent with the experimental measurements made on various multigrade oils by Williamson *et al.*

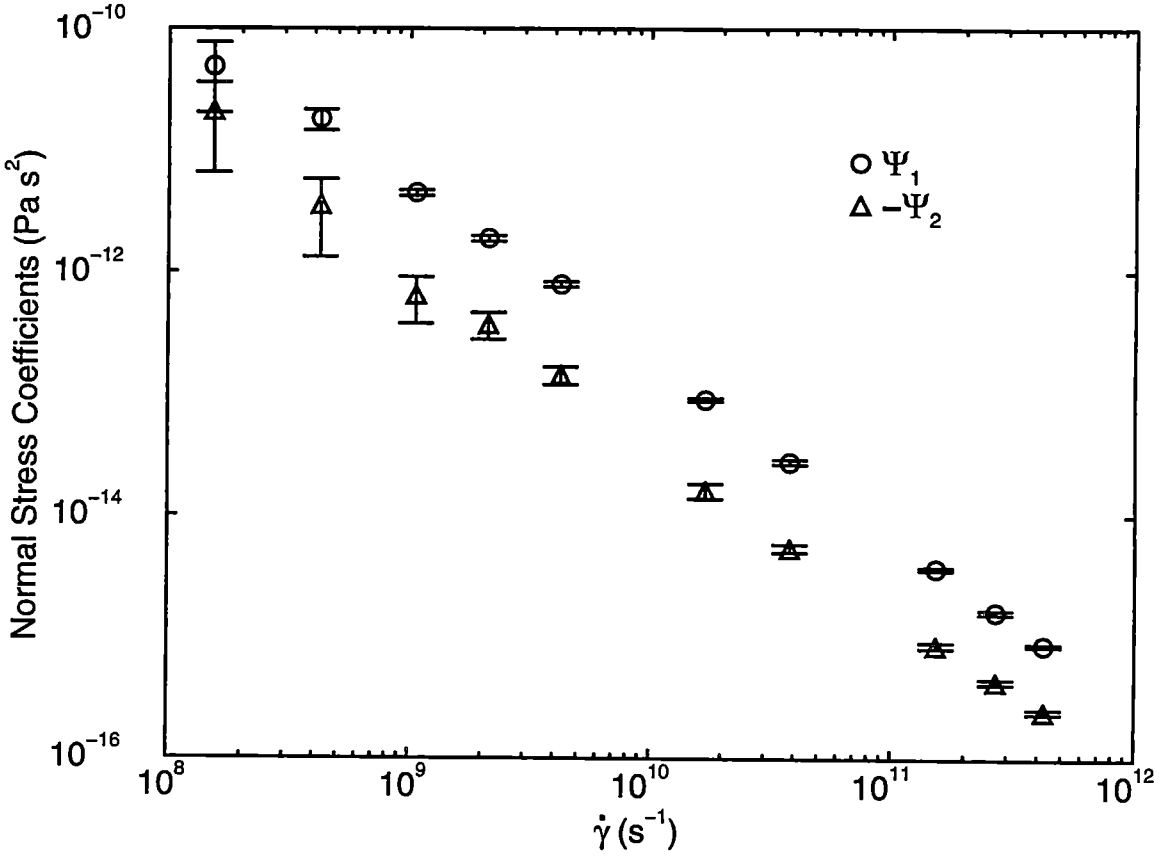

Figure 4.20: First and second normal stress coefficients vs. shear rate for $C_{100}H_{202}$ at 448 K and 0.75 g/mL.

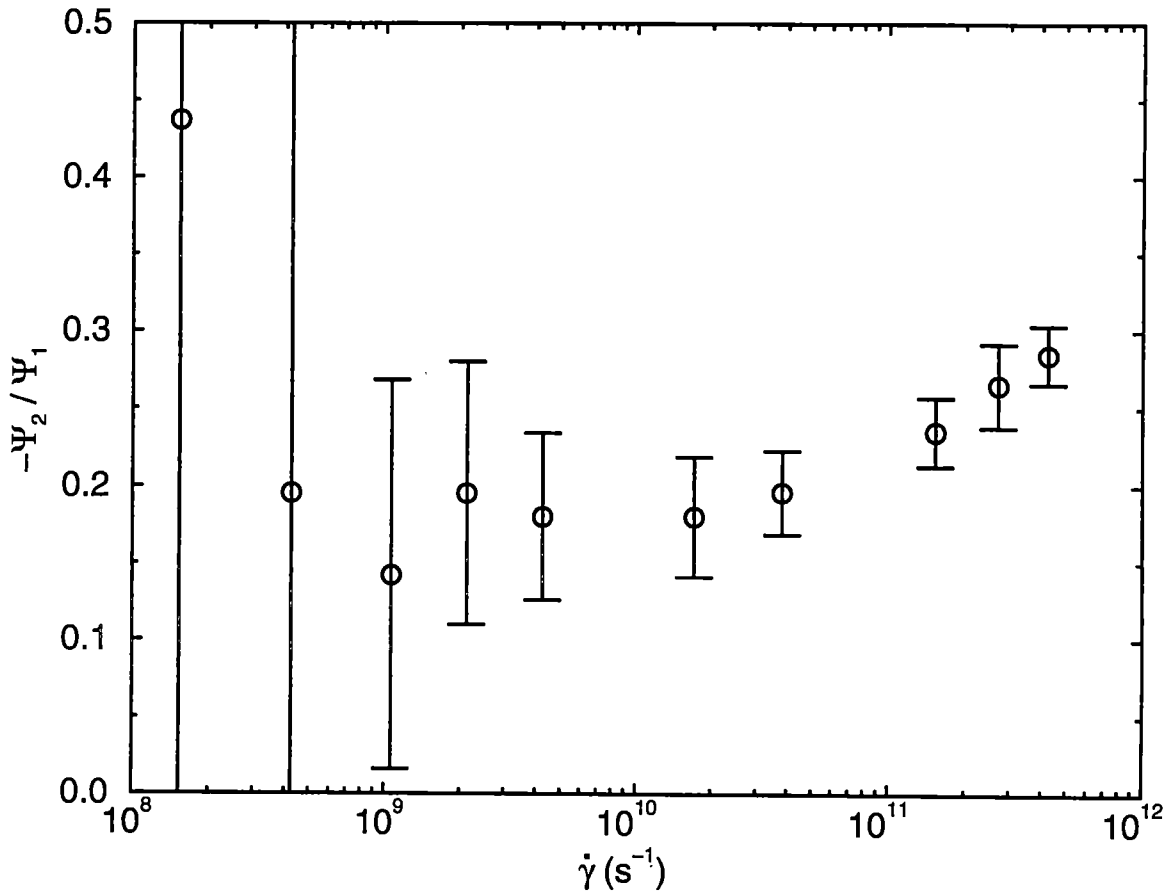

Figure 4.21: Ratio of second to first normal stress difference vs. shear rate for $C_{100}H_{202}$ at 448 K and 0.75 g/mL.

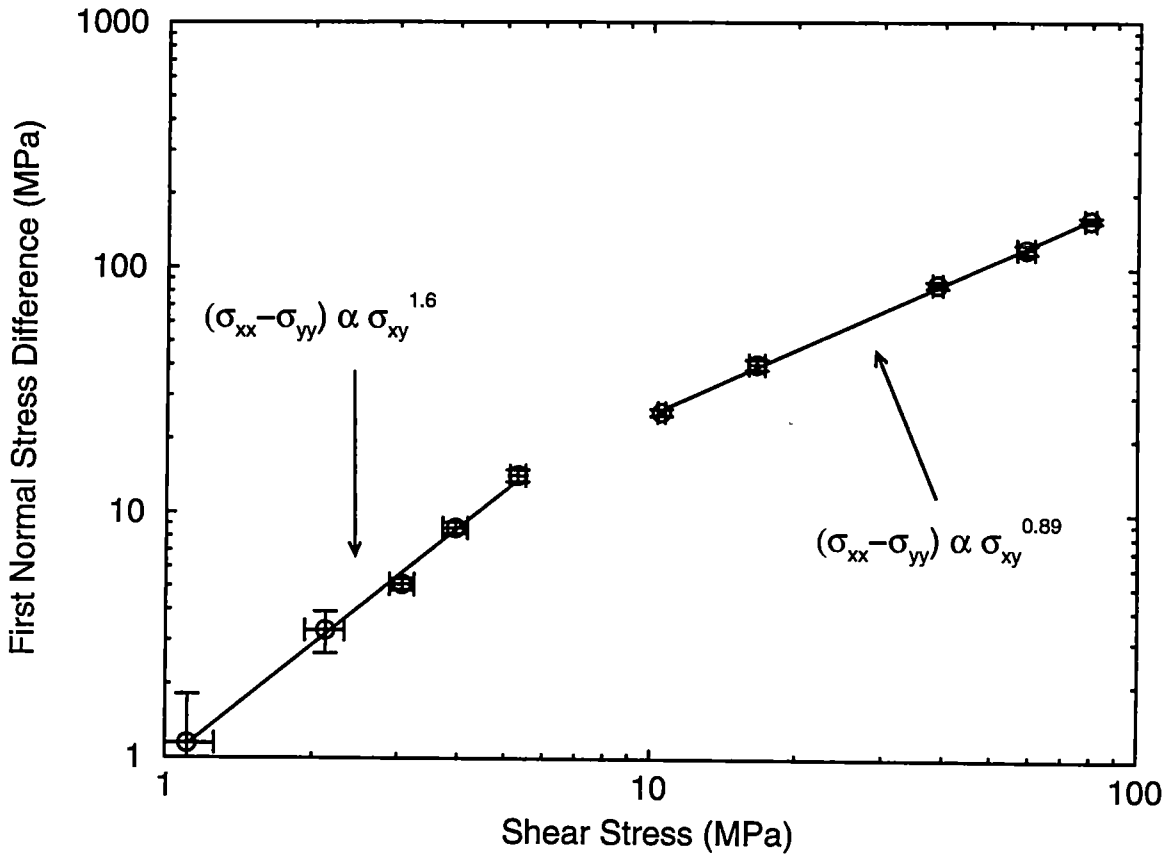

Figure 4.22: First normal stress difference vs. shear stress for $C_{100}H_{202}$ at 448 K and 0.75 g/mL.

[164].

4.2.2.2 Average chain dimensions and shear-induced alignment

Molecular configurations and alignment for $C_{100}H_{202}$ show significant dependence on strain-rate at the shear rates covered in this study. The average squared radius of gyration is plotted versus strain rate in Figure 4.23. At the lowest strain rates, R_g^2 approaches its equilibrium value. As strain rate increases, the shear field deforms the chain configurations and elongates the chain molecules. At the highest strain rates, R_g^2 becomes independent of strain rate and takes on a value approximately 1.67 times larger than the equilibrium one.

Though the linear-regime value of the alignment angle is 45°, Figure 4.24 reveals significant shear-induced alignment even at the lowest strain rate. Based on NEMD studies of shorter alkane chains, Cui *et al.* [152] associated the sharp decrease from 45° of the alignment angle with the transition from Newtonian to shear-thinning behavior. The departure from 45° even at the lowest strain rate suggests that the system may not have reached steady state or that it may be beyond the Newtonian regime even at this strain rate. At high rates of strain, the alignment angle approaches a limiting value of approximately 3°, almost complete alignment with the flow field. Simulations of *n*-$C_{30}H_{62}$ at 372 K revealed a limiting value of 6.8°, as shown in Section 4.1. Indeed, the high shear rate limit of the alignment angle tends to decrease with increasing chain backbone length for linear and branched alkanes [152].

4.2.2.3 Hydrostatic pressure and potential energy

In Figure 4.25 the hydrostatic pressure (no long-range corrections) is plotted versus strain rate. At low strain rates, the pressure approaches the equilibrium value. At

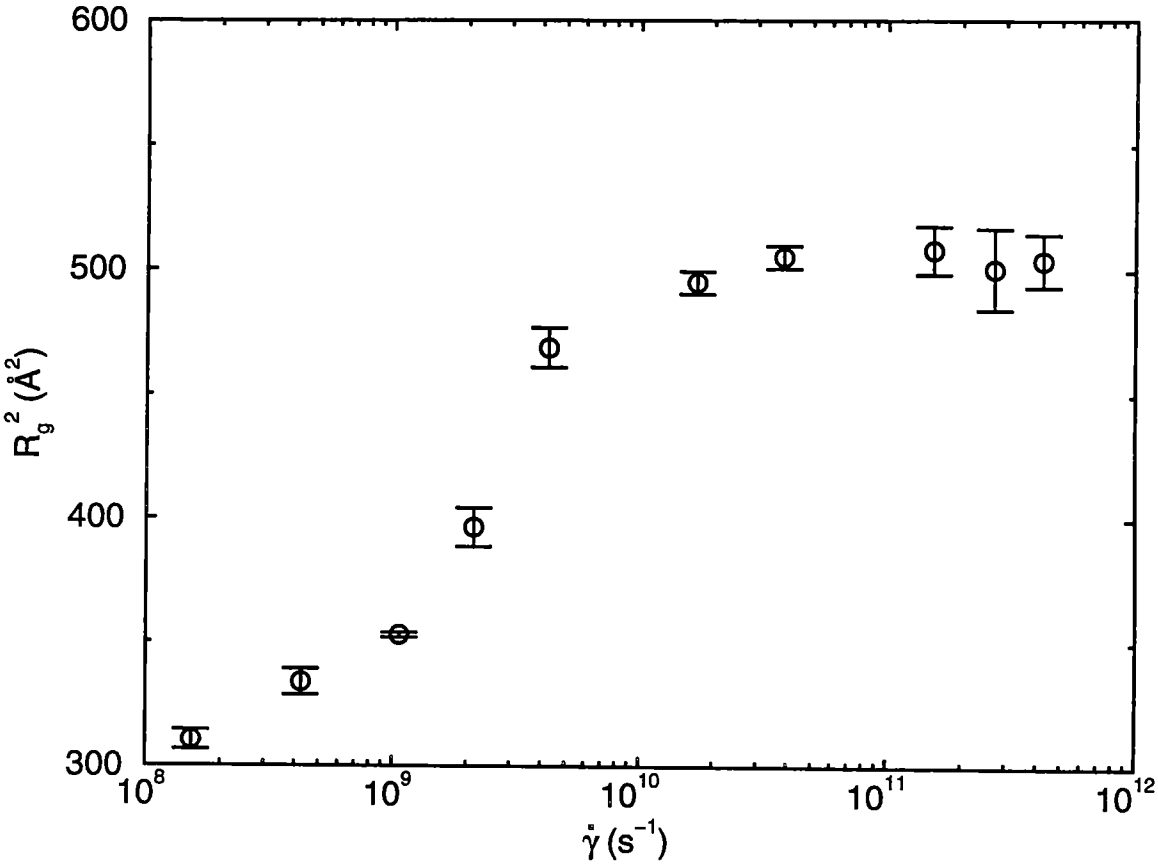

Figure 4.23: Squared radius of gyration vs. strain rate for $C_{100}H_{202}$ at 448 K and 0.75 g/mL.

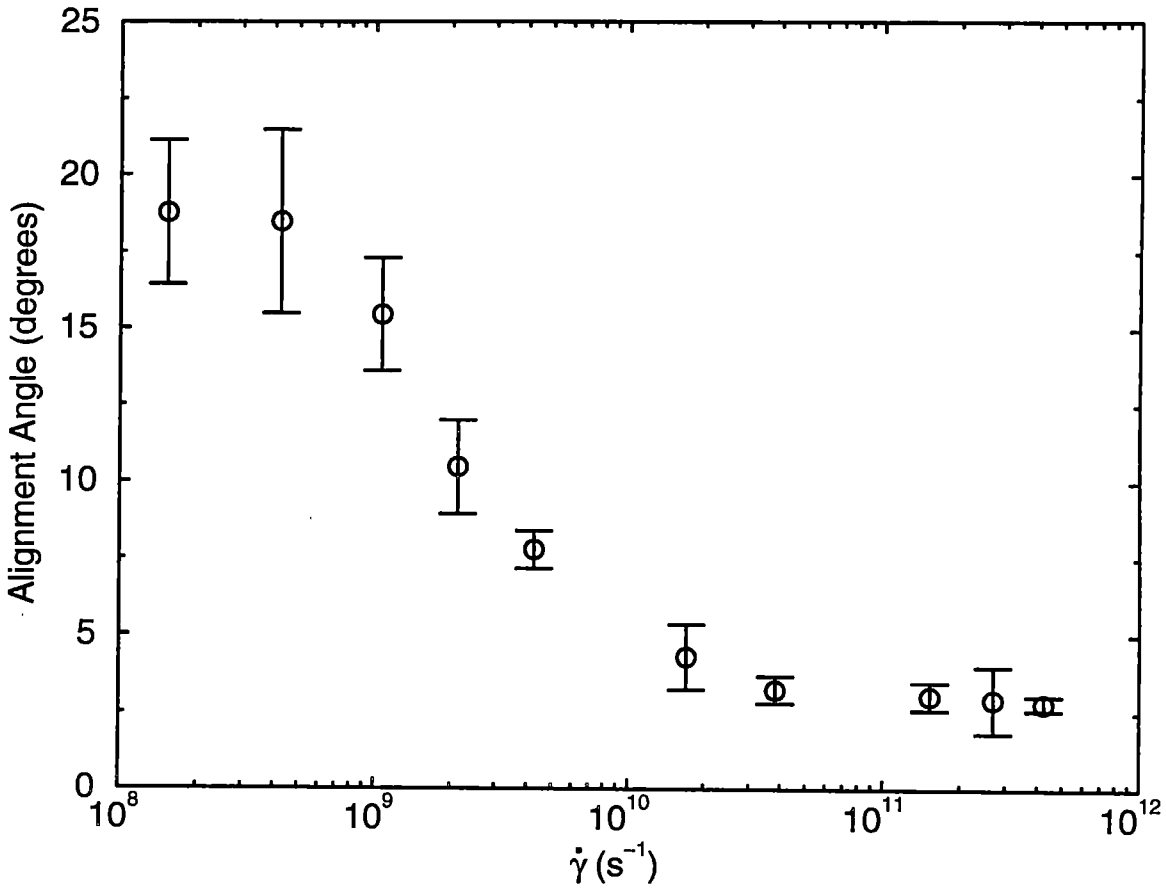

Figure 4.24: Average alignment angle with respect to the flow direction vs. shear rate for $C_{100}H_{202}$ at 448 K and 0.75 g/mL.

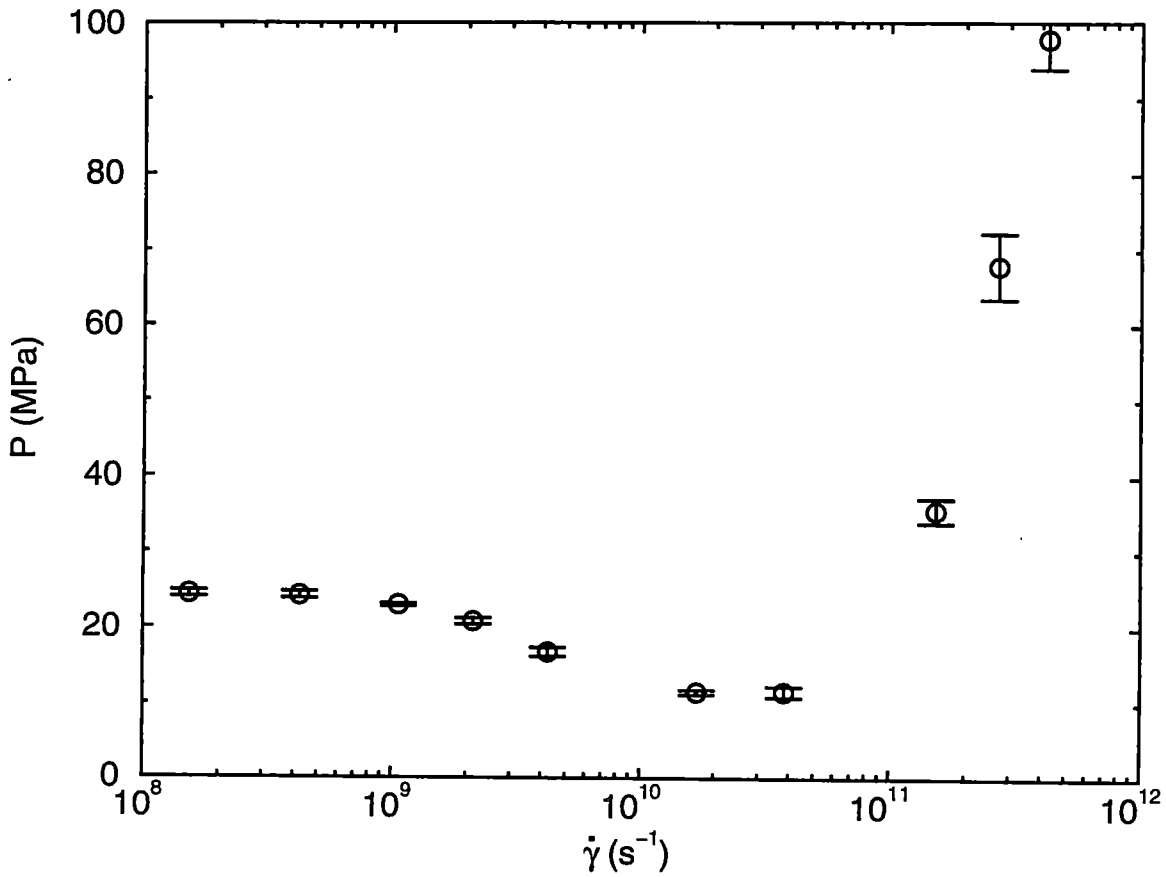

Figure 4.25: Hydrostatic pressure vs. shear rate for $C_{100}H_{202}$ at 448 K and 0.75 g/mL.

high strain rates, shear dilatancy is observed with $P \propto \dot{\gamma}^{0.9}$. In the range 1.7×10^{10} $s^{-1} < \dot{\gamma} < 3.8 \times 10^{10}$ s^{-1}, a minimum in hydrostatic pressure is observed. This pressure minimum has also been observed in simulations of n-$C_{28}H_{58}$ [21] and n-$C_{30}H_{62}$ (as reported in Section 4.1), but not for branched alkanes. The intermolecular Lennard-Jones potential energy also exhibits a minimum at $\dot{\gamma} \approx 3.8 \times 10^{10}$ s^{-1} (see Figure 4.26), as does the torsional potential energy. These observations can be understood in terms of two competing phenomena: the ordering induced by the shear field (tending to lower the energy) and the effect of the high rates of shear that cause more frequent and stronger collisions and keep chains out of the minimum energy states. The former effect dominates at lower strain rates and the latter at higher strain rates, leading to the occurrence of minima in the pressure and energy as a function of strain rate. In fact, Figures 4.19, 4.21, 4.22, 4.23, 4.24, 4.25, and 4.26 all show transitional behavior occurring in the range 1.7×10^{10} $s^{-1} < \dot{\gamma} < 3.8 \times 10^{10}$ s^{-1}. This is where the viscosity's power law exponent changes from -0.61 to -0.35 (Figure 4.19), where the ratio $-\Psi_2/\Psi_1$ becomes $\dot{\gamma}$-dependent with increasing $\dot{\gamma}$ (Figure 4.21), where the power law exponent for the dependence on the shear stress of the first normal stress difference changes from 1.6 to 0.89 (Figure 4.22), where R_g^2 and the alignment angle reach their high-$\dot{\gamma}$ limits (Figures 4.23 and 4.24), and where the pressure and intermolecular Lennard-Jones potential energy exhibit minima (Figures 4.25 and 4.26). The range of strain rates at which these transitions occur may simply be related to the attainment of the maximum shear-induced alignment. Alternatively, it may be associated with the shear rate exceeding the timescale of local chain dynamics (such as the rates of torsional transitions, correlated torsional transitions, or bond vector autocorrelation) which would be expected to occur roughly in the range 10^{-9} to 10^{-11} s^{-1} [47, 99, 100, 103].

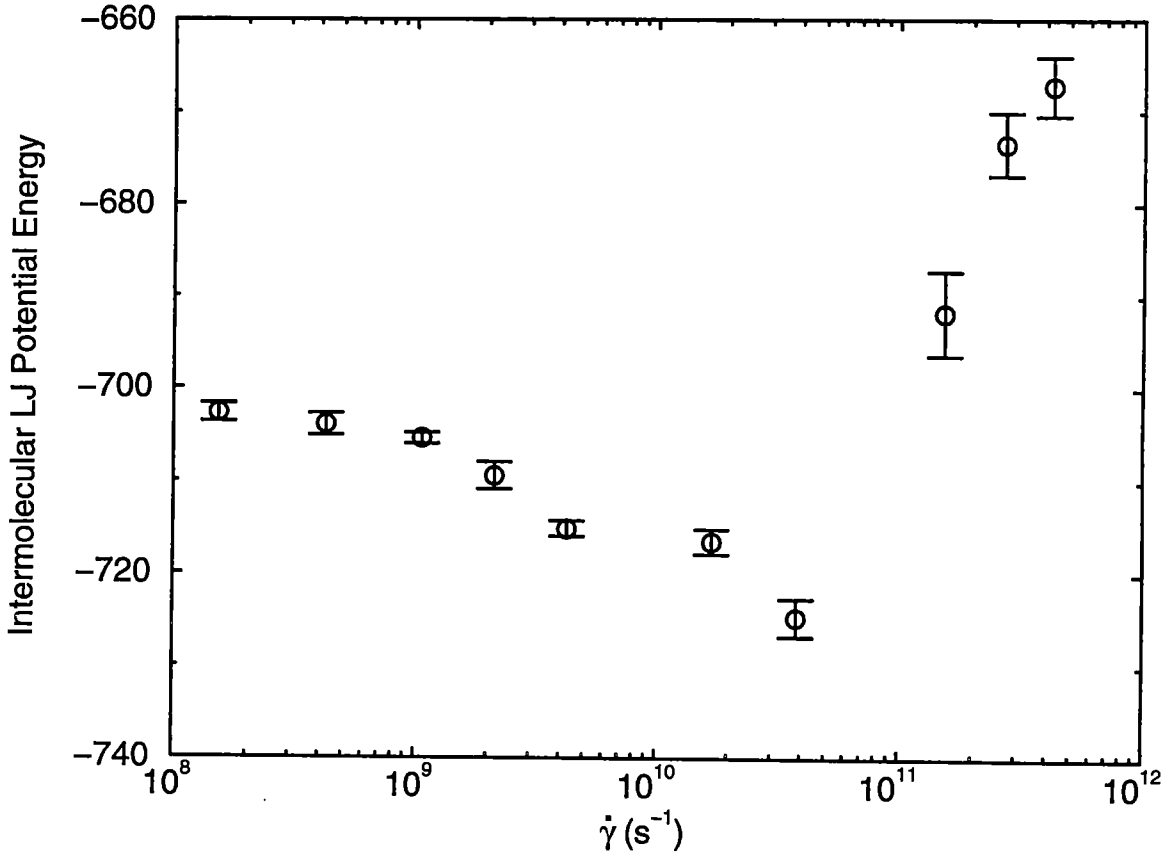

Figure 4.26: Intermolecular Lennard-Jones potential energy per molecule (reduced units) vs. shear rate for $C_{100}H_{202}$ at 448 K and 0.75 g/mL.

4.2.2.4 Shear-enhanced self-diffusion

Prompted by results described in Subsection 4.2.3, the steady-state shear-enhanced self-diffusion of the model polyethylene melt has been characterized using the Cummings-Wang formalism [165] for measuring self-diffusion in a Couette strain field, the basic details of which were described in the Appendix. In practical terms, calculation of the self-diffusion coefficients in a Couette strain field via the Einstein relations only adds one additional equation of motion (for q_x, the unconvected position in the flow direction) which must be integrated. A fourth order predictor-corrector was employed to integrate the equation for q_x, effectively using the multiple timestep algorithm employed to integrate the SLLOD equations as a "black box" to provide the peculiar momenta necessary to integrate the equation of motion for q_x. Although in retrospect method 2 seems preferable for applying the Cummings-Wang formalism to chain molecules, the initial calculations in this study were performed using method 1 (see the Appendix for definitions of methods 1 and 2). Later, tests were performed at two representative states to confirm that the results obtained were independent of the choice of method 1 or 2 within statistical error. In particular, the diagonal elements of the self-diffusion tensor for n-$C_{100}H_{202}$ in the Couette shear field were calculated. In Figure 4.27, the MSDs at $\dot{\gamma} = 1.53 \times 10^{11}$ s^{-1} are plotted. Averages were taken over the 400 molecules in the simulation and multiple time origins, each separated from the next by 2.35 ps. From the long-time limit of these curves, the diffusion coefficients are calculated using the Einstein relations. The behavior seen in Figure 4.27 is typical of that observed for $\dot{\gamma} > 4.25 \times 10^9$ s^{-1}: $D_{xx} \gg D_{zz} > D_{yy}$. Over this range of $\dot{\gamma}$, $D_{xx} \propto \dot{\gamma}$. At $\dot{\gamma} = 4.25 \times 10^9$ s^{-1}, $D_{zz} \approx D_{yy} \approx D$ (where D is the equilibrium self-diffusion coefficient). For smaller strain rates, the simulations were not run long enough to generate MSDs in the y and z directions of sufficient magnitude to have

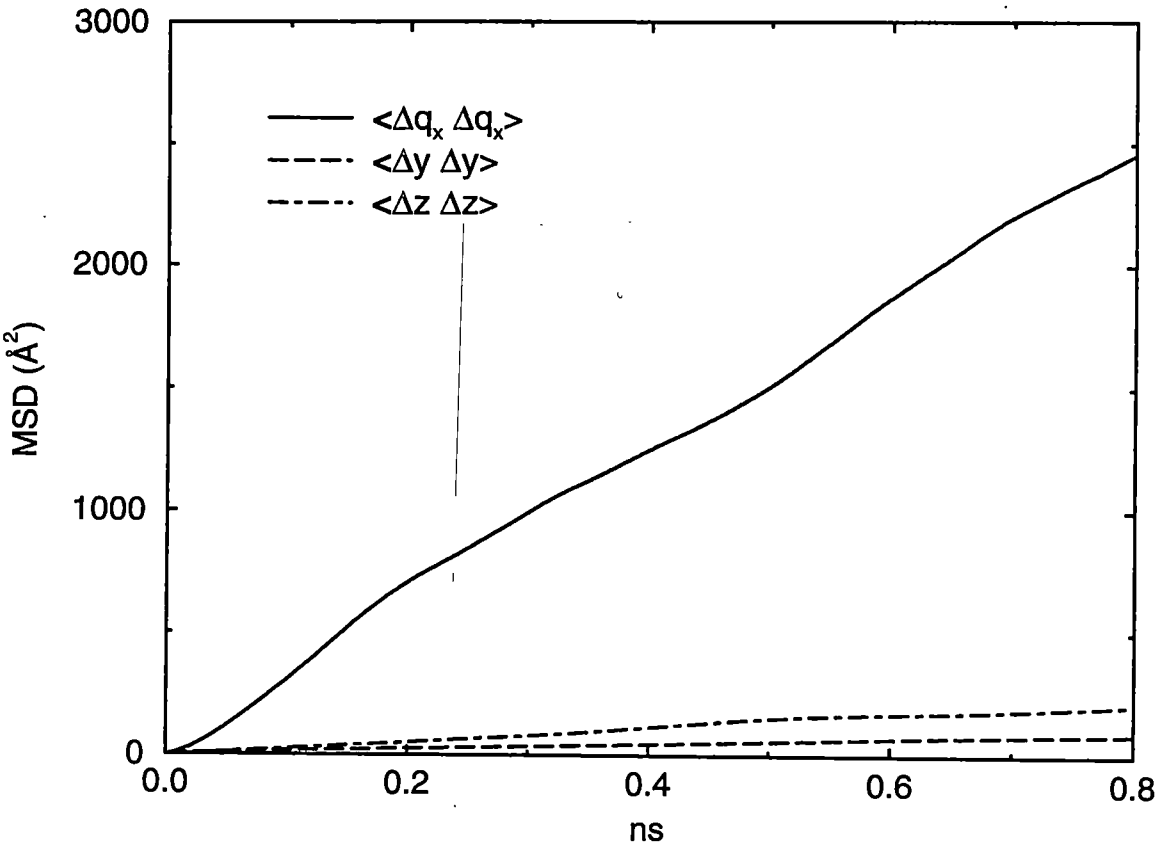

Figure 4.27: Mean squared displacements of q_x, y, and z vs. time for $C_{100}H_{202}$ at $\dot{\gamma} = 1.53 \times 10^{11}$ s^{-1}, 448 K and 0.75 g/mL.

confidence in the calculated values D_{yy} and D_{zz} (though $D_{yy} = 1.77$ and $D_{zz} = 1.70$ calculated at $\dot{\gamma} = 1.06 \times 10^9$ are certainly in agreement with the equilibrium value $D = 1.8$). The calculated diffusion coefficients are compiled in Table 4.9 and plotted in Figure 4.28. At the highest strain rate, D_{xx} is an order of magnitude larger than D_{zz} and two orders of magnitude larger than D_{yy} and D. This shear-enhancement of diffusion for $C_{100}H_{202}$ is much larger than the factor of 2 enhancement observed previously for the Lennard-Jones fluid at its triple point [165]. In addition, for the Lennard-Jones system, the observed trend was $D_{xx} > D_{yy} > D_{zz}$ with all three of similar magnitude. At the lowest strain rate at which diffusion was studied for $C_{100}H_{202}$, D_{xx} was still approximately 2.5 times larger than D. The values of D_{xx} in Table 4.9 were calculated using method 1 (as described in the section on simulation methodology). Also plotted in Figure 4.28 are calculations at two representative

Table 4.9: Diffusion coefficients of $C_{100}H_{202}$ under planar Couette flow at 448 K and 0.75 g/mL

Strain Rate (s^{-1})	Reduced Strain Rate †	Number of Time Origins	D_{xx} ‡	D_{yy} ‡	D_{zz} ‡
1.06×10^9	0.0025	100	4.94	-	-
2.13×10^9	0.005	163	5.27	-	-
4.25×10^9	0.01	95	9.28	1.48	1.44
3.83×10^{10}	0.09	185	47.0	2.39	7.18
1.53×10^{11}	0.36	170	151	5.47	13.8
2.72×10^{11}	0.64	25	310	5.67	27.2
4.25×10^{11}	1.00	75	477	6.35	30.6

† $\dot{\gamma}(m\sigma^2/\epsilon)^{1/2}$ ‡ 10^{-6} cm^2/s

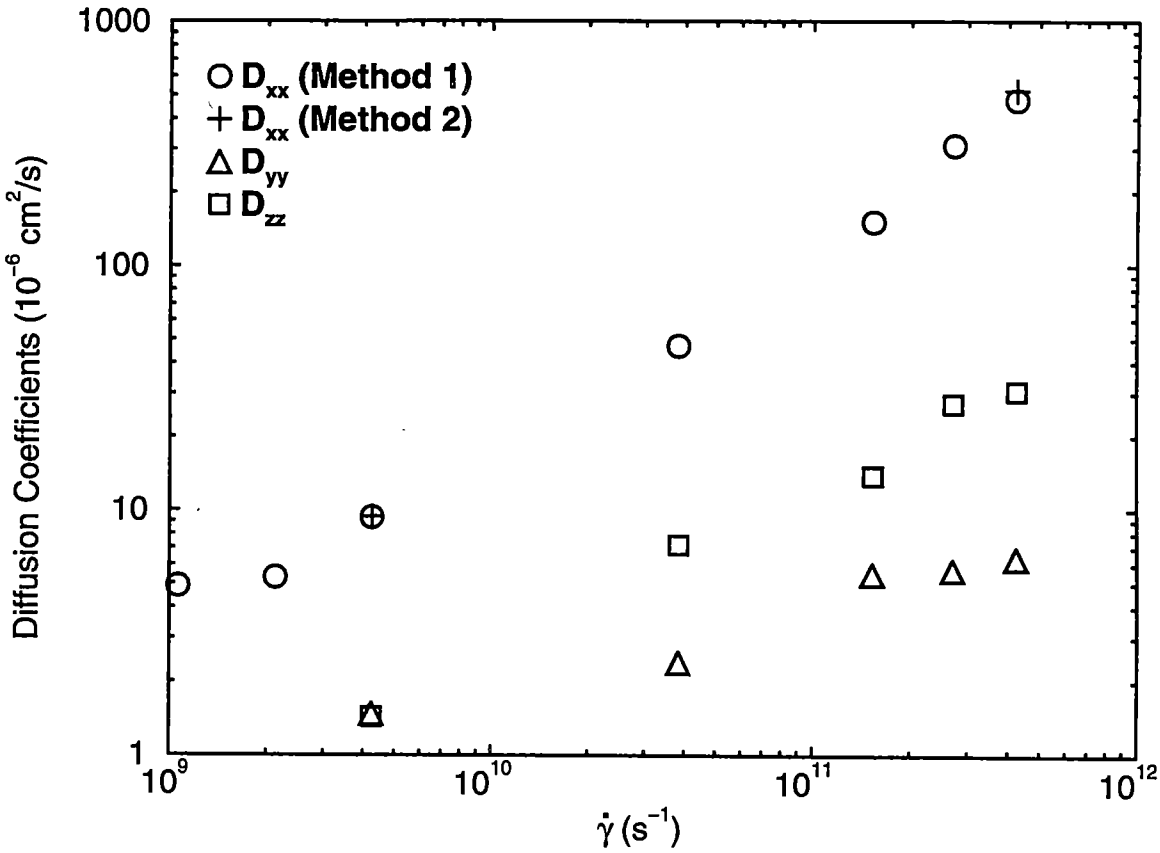

Figure 4.28: Diffusion coefficients vs. shear rate for $C_{100}H_{202}$ at 448 K and 0.75 g/mL. Methods 1 and 2, which are defined in the Appendix, refer to the details of the application of the Cummings-Wang formalism.

strain rates which were performed using method 2, confirming our expectation the resulting diffusion coefficients would be insensitive to the choice of method 1 versus method 2. Though the extremely large magnitude of the shear-enhancement of self-diffusion was initially somewhat surprising, in retrospect, significant enhancement in x-direction should not have been unexpected. Since at high $\dot{\gamma}$ the chains are almost completely aligned with the flow direction (x-direction), the chains move more easily along their own backbones (essentially in the x-direction) than in either the velocity-gradient or neutral directions (though the enhancement in the neutral direction relative to the velocity-gradient direction is not as easily rationalized).

4.2.3 Transient response upon onset of shear

In addition to the steady-state properties discussed in Subsection 4.2.2, the transient response of the model polyethylene melt to constant shear-rate start-up is also of interest. Referred to as "stress growth upon inception of shear flow" in Bird *et al.* [49], the constant shear-rate start-up test is a simple shear flow experiment commonly used in rheological studies. The fluid, assumed to be at rest for times $t < 0$, is subjected to a constant velocity gradient $\dot{\gamma}$ for $t \geq 0$, and the approach of the various growth coefficients ($\eta^+(t,\dot{\gamma})$, $\Psi_1^+(t,\dot{\gamma})$, and $\Psi_2^+(t,\dot{\gamma})$) to their steady-state values is observed. The shear stress growth coefficients for three different high shear rates are plotted in Figure 4.29. These coefficients pass through maxima before reaching steady-state. The system is clearly in the shear-thinning regime since the steady-state viscosity increases with decreasing shear rate. Also, the time required to reach steady-state increases with decreasing strain rate.

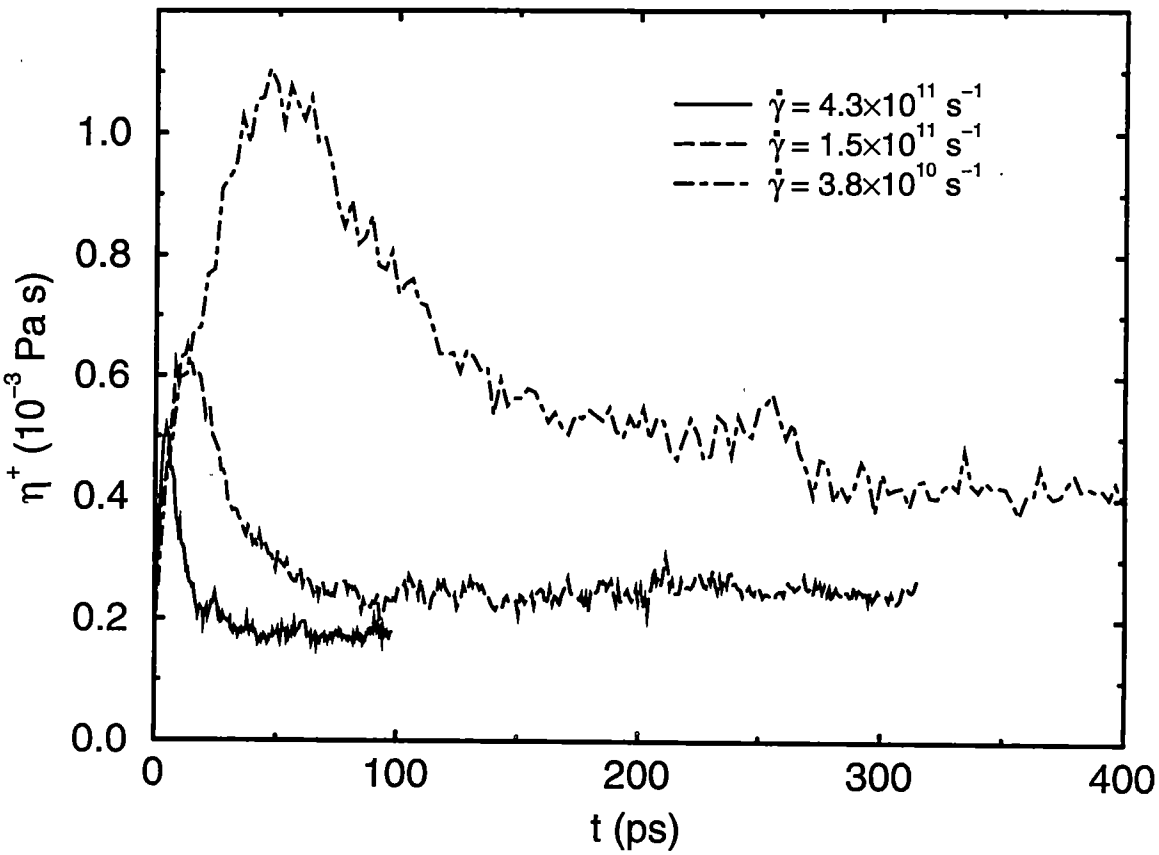

Figure 4.29: Shear stress growth coefficients of the $C_{100}H_{202}$ melt under constant shear-rate start-up at $T = 448$ K and $\rho = 0.75$ g/mL.

4.2.3.1 Stress overshoot: molecular-level origins

In Figures 4.30, 4.31, and 4.32, the shear stress, first normal stress difference, and second normal stress difference growth coefficients at $\dot{\gamma}$=4.3×10^{11} s^{-1} are decomposed into the components arising from the various contributions to the pressure tensor **P** (see Equation 3.9). The contributions include the intramolecular-potential (LJ, bond-stretching, bond-angle-bending, and torsional), intermolecular-potential (LJ), and kinetic contributions and are plotted vs. total strain $\gamma \equiv \int \dot{\gamma} dt = \dot{\gamma} t$. The curves were averaged over 3 independent constant shear-rate start-up simulations. All six contributions to η^+ pass through extrema during their approach to steady state. The kinetic and torsional contributions pass through minima. The bond-stretching, intramolecular-LJ, and intermolecular-LJ contributions all pass through maxima at $\dot{\gamma} t \approx 2$. The bond-angle-bending contribution passes through a minimum followed by a maximum. Clearly, the bond-stretching and intermolecular-LJ contributions dominate the stress overshoot. The former provides confirmation that the stress overshoot is closely related to the stretching of the individual chain-segments under the influence of the flow field. The latter suggests that, as the chains are being straightened-out and aligned, the shearing of molecules past one another causes strong intermolecular "frictional" interactions that also contribute significantly to the transient behavior of the shear stress. Also plotted in the figure is the sum of all the intramolecular contributions (stretching+intraLJ+bending+torsional) to η^+. At small values of total strain, the intramolecular-LJ and bond-angle-bending contributions are of sufficient magnitude to contribute significantly to the stress overshoot and, in conjunction with the bond-stretching term, cause the total intramolecular contribution to the stress overshoot to equal the intermolecular-LJ contribution. At larger values of strain, the intramolecular-LJ and bond-angle-bending contributions become negligible, and the

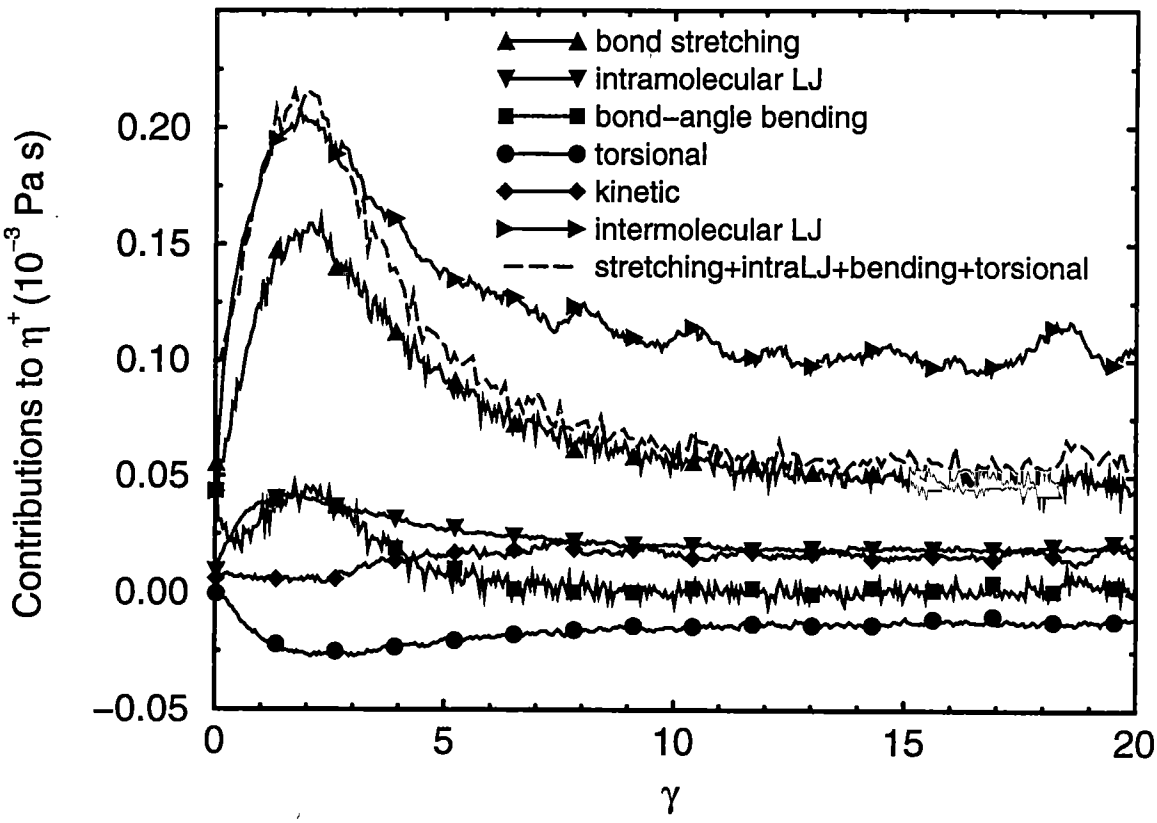

Figure 4.30: Contributions to the shear stress growth coefficient of the $C_{100}H_{202}$ melt under constant shear-rate start-up at $\dot{\gamma} = 4.3 \times 10^{11}$ s^{-1}, $T = 448$ K, and $\rho = 0.75$ g/mL.

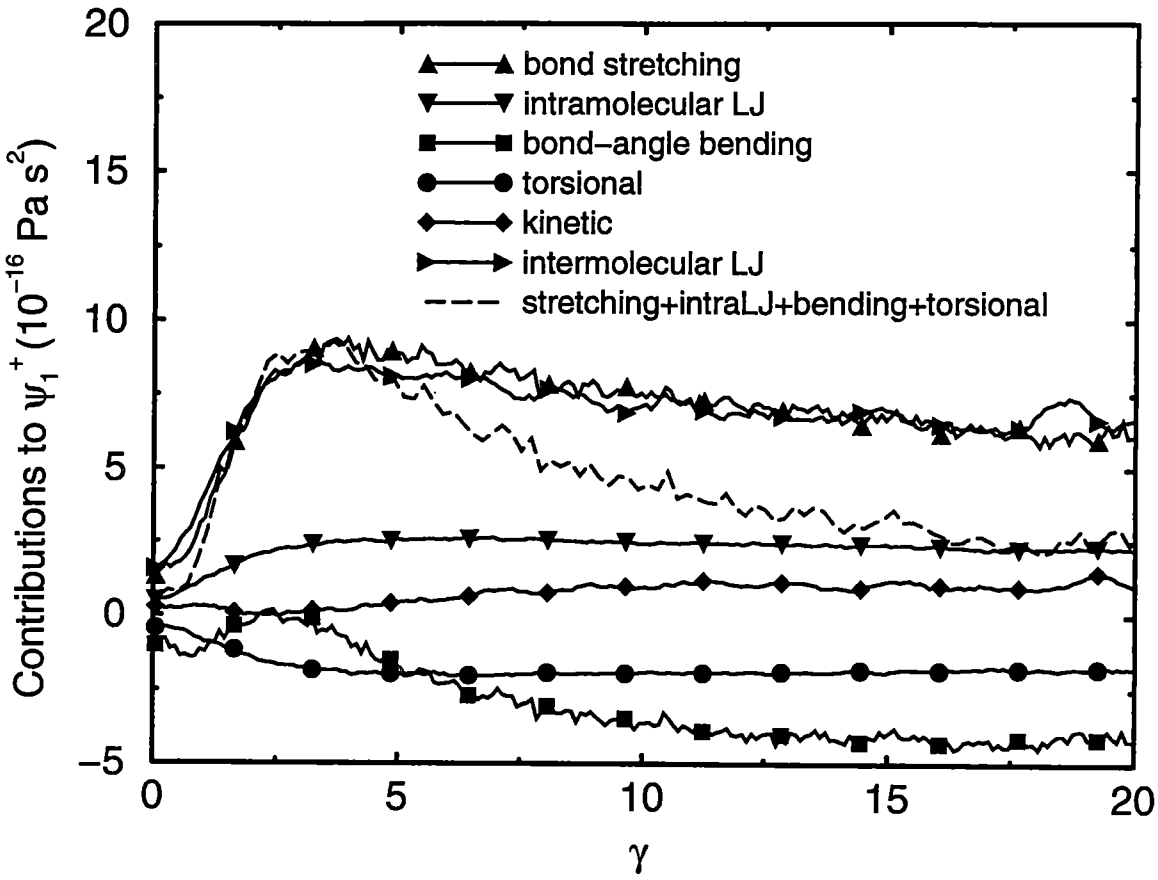

Figure 4.31: Contributions to the first normal stress difference growth coefficient of the $C_{100}H_{202}$ melt under constant shear-rate start-up at $\dot{\gamma} = 4.3 \times 10^{11}$ s^{-1}, $T = 448$ K, and $\rho = 0.75$ g/mL.

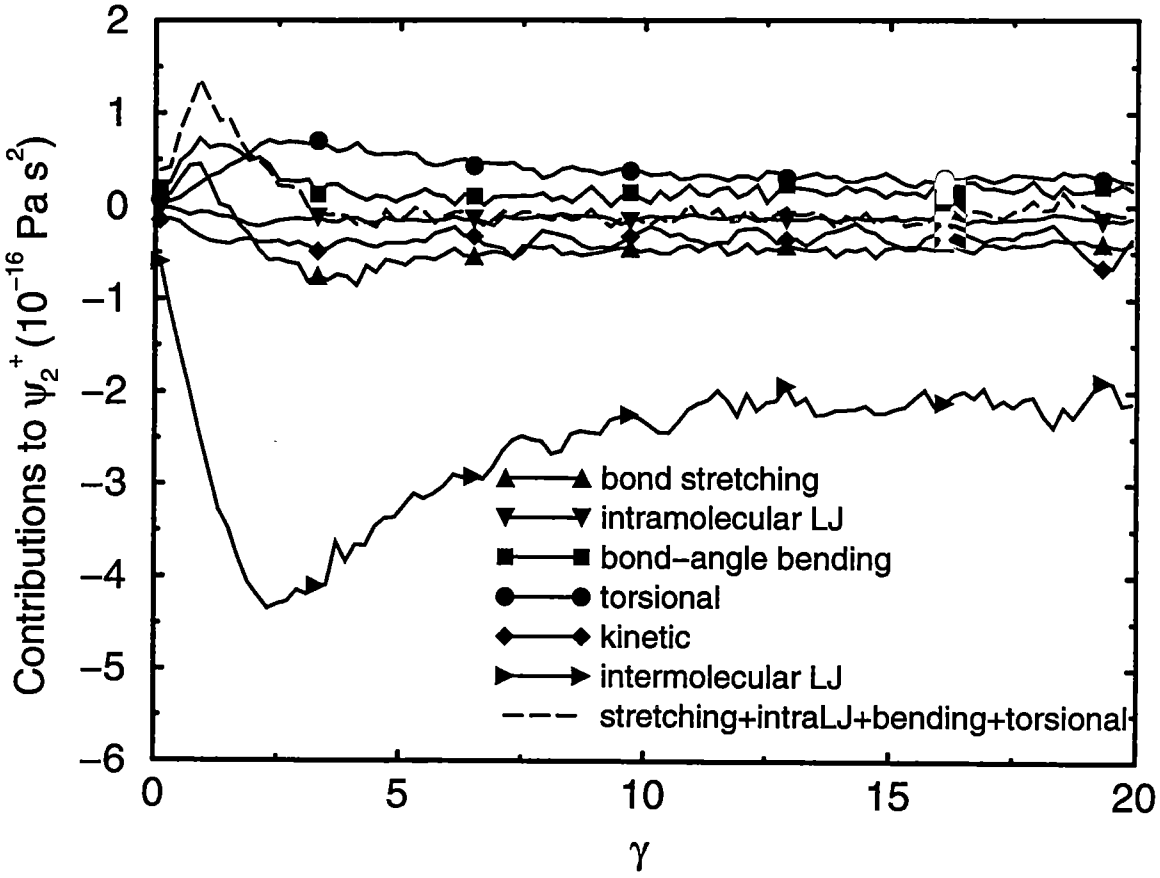

Figure 4.32: Contributions to the second normal stress difference growth coefficient of the $C_{100}H_{202}$ melt under constant shear-rate start-up at $\dot{\gamma} = 4.3 \times 10^{11}$ s^{-1}, $T = 448$ K, and $\rho = 0.75$ g/mL.

intramolecular contribution is dominated by the bond-stretching contribution alone.

As seen in Figure 4.31, the transient response of Ψ_1 is also dominated by bond-stretching and intermolecular-LJ contributions of approximately equal magnitude. The approaches to steady state of the intramolecular-LJ, kinetic, and torsional contributions are essentially monotonic. As it did for η^+, the bond-angle-bending contribution to Ψ_1^+ passes through a minimum followed by a maximum. At small values of total strain, the total intramolecular contribution is almost completely dominated by the bond-stretching term since the kinetic and bond-angle-bending contributions are negligible and the intramolecular-LJ and torsional contributions are of similar magnitude but opposite sign. At higher values of total strain, the bond-angle-bending contribution is more significant and, in combination with the torsional contribution, cancels the bond-bending term so that the total intramolecular contribution is equal to the intramolecular-LJ one. The various contributions to the transient response of Ψ_2 upon onset of shear are seen in Figure 4.32. The second normal stress difference is dominated by the intermolecular-LJ contribution alone. The total intramolecular contribution is negligible except at $\gamma \approx 1$ where it passes through a maximum.

4.2.3.2 Stress overshoot: strain-rate dependence

In Figure 4.33 the shear stress growth coefficient data from Figure 4.29 as well as three additional strain rates are plotted in a somewhat different fashion: shear stress growth coefficient normalized by the steady state viscosity vs. total strain. When plotted in this way, the six curves covering two orders of magnitude in strain rate are collapsed into two curves. In all cases, the peak viscosity occurs at $\gamma \approx 2$, in quantitative agreement with predictions from DE. At $\dot{\gamma} = 4.25 \times 10^{11}$ s^{-1}, $\dot{\gamma} = 2.72 \times 10^{11}$ s^{-1}, $\dot{\gamma} = 1.53 \times 10^{11}$ s^{-1}, and $\dot{\gamma} = 3.83 \times 10^{10}$ s^{-1}, $\eta^+(\gamma = 2)/\eta^+(t \to \infty) \approx 2.5$

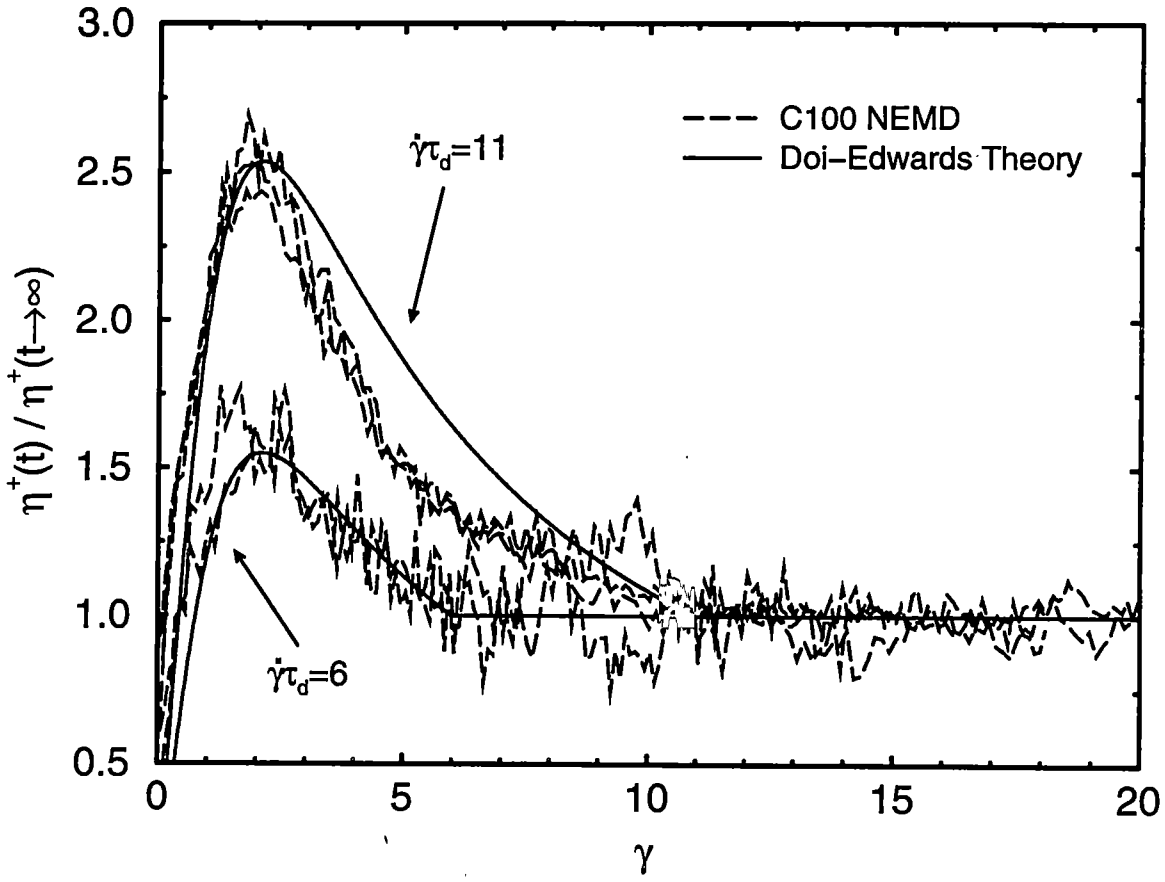

Figure 4.33: Shear stress growth coefficient normalized by the steady-state viscosity plotted vs. total strain ($\gamma \equiv \int \dot{\gamma} dt = \dot{\gamma} t$). The dashed lines are NEMD results for $C_{100}H_{202}$ ($T = 448$ K and $\rho = 0.75$ g/mL), and the solid lines are results from Doi-Edwards theory using the values of $\dot{\gamma}\tau_d$ indicated in the figure. The upper group of NEMD curves includes $\dot{\gamma} = 4.25 \times 10^{11}$ s^{-1}, $\dot{\gamma} = 2.72 \times 10^{11}$ s^{-1}, $\dot{\gamma} = 1.53 \times 10^{11}$ s^{-1}, and $\dot{\gamma} = 3.83 \times 10^{10}$ s^{-1}. The lower group includes $\dot{\gamma} = 4.25 \times 10^{9}$ s^{-1} and $\dot{\gamma} = 2.13 \times 10^{9}$ s^{-1}.

and the shear stress reaches its steady-state value at $\gamma \approx 11$. At $\dot{\gamma} = 4.25 \times 10^9$ s^{-1} and $\dot{\gamma} = 2.13 \times 10^9$ s^{-1}, $\eta^+(\gamma = 2)/\eta^+(t \to \infty) \approx 1.7$ and the shear stress reaches its steady-state value at $\gamma \approx 6$. The agreement between simulation and DE theory for the total strain at the peak shear stress prompted the explicit comparison between the stress overshoot curves of $C_{100}H_{202}$ at high strain rate and DE theory. In the theory, the steady-state viscosity is reached in the amount of time τ_d (the disentanglement or reptation time), so it was necessary to choose two different values of the product $\dot{\gamma}\tau_d$ (as indicated in the figure) in order to reconcile the theoretical predictions with the simulation results. This implies terminal relaxation times (τ_d) of approximately 2.8×10^{-9} s, 1.4×10^{-9} s, 2.9×10^{-10} s, 7.2×10^{-11} s, 4.0×10^{-11} s, and 2.6×10^{-11} s at strain rates $\dot{\gamma} = 2.1 \times 10^9$ s^{-1}, 4.3×10^9 s^{-1}, 3.8×10^{10} s^{-1}, 1.5×10^{11} s^{-1}, 2.7×10^{11} s^{-1}, and 4.3×10^{11} s^{-1} respectively, and that $\tau_d \propto 1/\dot{\gamma}$ over the 2 two ranges of strain rates where the curves are overlapping. Thus, by choosing the strain-rate-dependent τ_d corresponding to the time required to reach steady-state, we are able to achieve quantitative agreement between the $C_{100}H_{202}$ simulations and DE theory for the peak transient viscosity upon onset of shear relative to the steady-state viscosity.

The values of τ_d are much less than the value of τ_d that would usually be used in DE theory [8]. In the theory, τ_d is estimated on the basis of the time taken for a polymer molecule to move through a distance equal to its own length in a tube created by the surrounding polymer molecules, calculated in the absence of shear based on diffusive motion through the tube. As reported in Section 4.2.2, the self-diffusion coefficients for $C_{100}H_{202}$ are markedly enhanced under shear compared to the equilibrium state (up to two orders of magnitude in the flow direction at the highest shear rate studied). In Figure 4.34 the inverse of the relaxation time is plotted vs. strain rate for $C_{100}H_{202}$ as determined from the time for the shear stress growth coefficient to reach steady state and from the strain-rate-dependent D_{xx} using an

arbitrary but physically plausible characteristic distance of 250 Å^2, somewhat smaller than the average equilibrium squared radius of gyration (300 Å^2). As can be seen in the figure, the observed variation of D_{xx} with strain rate is consistent with that of the time required for the viscosity to reach steady state upon onset of shear.

In contrast to the predictions of DE but qualitatively consistent with the behavior predicted by recently developed modifications of DE theory [40, 43], overshoot is observed in Ψ_1 upon onset of shear for $C_{100}H_{202}$. Curves corresponding to four strain rates are plotted in Figure 4.35. Ψ_1^+ reaches a maximum at $\gamma \approx 3.5$ independent of strain rate, and the value of $\Psi_1^+(\gamma \approx 3.5)/\Psi_1^+(t \to \infty)$ is approximately 2 at the three higher strain rates and 1.5 at the lower one. Ψ_2^+ also reaches a maximum (in magnitude) at $\gamma \approx 3.5$, but the noise in the Ψ_2^+ curves increases rapidly as strain rate decreases and, therefore, we do not include here a figure similar to Figure 4.35 for Ψ_2^+.

4.2.3.3 Stress overshoot: chain-length dependence

Also of interest is how the stress overshoot is affected by chain length. This effect is presented in Figure 4.36 in terms of the normalized shear stress growth coefficient vs. total strain for melts of C_{100}, C_{30}, and C_{10}. The state points correspond to the experimental density (interpolated for both C_{100} and C_{30}) at a temperature roughly between 30 and 60 K above each particular system's (experimental) melting point. The C_{100} curve was averaged over 3 independent constant shear-rate start-up simulations, the C_{30} curve averaged over 12, and the C_{10} averaged over 20. Though fairly subtle in the case of decane, stress overshoot is observed in all three systems at this extremely high shear rate. The relative peak viscosity increases with chain length from 1.2 to 1.7 to 2.5. The location of the peak appears to have increased as

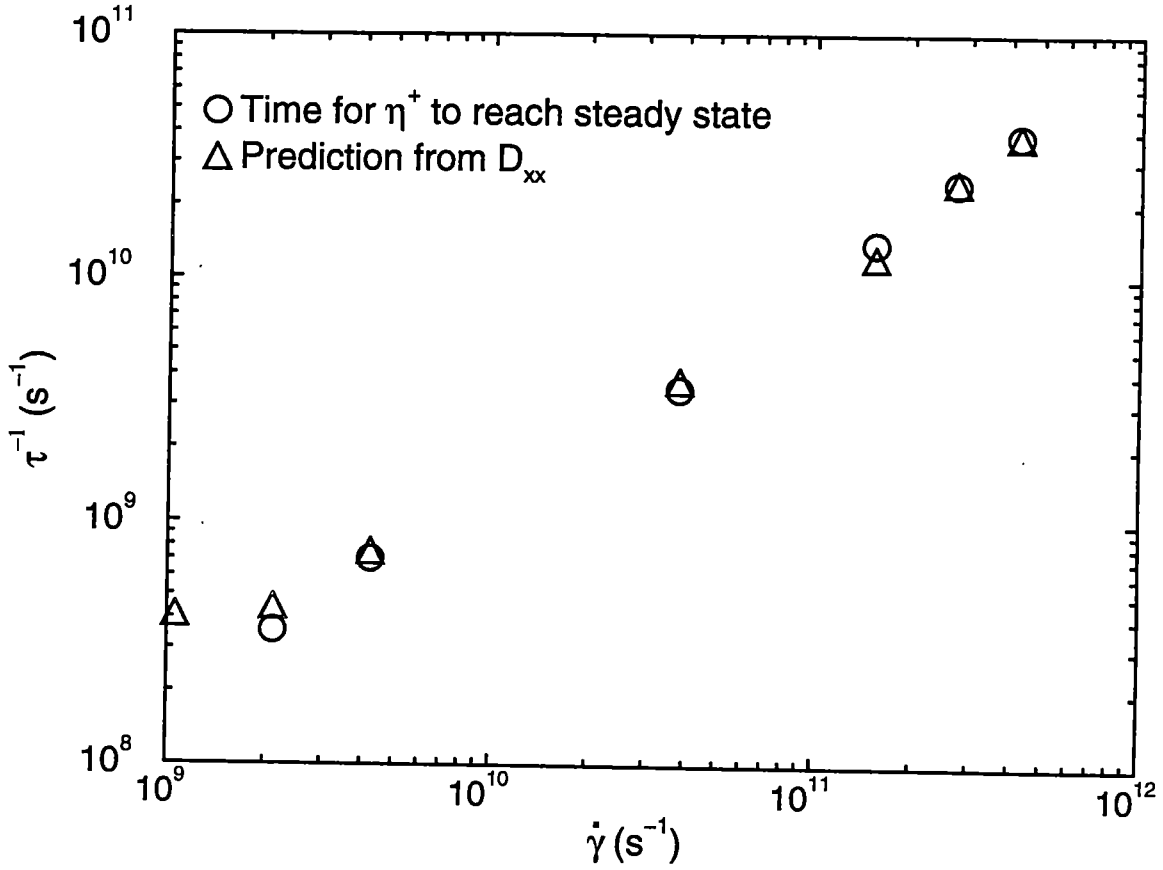

Figure 4.34: Inverse of the relaxation time vs. strain rate for $C_{100}H_{202}$ ($T = 448$ K and $\rho = 0.75$ g/mL) determined from the time for the shear stress growth coefficient to reach steady state (circles) and determined from D_{xx} using a characteristic distance of 250 Å^2 (triangles).

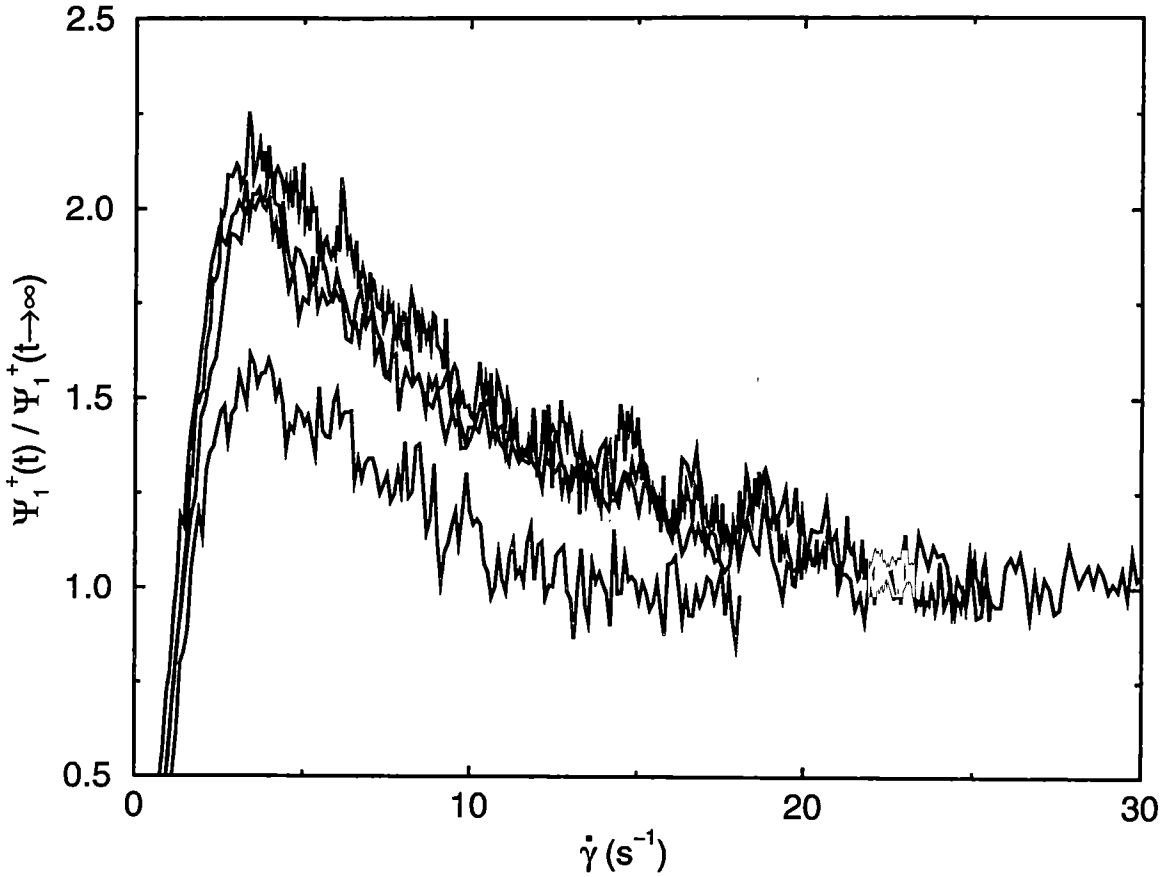

Figure 4.35: First normal stress difference growth coefficient normalized by the steady-state first normal stress coefficient plotted vs. total strain for $C_{100}H_{202}$ (T = 448 K and ρ = 0.75 g/mL). The upper group of curves includes $\dot{\gamma} = 4.25 \times 10^{11}$ s^{-1}, $\dot{\gamma} = 2.72 \times 10^{11}$ s^{-1}, and $\dot{\gamma} = 1.53 \times 10^{11}$ s^{-1}. The lower curve corresponds to $\dot{\gamma} = 3.83 \times 10^{10}$ s^{-1}.

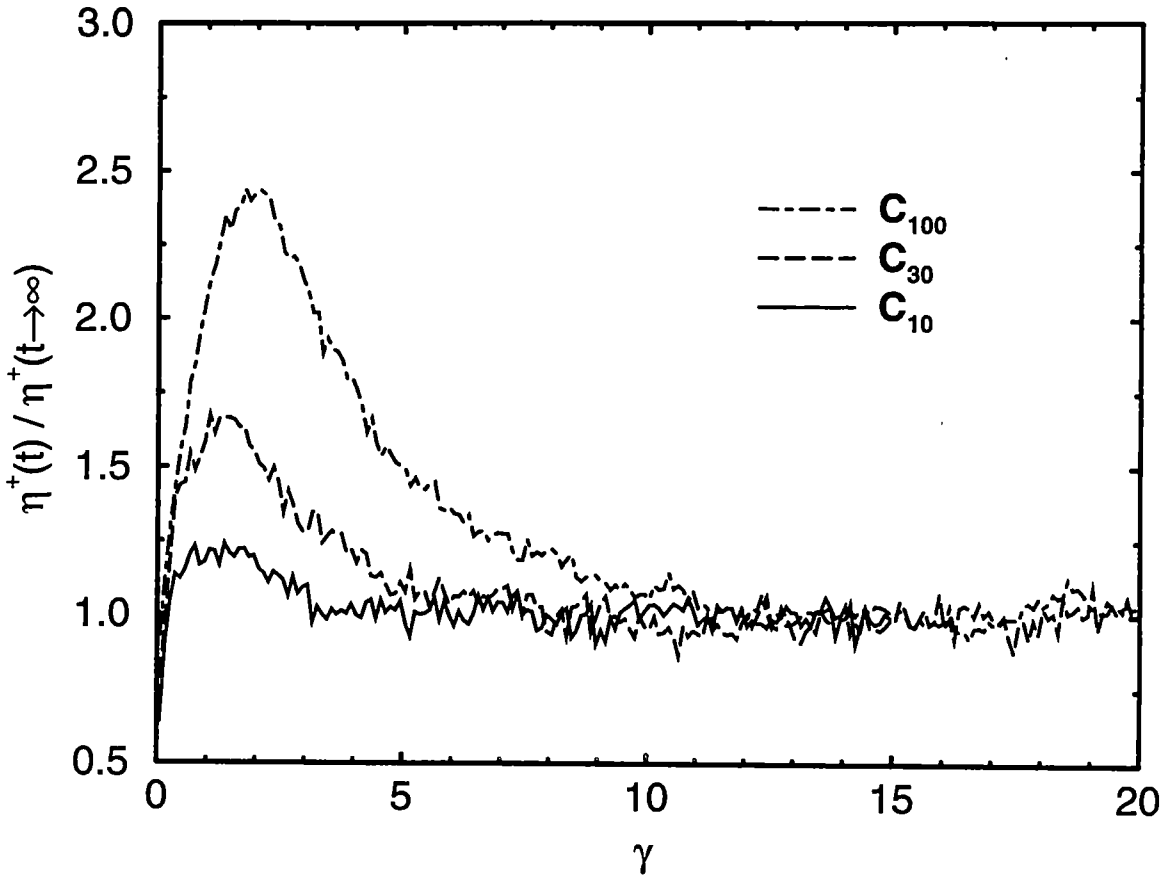

Figure 4.36: Shear stress growth coefficient normalized by the steady-state viscosity plotted vs. total strain ($\gamma = \dot{\gamma}t$) for $C_{100}H_{202}$ ($\rho = 0.75$ g/mL, $T = 448$ K), $C_{30}H_{62}$ ($\rho = 0.76$ g/mL, $T = 372$ K), and $C_{10}H_{22}$ ($\rho = 0.73$ g/mL, $T = 298$ K) at $\dot{\gamma} = 4.25 \times 10^{11}$ s^{-1}.

well, from $\dot{\gamma}t \approx 1.4$ for C_{30} to $\dot{\gamma}t \approx 2.0$ for C_{100}. Figure 4.37 illustrates the transient response of the average chain dimension, this time normalized by its equilibrium value. In fact, R_g^2 passes through a maximum in all three systems, but the change in dimension is much more pronounced for C_{100}. This is not surprising since C_{100}, unlike the other two, is long enough (and therefore flexible enough) to assume quite coiled conformations at equilibrium which will then be uncoiled in the presence of a strong shear field. Though C_{30} and C_{10} do pass through slight maxima, they return to essentially their equilibrium dimension, while C_{100} does not as is seen in Figure 4.38. In this figure, the average squared end-to-end distance is plotted vs. total strain upon onset of shear at $\dot{\gamma} = 1.53 \times 10^{11}$ s^{-1}. As is also evident from the figure, R_{ee}^2 at this shear rate, in addition to passing through a maximum at $\gamma \approx 15$, passes through a minimum at $\gamma \approx 42$ during its approach to steady-state. As seen in Figure 4.39, the percent trans also passes through a maximum upon onset of shear.

4.2.3.4 Stress overshoot: shear-induced ordering

For shorter alkane chains, if the strain rate exceeds the critical value ($\dot{\gamma}_c \approx 1/\tau_1$, where τ_1 is the rotational relaxation time), shear thinning occurs and is accompanied by the alignment of molecules with the flow direction. In Figure 4.40 the alignment angle is plotted vs. total strain γ for the $C_{100}H_{202}$ system at five different strain rates under constant shear-rate start-up tests. The alignment angle decreases with increasing strain and approaches a small limiting value at long times, evidence of extreme alignment in the flow field. The dashed lines in Figure 4.40 illustrate that at all five strain rates the alignment angle is approximately one-half its linear-regime value of 45° at $\gamma \approx 2$. That is, the $C_{100}H_{202}$ melt experiences its maximum shear stress when it has been strained enough to be at the midpoint of the shear-alignment

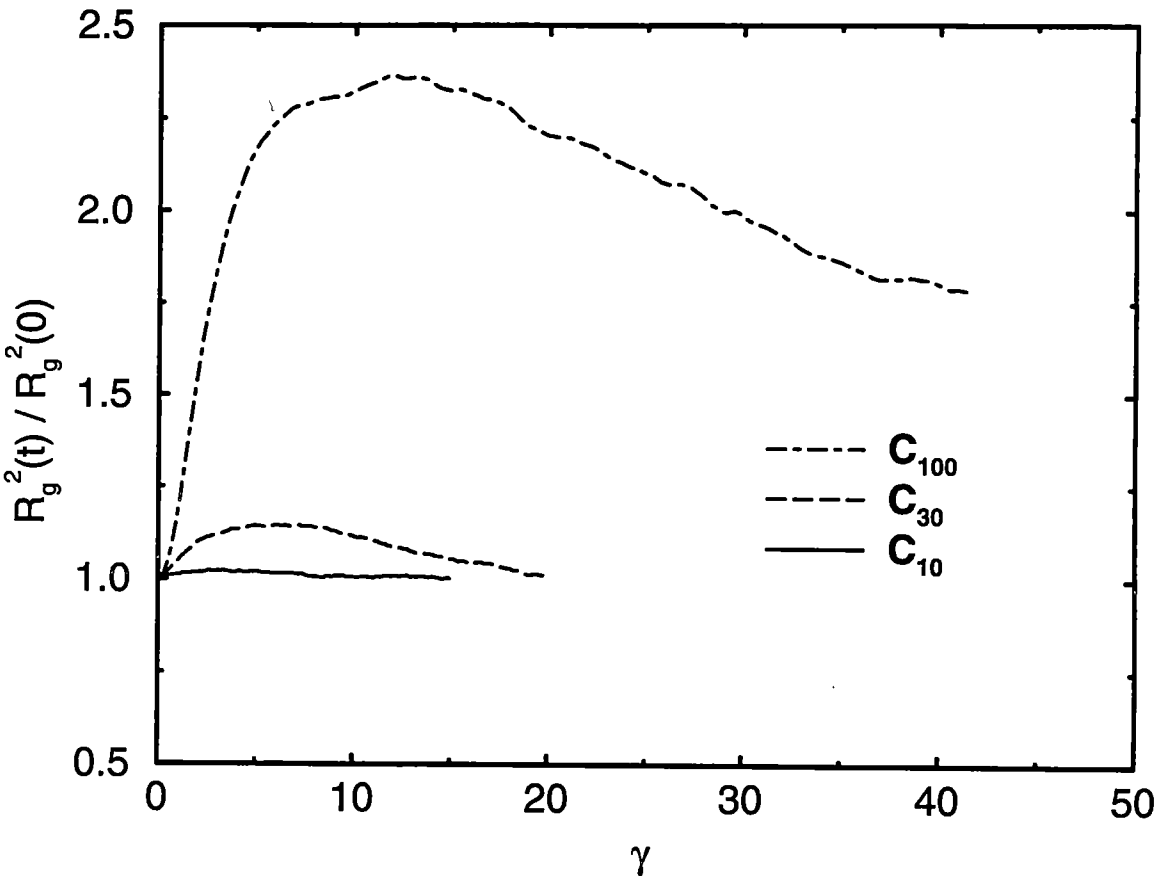

Figure 4.37: Squared radius of gyration divided by its value at t=0 vs. total strain for $C_{100}H_{202}$ (ρ = 0.75 g/mL, T = 448 K), $C_{30}H_{62}$ (ρ = 0.76 g/mL, T = 372 K), and $C_{10}H_{22}$ (ρ = 0.73 g/mL, T = 298 K) under constant shear-rate start-up at $\dot{\gamma} = 4.25 \times 10^{11}$ s^{-1}.

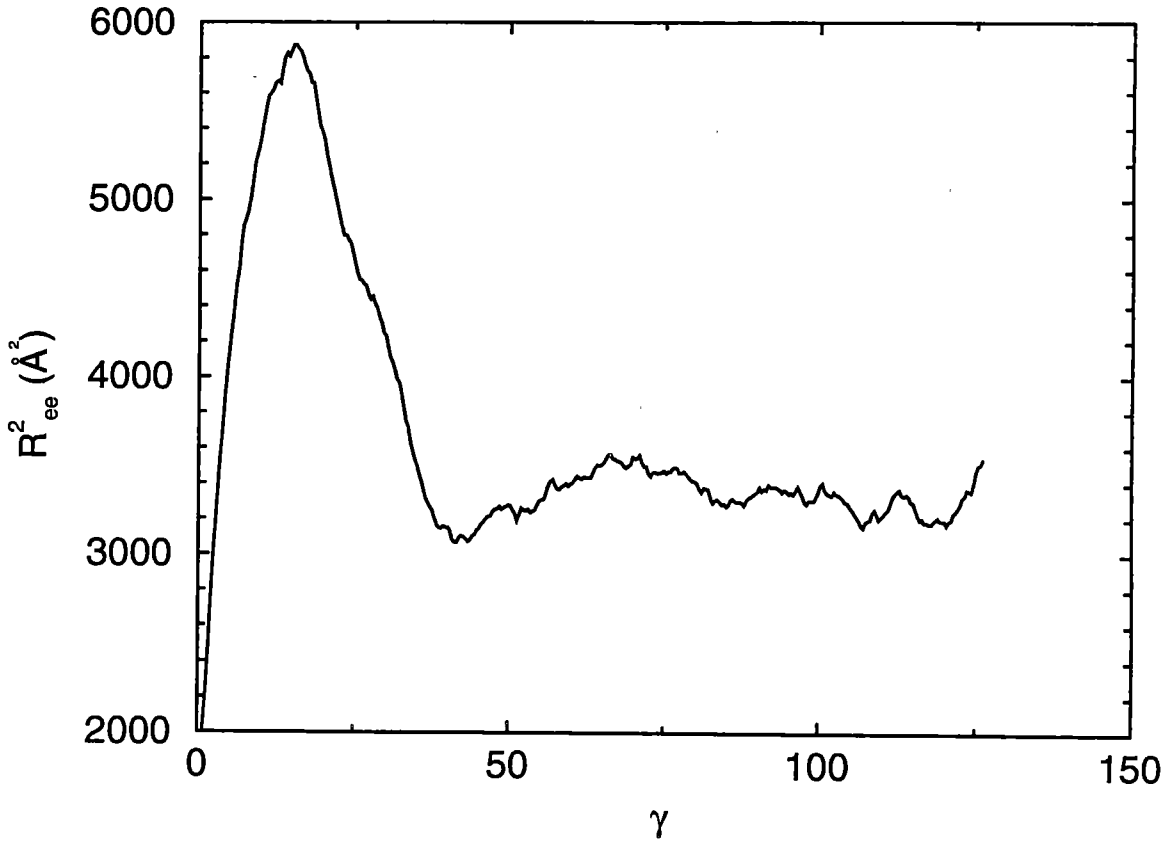

Figure 4.38: Squared end-to-end distance vs. total strain for $C_{100}H_{202}$ under constant shear-rate start-up at $\dot{\gamma} = 1.53 \times 10^{11}$ s^{-1}, $T = 448$ K, and $\rho = 0.75$ g/mL.

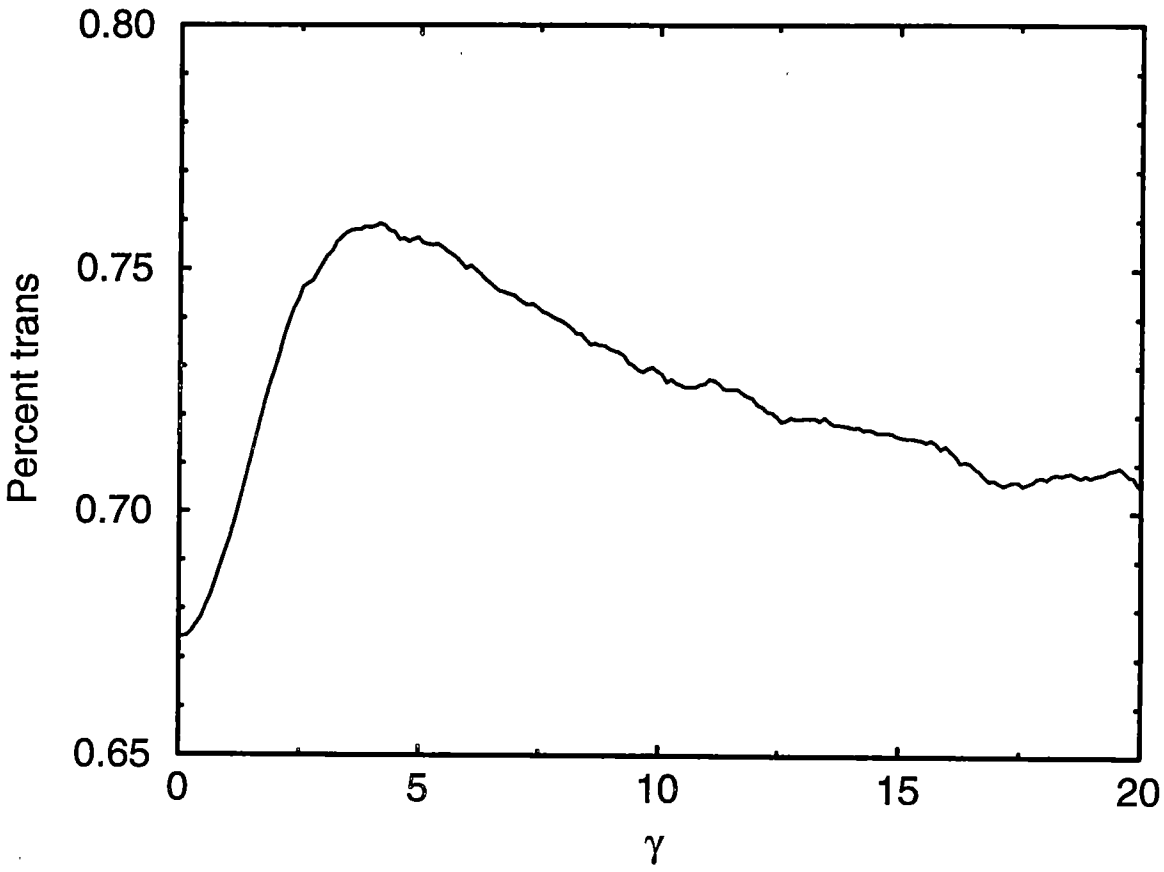

Figure 4.39: Percent trans bonds vs. total strain for $C_{100}H_{202}$ under constant shear-rate start-up at $\dot{\gamma} = 4.25 \times 10^{11}$ s^{-1}, $T = 448$ K, and $\rho = 0.75$ g/mL.

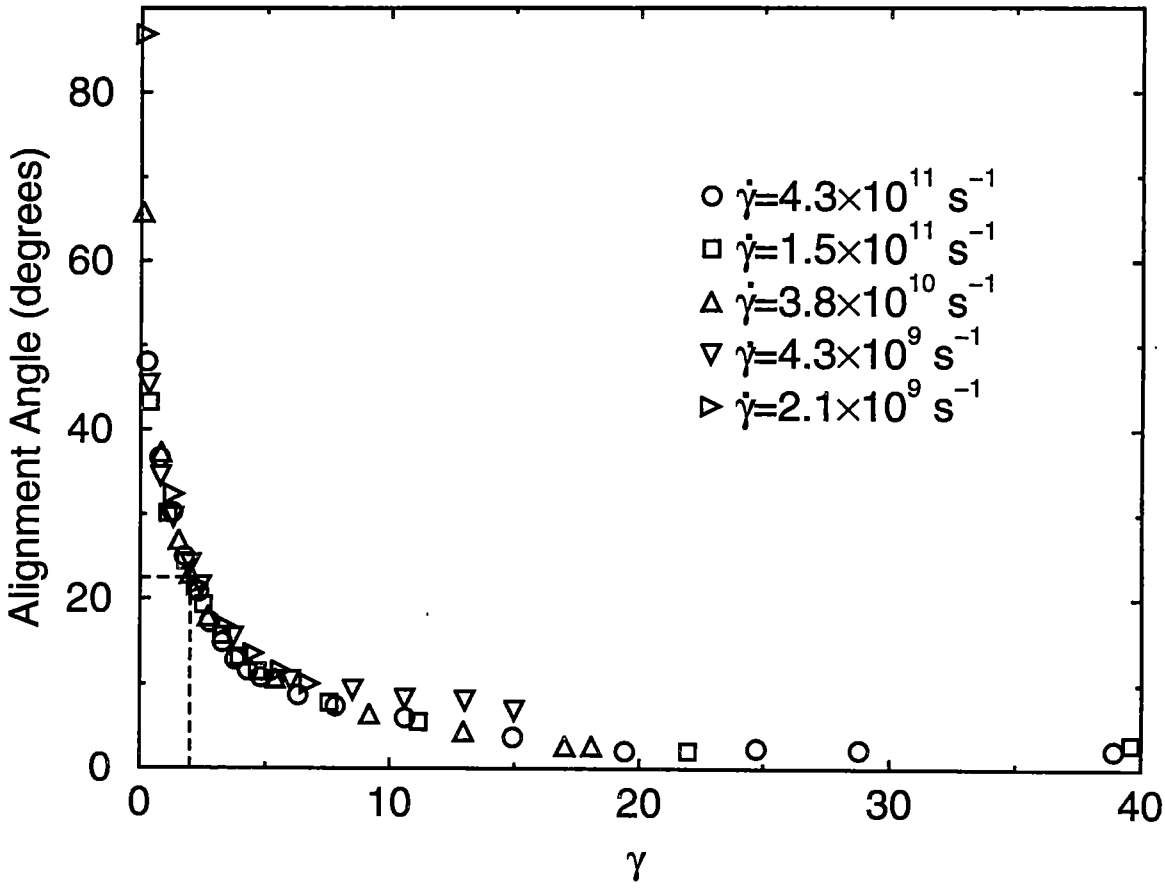

Figure 4.40: Alignment angle with the flow field of the $C_{100}H_{202}$ end-to-end vector vs. total strain for five different strain rates under constant shear-rate start-up tests at $\rho = 0.75$ g/mL and $T = 448$ K. The purpose of the dashed lines is to emphasize the fact that alignment angle has reached half its linear-regime value at $\dot{\gamma}t \approx 2$.

process. Also, at $\dot{\gamma}t \approx 2$, the order parameter in the $C_{100}H_{202}$ system is equal to 0.5, half way between the limiting values of 1 (complete order) and 0 (complete disorder). In Figure 4.41, visualization snapshots illustrate the evolution of the shear-induced molecular alignment for the $C_{100}H_{202}$ system. Different shades of gray are used to help distinguish between the individual molecules.

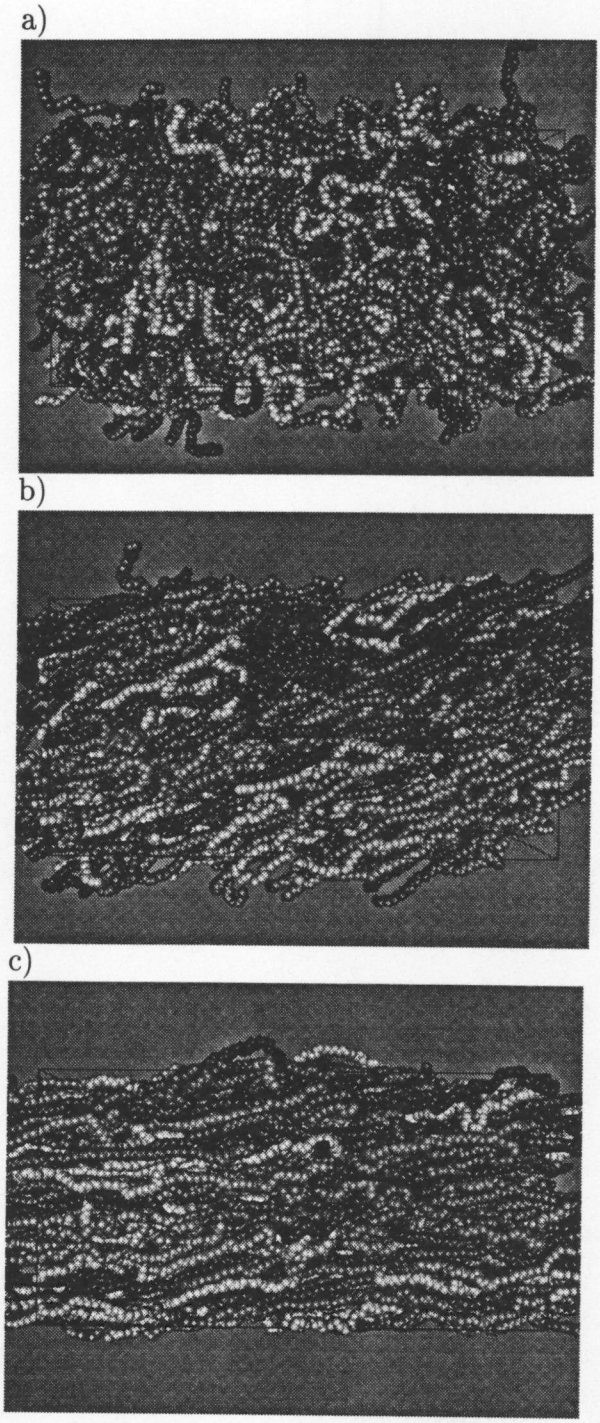

Figure 4.41: Snapshots of the $C_{100}H_{202}$ melt ($\rho = 0.75$ g/mL, $T = 448$ K). Views are into the x-y plane. a) at equilibrium just before the shear field is turned on; b) at $\gamma = 2$ under constant shear-rate start-up at $\dot{\gamma} = 4.3 \times 10^{11}$ s^{-1}; and c) at $\gamma = 20$ under constant shear-rate start-up at $\dot{\gamma} = 4.3 \times 10^{11}$ s^{-1}.

Chapter 5

Concluding remarks

5.1 Conclusions

The general goal of this research was to employ the NEMD simulation technique and a realistic, atomistically detailed molecular model to gain molecular-level insights into the rheology of linear and branched chain molecules (in particular, alkanes of intermediate to long backbone length). The knowledge gained from such a study has potential applications in the design of synthetic lubricants and the improvement of polymer processing techniques. In terms of theoretical interest, the nonlinear viscoelasticity of short-chain, unentangled polymer liquids is, at present, still not well understood. Experimental data are unavailable because of the difficulty of reaching the nonlinear regime in shear rate for short-chain systems, and a successful theory of the nonlinear rheology of short-chain polymers has not yet been developed. Insights gained from molecular simulation will be helpful in the development of theory and the modification of theories developed for longer-chain systems.

Part of this work focused on the rheology of linear and branched alkanes con-

taining thirty total carbons (*n*-triacontane, 9-*n*-octyldocosane, and squalane). These alkanes fall within the mass range present in lubricant basestocks and are, therefore, of particular interest in lubrication applications. The calculated kinematic viscosities of the C_{30} isomers were reported at a variety of strain rates and at temperatures of 311 and 372 K. In all cases, the viscosity showed shear thinning behavior over most of the range of strain rates and a Newtonian plateau at the lowest strain rates. Compared to experiment, NEMD and the united atom model underpredicted the kinematic viscosities of *n*-triacontane and 9-*n*-octyldocosane but accurately predicted the values for squalane (within 15%). Using the rotational relaxation time calculated from the EMD simulation and results from the Rouse model, the predicted zero-shear viscosity for *n*-triacontane was within 16% of the value determined by NEMD. Except for the values of the zero-shear viscosity and rotational relaxation time, the kinematic viscosity versus $\dot{\gamma}$ curves varied little with molecular architecture at a single temperature. Comparing the basic curve shapes at the two temperatures, the primary effect of decreasing temperature was to strengthen the shear thinning behavior (i.e. more negative power-law exponent). The zero-shear viscosities for 9-*n*-octyldocosane and squalane were used to estimate the kinematic viscosity index of those two molecules according to the ASTM standard (ASTM D2270-93 and ASTM D341-93). Within the estimated uncertainty of the simulations and of the experimental data in the literature, the predicted values of the kinematic viscosity index for both 9-*n*-octyldocosane and squalane were in quantitative agreement with experiment. For these two branched C_{30} isomers, 9-*n*-octyldocosane has the highest viscosity index (weakest variation of viscosity with temperature) and is, based on this criterion, the better lubricant candidate. The influence of the shear field on the squared radius of gyration varied according to molecular structure. The linear alkane exhibited a maximum in R_g^2 at intermediate strain rates, and 9-*n*-octyldocosane did not. Squalane,

with its many short side-branches, showed a slight maximum in R_g^2, behavior intermediate between that of the long, linear alkane and the long-branched alkane. In each case, the average chain dimension decreased with increasing $\dot{\gamma}$ at high $\dot{\gamma}$. Since the presence of branches would inherently hinder the ability to minimize a chain's exposure to multiple shear planes, it may not be surprising that the variation of R_g^2 with $\dot{\gamma}$ was less dramatic for the branched alkanes. In all cases the variation is fairly modest: at most a 10% increase or decrease. All three molecules exhibited significant shear-induced chain alignment. While at low $\dot{\gamma}$, the angle increased with decreasing strain rate as it approached linear-regime behavior, at high $\dot{\gamma}$ it approached a small limiting value between 6 and 11°. The limiting value of the angle at high $\dot{\gamma}$ was observed to be dependent on the length of the molecule's backbone. As the chain-backbone length increased from 9-*n*-octyldocosane to squalane to *n*-triacontane, the limiting alignment angle decreased from approximately 10.5 to 7.7 to 6.8°. In addition, the high-$\dot{\gamma}$ value of the alignment angle varied only slightly with temperature for the same molecule. For the normal alkane only, a minimum was observed in the average hydrostatic pressure and intermolecular LJ potential energy at the strain rate just prior to the occurrence the maximum in R_g^2.

Utilizing the same united atom potential model and NEMD algorithm as used for the C_{30} study, simulations of a monodisperse $C_{100}H_{202}$ polyethylene melt at 448 K and 0.75 g/mL were also performed. The study focused on both steady-state shear and the transient response upon onset of shear. Shear thinning was observed in the viscosity and normal stress coefficients over the range of strain rates studied. A minimum in the hydrostatic pressure was observed at an intermediate strain rate that was associated with a minimum in the intermolecular Lennard-Jones potential energy as well as transitions in the strain-rate-dependent behavior of several other viscous and structural properties of the system. The shear field also imposed significant

alignment of the chains with the flow direction, approaching a limiting angle of 3° at high strain rate. In addition, the self-diffusion coefficients (calculated in terms of the unconvected positions according to the Cummings-Wang formalism) were markedly enhanced under shear compared to the equilibrium state (up to two orders of magnitude at the highest shear rate studied). This shear-enhancement of diffusion for $C_{100}H_{202}$ was much larger than the factor of 2 enhancement observed previously for the Lennard-Jones fluid at its triple point [165]. Under constant shear-rate start-up test, significant stress overshoot was observed at a variety of strain rates. Decomposition of the stress into the components arising from the various contributions to the pressure tensor revealed that all six contributions to the shear stress growth coefficient passed through extrema during their approach to steady state. The kinetic and torsional contributions passed through minima. The bond-stretching, intramolecular-LJ, and intermolecular-LJ contributions all passed through maxima at $\dot{\gamma}t \approx 2$. The bond-angle-bending contribution passed through a minimum followed by a maximum. The bond-stretching and intermolecular-LJ contributions dominated the stress overshoot. The former provides confirmation that the stress overshoot is closely related to the stretching of the individual chain-segments under the influence of the flow field. The latter suggests that, as the chains are being straightened-out and aligned, the shearing of molecules past one another causes strong intermolecular "frictional" interactions that also contribute significantly to the transient behavior of the shear stress. The transient response of Ψ_1 was also dominated by bond-stretching and intermolecular-LJ contributions of approximately equal magnitude, while the overshoot in Ψ_2 was dominated by the intermolecular-LJ contribution alone. When the shear stress growth coefficients at a variety of strain rates were normalized by the corresponding steady state viscosity and plotted vs. total strain, the curves for strain rates varying over two orders of magnitude were collapsed into two master curves. In

all cases, the peak viscosity occurred at $\gamma \approx 2$, in quantitative agreement with predictions from the Doi-Edwards (DE) model. This prompted explicit comparison to the stress overshoot curve predicted by the DE model. Fitting the curves to the time required to reach steady state (i.e. taking into account the shear-rate-dependence of the terminal relaxation time), the DE model quantitatively predicted the peak height of the stress overshoot. In addition, the shear-rate-dependence of the terminal relaxation time was found to be consistent with the strain-rate dependence of the self-diffusion coefficient in the flow direction. Also, at the maximum of shear stress overshoot, the molecular orientational order and the alignment angle were found to be mid-way between those characteristic of Newtonian flow and full alignment with the flow.

5.2 Implications of these results

The ability to directly observe and study the dynamical behavior of individual molecules and thus gain molecular-level insight into a system's behavior is the key advantage of an MD simulation over analytic theory and many types of macroscopic experimental measurements. Recent advances in models [26] and algorithms [27] as well as the advent of massively parallel supercomputers have now made such detailed simulations possible for chain systems of significant practical interest, such as the alkanes examined in this study. Among the various interesting observations arising from this work, two stand out as most significant: 1) the nonequilibrium molecular dynamics simulation technique in combination with a realistic, computationally efficient molecular model such as that of Siepmann *et al.* [26] is able to make quantitatively accurate predictions of the kinematic viscosity index of alkanes in the mass range of interest to lubricant basestocks and 2) even though the C_{100} system is too short to experience

the sort of entanglements on which Doi-Edwards theory is based, the stress overshoot curves calculated for C_{100} are in good quantitative agreement with DE theory if the terminal relaxation time is assumed to have the same strain-rate dependence as the calculated self-diffusion coefficient in the flow direction.

Though squalane's viscosity was predicted accurately (within 15%), more generally, united atom models have usually been found to underestimate experimental viscosities [148], typically underpredicting them by up to 50 %. This was true for 9-*n*-octyldocosane using the SKS model. Even so, the predicted kinematic viscosity index values for both 9-*n*-octyldocosane and squalane were in quantitative agreement with experiment and represent the first such predictions by molecular simulation. Thus, this same general potential model and computational approach can be used to predict this important lubricant property for potential lubricants prior to their synthesis, offering the possibility of simulation-guided lubricant design.

The question of why the reptation model should be applicable to a melt of $C_{100}H_{202}$ alkane molecules is worth examining. The physical picture underlying the reptation model of de Gennes (and the DE theory and its derivatives which are based on it) is that very long chain molecules become so entangled that the only mechanism of (center of mass) chain motion is by "reptation" motion in which one end of the chain moves into a near-by region of free volume, and the rest of the chain is constrained to follow snake-like through the tubular volume occupied by the chain itself because all of the surrounding volume is occupied by slowly moving segments. Usually, it is thought that the reptation model does not apply to the motion of shorter chain molecules ($C_n, n \lesssim 300$ [166]) because they are too short to become entangled. In the high strain rate simulations described in Chapter 4, the rate of center of mass chain motion (due to shear) is fast compared to the rate of motion due to diffusion (even shear-enhanced diffusion). Thus, at these high strain rates, even short chains may be

effectively confined to a "tube" formed by the surrounding chains on the timescale of the shearing motion. It is not our intention to vigorously argue that the behavior of these short chain systems at high strain rate is accurately described by the reptation picture. Instead, we simply observe a striking similarity between the behavior upon onset of shear predicted by a mathematical model developed to describe entangled polymers at experimentally accessible shear rates and observed in simulations of a short-chain model polyethylene melt at the extremely high shear rates accessible to simulation but inaccessible to experiment. Assuming the origin of this similarity to be fundamental rather than coincidental, we speculate that the imposition on the chains of shearing motion on a timescale much faster than that of motion due to diffusion may be the common feature of these two systems that leads to the sort of stress overshoot behavior predicted by the DE model and observed in simulations of $C_{100}H_{202}$.

Recently, effort has been made by a number of authors [37, 38, 39, 40, 41, 42, 43, 44, 45] to modify DE theory in order to improve its predictions for various aspects of the nonlinear viscoelasticity of entangled polymer melts in general and to achieve consistency with the empirical Cox-Merz rule in particular [37, 38, 39, 40]. The concept of "convective constraint release" (CCR) is prominent in several of these theoretical treatments [37, 38, 39, 43, 45]. The basic premise of the CCR concept is that at high rates of shear the flow convects entangled chains, one relative to another, at a rate faster than the reptation mechanism [38]. Ianniruberto and Marrucci argue that CCR could result in a relaxation time that decreases linearly with increasing $\dot{\gamma}$ under fast flow conditions for entangled systems [37], though Mhetar and Archer argue that CCR might lead to a renewal time that is either unchanged or increases with increasing $\dot{\gamma}$ [40]. We believe that shear-enhanced diffusion, which we have quantified for our model $C_{100}H_{202}$ melt and shown to be consistent with its strain-rate-dependent

relaxation time observed under constant-shear-rate start-up tests, offers a possible additional or alternative mechanism for strain-rate-dependent relaxation times in the fast flows of polymers. This is a possibility that is not currently being considered in the literature but could have important implications for the current effort in the rheological community to improve the state of the art in the theoretical treatment of polymer melts undergoing fast flows.

5.3 Future work

The NEMD study of lubricant basestocks can be extended in several ways. Obviously, simulations of $C_{30}H_{62}$ isomers for which no experimental data is available would be of particular interest (e.g. a 24-carbon backbone with two propyl sidechains, a 16-carbon backbone with two heptyl sidechains attached at the eighth carbon, or an isomer containing a cyclic structure). The lack of experimental density data would complicate the choice of density for NVT simulations of such systems. The density could be estimated from experimental data available for other closely-related structures, or a constant-pressure simulation code could be employed. In addition, an investigation of the viscosity predictions of other potential models (such as the AUA model of Toxvaerd [82] and the TraPPE explicit-atom model [89]) would be of interest in identifying a transferable model that can consistently predict accurate viscosities for a variety of chain architectures. Also, given the success of the SKS united atom model in predicting the VI, a natural next step would be to predict the pressure-viscosity coefficients of these lubricant molecules at the extreme pressures ($P \simeq 10^9$ Pa [28, 29]) relevant to many lubrication applications.

Interesting extensions of the C_{100} work would include characterization of how the stress overshoot behavior and the shear-enhanced diffusion depend on temperature,

chain length (long chains somewhat shorter or longer than C_{100}), and chain architecture. Also, examination of the stress relaxation upon cessation shear for C_{100} would be of interest. Application to C_{100} of the geometric criterion used by Kröger and Voigt to model entanglement would be interesting to determine if the melt is at all entangled according to that definition. In addition, explicit comparison between the C_{100} simulations and theory incorporating convective constraint release (CCR) would be instructive. If a prediction from CCR theory appropriate for C_{100} could be identified, it might shed light on whether the strain-rate-dependent relaxation times observed in the C_{100} simulations are of diffusive or convective origin.

Finally, Baranyai and Cummings [167] and Todd and Daivis [168, 169] have recently applied periodic boundary conditions developed by Kraynik and Reinelt [170] to perform steady-state NEMD simulations of simple liquids experiencing planar elongational flow. This development is especially exciting since elongational flow, though as important industrially as shear flow, has not previously been studied in steady-state simulations of molecular liquids due to technical limitations of the simulation algorithm. The new algorithm does not share these same limitations and can be applied to perform steady-state simulations of chain molecules under elongational flow. Clearly, such simulations for the C_{30} and C_{100} systems would be of great scientific and practical importance.

BIBLIOGRAPHY

Bibliography

[1] J. Denis. The relationships between structure and rheological properties of hydrocarbons and oxygenated compounds used as base stocks. *Journal of Synthetic Lubrication*, 1:201–219, 1984.

[2] A.P.I. *API 42: Properties of Hydrocarbons of High Molecular Weight.* American Petroleum Institute, 1966.

[3] M.P. Allen and D.J. Tildesley. *Computer Simulations of Liquids.* Oxford Science Publications, 1987.

[4] K. Binder. *Monte Carlo and Molecular Dynamics Simulations in Polymer Science*, chapter 1. Oxford University Press, 1995.

[5] W. Tschöp, K. Kremer, J. Batoulis, T. Bürger, and O. Hahn. Simulation of polymer melts. I. Coarse-graining procedure for polycarbonates. *Acta Polymerica*, 49:61–74, 1998.

[6] M.R.S. Pinches, D.J. Tildesley, and W. Smith. Large scale molecular dynamics on parallel computers using the link-cell algorithm. *Molecular Simulation*, 6:51–87, 1991.

[7] R. Bhupathiraju, P.T. Cummings, and H.D. Cochran. An efficient parallel algorithm for non-equilibrium molecular dynamics simulations of very large systems in planar Couette flow. *Molecular Physics*, 88:1665–1670, 1996.

[8] M. Doi and S.F. Edwards. *The Theory of Polymer Dynamics.* Oxford Science Publications, 1988.

[9] T.J. Murphy and J.L. Aguirre. Brownian motion of n interacting particles. I. Extension of the Einstein diffusion relation to the n-particle case. *Journal of Chemical Physics*, 57:2098–2104, 1972.

[10] D.L. Ermak and J.A. McCammon. Brownian dynamics with hydrodynamic interactions. *Journal of Chemical Physics*, 69:1352–1360, 1978.

[11] P.M. Morse. Demand for synthetic lubricants on the rise. *Chemical & Engineering News*, 76:21–22, 1998.

[12] A.K. Mehrotra. A generalized viscosity equation for pure heavy hydrocarbons. *Industrial & Engineering Chemistry Research*, 30:420–427, 1991.

[13] U. Yahsi. Viscous behavior of linear and three-branch alkanes: Linking the equilibrium and transport theories. *Journal of Polymer Science: Part B: Polymer Physics*, 37:879–887, 1999.

[14] V. Eychenne and Z. Mouloungui. Relationships between structure and lubricating properties of neopentylpolyol esters. *Industrial & Engineering Chemistry Research*, 37:4835–4843, 1998.

[15] D.J. Evans and G.P. Morriss. *Statistical Mechanics of Nonequilibrium Liquids.* Academic, 1990.

[16] G.P. Morriss, P.J. Daivis, and D.J. Evans. The rheology of n-alkanes: Decane and eicosane. *Journal of Chemical Physics*, 94:7420–7433, 1991.

[17] K.P. Travis and D.J. Evans. On the rheology of n-eicosane. *Molecular Simulation*, 17:157–164, 1996.

[18] S.T. Cui, S.A. Gupta, and P.T. Cummings. Molecular dynamics simulations of the rheology of normal decane, hexadecane, and tetracosane. *Journal of Chemical Physics*, 105:1214–1220, 1996.

[19] M. Mondello, G.S. Grest, E.B. Webb III, and P. Peczak. Dynamics of n-alkanes: Comparison to Rouse model. *Journal of Chemical Physics*, 109:798–805, 1998.

[20] C.J. Mundy, S. Balasubramanian, K. Bagchi, J.I. Siepmann, and M.L. Klein. Equilibrium and non-equilibrium simulation studies of fluid alkanes in bulk and at interfaces. *Faraday Transactions*, 104:17–36, 1996.

[21] R. Khare, J. de Pablo, and A. Yethiraj. Rheological, thermodynamic, and structural studies of linear and branched alkanes under shear. *Journal of Chemical Physics*, 107:6956–6964, 1997.

[22] S.A. Gupta, P.T. Cummings, and H.D. Cochran. Shear behavior of squalane and tetracosane under extreme confinement. I. Model, simulation method, and interfacial slip. *Journal of Chemical Physics*, 107:10316–10326, 1997.

[23] S.A. Gupta, P.T. Cummings, and H.D. Cochran. Shear behavior of squalane and tetracosane under extreme confinement. II. Confined film structure. *Journal of Chemical Physics*, 107:10327–10334, 1997.

[24] S.A. Gupta, P.T. Cummings, and H.D. Cochran. Shear behavior of squalane and tetracosane under extreme confinement. III. Effect of continement on viscosity. *Journal of Chemical Physics*, 107:10327–10334, 1997.

[25] M. Lahtela, M. Linnolahti, T.A. Pakkanen, and R.L. Rowley. Computer simulations of branched alkanes: The effect of side chain and its position on rhelological behavior. *Journal of Chemical Physics*, 108:2626–2630, 1998.

[26] J.I. Siepmann, S. Karaborni, and B. Smit. Simulating the critical behavior of complex fluids. *Nature*, 365:330–332, 1993.

[27] M.E. Tuckerman, B.J. Berne, and G.J. Martyna. Reversible multiple time step molecular dynamics. *Journal of Chemical Physics*, 97:1990–2001, 1992.

[28] S. Chynoweth, U.C. Klomp, and L.E. Scales. Simulations of organic liquids using pseudo-pairwise interatomic forces on a toroidal transputer array. *Computer Physics Communications*, 62:297–306, 1991.

[29] R.A. Gray, S. Chynoweth, Y. Michopoulos, and G.S. Pawley. Shear localisation in simulated fluid. *Europhysics Letters*, 43:491–496, 1998.

[30] W. Paul, G.D. Smith, D.Y. Yoon, B. Farago, S. Rathgeber, A. Zirkel, L. Wilner, and D. Richter. Chain motion in an unentangled polyethylene melt: A critical test of the Rouse model by molecular dynamics simulations and neutron spin echo spectroscopy. *Physical Review Letters*, 80:2346–2349, 1998.

[31] V.A. Harmandaris, V.G. Mavrantzas, and D.N. Theodorou. Atomistic molecular dynamics simulation of polydisperse linear polyethylene melts. *Macromolecules*, 31:7934–7943, 1998.

[32] P.G. de Gennes. Reptation of a polymer chain in the presence of fixed obstacles. *Journal of Chemical Physics*, 55:572–579, 1971.

[33] M. Doi and S. Edwards. Dynamics of concentrated polymer systems. Part 3. The constitutive equation. *Journal of the Chemical Society Faraday Transactions 2*, 74:1818–1832, 1978.

[34] M. Doi and S. Edwards. Dynamics of concentrated polymer systems. part 4. rheological properties. *Journal of the Chemical Society Faraday Transactions 2*, 75:38–54, 1979.

[35] D. Pearson, E. Herbolzheimer, N. Grizzuti, and G. Marrucci. Transient behavior of entangled polymers at high shear rates. *Journal of Polymer Science: Part B: Polymer Physics*, 29:1589–1597, 1991.

[36] E.V. Menezes and W.W. Graessley. Nonlinear rheological behavior of polymer systems for several shear-flow histories. *Journal of Polymer Science: Part B: Polymer Physics*, 20:1817–1833, 1982.

[37] G. Marrucci. Dynamics of entanglements: A nonlinear model consistent with the Cox-Merz rule. *Journal of Non-Newtonian Fluid Mechanics*, 62:279–289, 1996.

[38] G. Ianniruberto and G. Marrucci. On compatability of the Cox-Merz rule with the model of Doi and Edwards. *Journal of Non-Newtonian Fluid Mechanics*, 65:241–246, 1996.

[39] G. Marrucci and G. Ianniruberto. Open problems in tube models for concentrated polymers. *Journal of Non-Newtonian Fluid Mechanics*, 82:275–286, 1999.

[40] V. Mhetar and L.A. Archer. Nonlinear viscoelasticity of entangled polymeric liquids. *Journal of Non-Newtonian Fluid Mechanics*, 81:71–81, 1999.

[41] A. Ait-Kadi, A. Ramazani, M. Grmela, and C. Zhou. "Volume preserving" rheological models for polymer melts and solutions using the GENERIC formalism. *Journal of Rheology*, 43:51–72, 1999.

[42] J. Remmelgas, G. Harrison, and L.G. Leal. A differential constitutive equation for entangled polymer solutions. *Journal of Non-Newtonian Fluid Mechanics*, 80:115–134, 1999.

[43] D.W. Mead, R.G. Larson, and M. Doi. A molecular theory for fast flows of entangled polymers. *Macromolecules*, 31:7895–7914, 1998.

[44] H.C. Öttinger and A.N. Beris. Thermodynamically consistent reptation model without independent alignment. *Journal of Chemical Physics*, 110:6593–6596, 1999.

[45] H.C. Öttinger. Thermodynamically admissible reptation models with anisotropic tube cross sections and convective constraint release. *Journal of Non-Newtonian Fluid Mechanics*, in press.

[46] W. Paul, D.Y. Yoon, and G.D. Smith. An optimized united atom model for simulations of polymethylene melts. *Journal of Chemical Physics*, 103:1702–1709, 1995.

[47] G.D. Smith and D.Y. Yoon. Equilibrium and dynamic properties of polymethylene melts from molecular dynamics simulations. I. *n*-tridecane. *Journal of Chemical Physics*, 100:649–658, 1994.

[48] R.B. Bird. private communication.

[49] R.B. Bird, R.C. Armstrong, and O. Hassager. *Dynamics of Polymeric Liquids: Fluid Mechanics*, volume 1. Wiley, 2nd. edition, 1987.

[50] R.B. Bird, R.C. Armstrong, and O. Hassager. *Dynamics of Polymeric Liquids: Kinetic Theory*, volume 2. Wiley, 2nd. edition, 1987.

[51] J.N. Cosby and L.H. Sutherland. The synthesis and properties of hyrdrocarbons of high molecular weight. *Proceedings of the American Petroleum Institute*, 22:13–24, 1941.

[52] R.W. Schiessler, J.N. Cosby, D.G. Clarke, C.S. Rowland, W.S. Sloatman, and C.H. Herr. The synthesis and properties of hydrocarbons of high molecular weight II. *Proceedings of the American Petroleum Institute*, 23:15–36, 1942.

[53] R.W. Schiessler, C.H. Herr, A.W. Rytina, C.A. Weisel, F. Fischl, R.L. McLaughlin, and H.H. Kuehner. The synthesis and properties of hydrocarbons of high molecular weight IV. *Proceedings of the American Petroleum Institute*, 26:254–302, 1946.

[54] R.W. Schiessler, D.G. Clarke, C.S. Rowland, W.S. Sloatman, and C.H. Herr. The synthesis and properties of hydrocarbons of high molecular weight III. *Petroleum Refiner*, 22:390–409, 1943.

[55] R.W. Schiessler, J.N. Cosby, D.G. Clarke, C.S. Rowland, W.S. Sloatman, and C.H. Herr. Synthesis and properties of hydrocarbons of high molecular weight. *Petroleum Refiner*, 21:383–400, 1942.

[56] E.M. Griest, W. Webb, and R.W. Schiessler. Effect of pressure on viscosity of higher hydrocarbons and their mixtures. *Journal of Chemical Physics*, 29:711–720, 1958.

[57] R.R. Nelson, W. Webb, and J.A. Dixon. First-order phase transitions of six normal paraffins at elevated pressures. *Journal of Chemical Physics*, 33:1756–1764, 1960.

[58] D.A. Lowitz, J.W. Spencer, W. Webb, and R.W. Schiessler. Temperature-pressure-structure effects on the viscosity of several high hydrocarbons. *Journal of Chemical Physics*, 30:73–83, 1959.

[59] E.W. Dean and G.H.B. Davis. Viscosity variations of oils with temperature. *Chemical & Metallurgical Engineering*, 36:618–619, 1929.

[60] E.W. Hardiman and A.H. Nissan. A rational basis for the viscosity index system. Part I. *J. Inst. Pet.*, 31:255–270, 1945.

[61] D.S. Pearson, G. Ver Strate, E. von Meerwall, and F.C. Schilling. Viscosity and self-diffusion coefficient of linear polyethylene. *Macromolecules*, 20:1133–1141, 1987.

[62] P.E. Rouse Jr. A theory of the linear viscoelastic properties of dilute solutions of coiling polymers. *Journal of Chemical Physics*, 21:1272–1280, 1953.

[63] D.S. Pearson, L.J. Fetters, W.W. Graessley, G. Ver Strate, and E. von Meerwall. Viscosity and self-diffusion coefficient of hydrogenated polybutadiene. *Macromolecules*, 27:711–719, 1994.

[64] E.V. Menezes and W.W. Graessley. Study of the nonlinear response of a polymer solution to various uniaxial shear flow histories. *Rheologica Acta*, 19:38–50, 1980.

[65] M.H. Wagner, H. Bastian, P. Ehrecke, M. Kraft, P. Hachmann, and J. Meissner. Nonlinear viscoelastic characterization of a linear polyethylene (HDPE) melt in rotational and irrotational flows. *Journal of Non-Newtonian Fluid Mechanics*, 79:283–296, 1998.

[66] M. Kraft. *Untersuchungen zur scherinduzierten rheologischen anisotripie von verschiedenen polyethylen-schmelzen.* PhD thesis, ETH Zürich, 1996.

[67] P. Hachmann. *Multiaxiale dehnung von polymerschmelzen.* PhD thesis, ETH Zürich, 1996.

[68] M.H. Wagner. The origin of the C_2 term in rubber elasticity. *Journal of Rheology*, 38:655–679, 1994.

[69] S.F. Edwards. Statistical mechanics with topological constraints: I. *Proceedings of the Physical Society*, 91:513–519, 1967.

[70] S.F. Edwards. The statistical mechanics of polymerized material. *Proceedings of the Physical Society*, 92:9–16, 1967.

[71] M. Doi and S. Edwards. Dynamics of concentrated polymer systems. Part 1. Brownian motion in the equilibrium state. *Journal of the Chemical Society Faraday Transactions 2*, 74:1789–1801, 1978.

[72] M. Doi and S. Edwards. Dynamics of concentrated polymer systems. Part 2. Molecular motion under flow. *Journal of the Chemical Society Faraday Transactions 2*, 74:1802–1817, 1978.

[73] J.D. Ferry. *Viscoelastic Properties of Polymers*, page 244. Wiley, 1980.

[74] G. Marrucci and N. Grizzuti. Fast flows of concentrated polymers: Predictions of the tube model on chain stretching. *Gazzetta Chimica Italiana*, 118:179–185, 1988.

[75] D.S. Pearson, A.D. Kiss, L.J. Fetters, and M. Doi. Flow-induced birefringence of concentrated polyisoprene solutions. *Journal of Rheology*, 33:517–535, 1989.

[76] D.W. Mead and L.G. Leal. The reptation model with segmental stretch. I. Basic equations and general properties. *Rheologica Acta*, 34:339–359, 1995.

[77] D.W. Mead, D. Yavich, and L.G. Leal. The reptation model with segmental stretch. II. Steady flow properties. *Rheologica Acta*, 34:360–383, 1995.

[78] M. Mondello and G.S. Grest. Molecular dynamics of linear and branched alkanes. *Journal of Chemical Physics*, 103:7156–7165, 1995.

[79] W.L. Jorgensen, J.D. Madura, and C.J. Swenson. Optimized intermolecular potential functions for liquid hydrocarbons. *Journal of the American Chemical Society*, 106:6638–6646, 1984.

[80] J.I. Siepmann, M.G. Martin, C.J. Mundy, and M.L. Klein. Intermolecular potentials for branched alkanes and the vapour-liquid phase equilibria of *n*-heptane, 2-methylhexane, and 3-ethylpentane. *Molecular Physics*, 90:687–693, 1997.

[81] M.G. Martin and J.I. Siepmann. Transferable potentials for phase equilibria. 1. United-atom description of *n*-alkanes. *Journal of Physical Chemistry B*, 102:2569–2577, 1998.

[82] S. Toxvaerd. Molecular dynamics calculation of the equation of state of alkanes. *Journal of Chemical Physics*, 93:4290–4295, 1990.

[83] W.L. Jorgensen, D.S. Maxwell, and J. Tirado-Rives. Development and testing of the OPLS all-atom force field on conformational energetics and properties of organic liquids. *Journal of the American Chemical Society*, 118:11225–11236, 1996.

[84] D.E. Williams. Nonbonded potential parameters derived from crystalline hydrocarbons. *Journal of Chemical Physics*, 47:4680–4684, 1967.

[85] J. R. Errington and A. Z. Panagiotopoulos. A new intermolecular potential model for the *n*-alkanes homologous series. *Journal of Physical Chemistry B*, 1999. submitted.

[86] J.-P. Ryckaert and A. Bellemans. Molecular dynamics of liquid alkanes. *Discussions of the Faraday Society*, 66:95–106, 1978.

[87] S. Chynoweth and Y. Michopoulos. An improved model for *n*-hexadecane molecular dynamics simulations under extreme conditions. *Molecular Physics*, 81:133–141, 1994.

[88] M.G. Martin and J.I. Siepmann. Novel configurational-bias Monte Carlo method for branched molecules. Transferable potentials for phase equilibria. 2. United-atom description of branched alkanes. *Journal of Physical Chemistry B*, 103:4508–4517, 1999.

[89] B. Chen and J.I. Siepmann. Transferable potentials for phase equilibria. 3. Explicit-hydrogen description of normal alkanes. *Journal of Physical Chemistry B*, 103:5370–5379, 1999.

[90] G.S. Grest and K. Kremer. Molecular dynamics simulation for polymers in the presence of a heat bath. *Physical Review A*, 33:3628–3631, 1986.

[91] K. Kremer, G.S. Grest, and I. Carmesin. Crossover from Rouse to reptation dynamics: A molecular dynamics simulation. *Physical Review Letters*, 61:566–569, 1998.

[92] K. Kremer and G.S. Grest. Dynamics of entangled linear polymer melts: A molecular-dynamics simulation. *Journal of Chemical Physics*, 92:5057–5086, 1990.

[93] Z. Xu, J. de Pablo, and S. Kim. Transport properties of polymer melts from nonequilibrium molecular dynamics. *Journal of Chemical Physics*, 102:5836–5844, 1995.

[94] Z. Xu, R. Khare, J.J. de Pablo, and S. Kim. On the calculation of transport properties of polymer melts from nonequilibrium molecular dynamics. *Journal of Chemical Physics*, 106:8285–8286, 1997.

[95] M. Kröger, W. Loose, and S. Hess. Rheology and structural changes of polymer melts via nonequilibrium molecular dynamics. *Journal of Rheology*, 37:1057–1079, 1993.

[96] M. Kröger. NEMD computer simulation of polymer melt rheology. *Rheology 95*, 5:66–71, 1995.

[97] M. Kröger and H. Voigt. On a quantity describing the degree of chain entanglement in linear polymer systems. *Macromolecular Theory and Simulation*, 3:639–647, 1994.

[98] D.Y. Yoon, G.D. Smith, and T. Matsuda. A comparison of a united atom and an explicit atom model in simulations of polymethylene. *Journal of Chemical Physics*, 98:10037–10043, 1993.

[99] G.D. Smith, D.Y. Yoon, W. Zhu, and M.D. Ediger. Comparison of equilibrium and dyanamic properties of polymethylene melts of n-$C_{44}H_{90}$ chains from simulations and experiments. *Macromolecules*, 27:5563–5569, 1994.

[100] G.D. Smith, D.Y. Yoon, and R.L. Jaffe. Long-time molecular motions and local chain dynamics in n-$C_{44}H_{90}$ melts by molecular dynamics simulations. *Macromolecules*, 28:5897–5905, 1995.

[101] J. Han, R.L. Jaffe, and D.Y. Yoon. Conformational characteristics of polymethylene chains in melts and in various phantom chains from explicit atom molecular dynamics simulations. *Macromolecules*, 30:7245–7252, 1997.

[102] G.D. Smith, W. Paul, D.Y. Yoon, A. Zirkel, J. Hendricks, D. Richter, and H. Schober. Local dynamics in a long-chain alkane melt from molecular dynamics simulations and neutron scattering experiments. *Journal of Chemical Physics*, 107:4751–4755, 1997.

[103] W. Paul, G.D. Smith, and D.Y. Yoon. Static and dynamic properties of a *n*-$C_{100}H_{202}$ melt from molecular dynamics simulations. *Macromolecules*, 30:7772–7780, 1997.

[104] J.D. Londono, B.K. Annis, A. Habenschuss, G.D. Smith, O. Borodin, C. Tso, E.T. Hsieh, and A.K. Soper. Hydrogen-hydrogen intermolecular structure of polyethylene in the melt. *Journal of Chemical Physics*, 110:8786–8791, 1999.

[105] L. Harnau, R.G. Winkler, and P. Reineker. Comment on 'Chain motion in an unentangled polyethylene melt: A critical test of the Rouse model by molecular dynamics simulations and neutron spin echo spectroscopy'. *Physical Review Letters*, 82:2408, 1999.

[106] D. Brown, J.H.R. Clarke, M. Okuda, and T. Yamazaki. A molecular dynamics study of chain configurations in *n*-alkane-like liquids. *Journal of Chemical Physics*, 100:1684–1692, 1994.

[107] A. van Zon and S.W. de Leeuw. Structural relaxations in glass forming poly(butadiene): A molecular dynamics study. *Physical Review E*, 58:R4100–R4103, 1998.

[108] P.V. Krishna Pant, J. Han, G.D. Smith, and R.H. Boyd. A molecular dynamics simulation of polyethylene. *Journal of Chemical Physics*, 99:597–604, 1993.

[109] R.H. Boyd, R.H. Gee, J. Han, and Y. Jin. Conformational dynamics in bulk polyethylene: A molecular dynamics simulation study. *Journal of Chemical Physics*, 101:788–797, 1994.

[110] R.H. Gee and R.H. Boyd. Conformational dynamics and relaxation in bulk polybutadienes: A molecular dynamics study. *Journal of Chemical Physics*, 101:8028–8038, 1994.

[111] Y. Jin, M. Pernice, and R.H. Boyd. MD simulations of bulk polymers beyond 10 ns using parallel computation on a workstation cluster. *Computational and Theoretical Polymer Science*, 6:9–13, 1996.

[112] R.H. Boyd. Glass transition temperatures from molecular dynamics simulations. *Trends in Polymer Science*, 4:12–17, 1996.

[113] R.H. Gee and R.H. Boyd. Small penetrant diffusion in polybutadiene: A molecular dyanmics simulation study. *Polymer*, 36:1435–1440, 1995.

[114] R.H. Boyd and P.V.K. Pant. Molecular packing and diffusion in polyisobutylene. *Macromolecules*, 24:6325–6331, 1991.

[115] P.V.K. Pant and R.H. Boyd. Molecular dynamics simulation of diffusion of small penetrants in polymers. *Macromolecules*, 26:679–686, 1993.

[116] J. Han and R.H. Boyd. Small-molecule penetrant diffusion in hydrocarbon polymers as studied by molecular dynamics simulation. *Macromolecules*, 27:5365–5370, 1994.

[117] M. Mondello, G.S. Grest, A.R. Garcia, and B.G. Silbernagel. Molecular dynamics of linear and branched alkanes: Simulations and nuclear magnetic resonance results. *Journal of Chemical Physics*, 105:5208–5215, 1996.

[118] S.T. Cui, P.T. Cummings, and H.D. Cochran. The calculation of the viscosity from the autocorrelation function using molecular and atomic stress tensors. *Molecular Physics*, 88:1657–1664, 1996.

[119] S.T. Cui, P.T. Cummings, and H.D. Cochran. The calculation of viscosity of liquid *n*-decane and *n*-hexadecane by the Green-Kubo method. *Molecular Physics*, 93:117–121, 1998.

[120] K.S. Kostov, K.F. Freed, E.B. Webb III, M. Mondello, and G.S. Grest. Dynamics of linear and branched alkane melts: Molecular dynamics test of theory for long time dynamics. *Journal of Chemical Physics*, 108:9155–9167, 1998.

[121] J.K. Maranas, M. Mondello, G.S. Grest, S.K. Kumar, P.G. Debnedetti, and W. Graessley. Liquid structure, thermodynamics, and mixing behavior of saturated hydrocarbon polymers. 1. Cohesive energy density and internal pressure. *Macromolecules*, 31:6991–6997, 1998.

[122] J.K. Maranas, S.K. Kumar, P.G. Debnedetti, W. Graessley, M. Mondello, and G.S. Grest. Liquid structure, thermodynamics, and mixing behavior of saturated hydrocarbon polymers. 2. Pair distribution functions and the regularity of mixing. *Macromolecules*, 31:6998–7002, 1998.

[123] J.D. Londono, J.K. Maranas, M. Mondello, A. Habenschuss, G.S. Grest, P.G. Debenedetti, W.W. Graessley, and S.K. Kumar. Chain-packing effects in the thermodynamics of polymers. *Journal of Polymer Science: Part B: Polymer Physics*, 36:3001–3005, 1998.

[124] J.K. Maranas, M. Mondello, G.S. Grest, S. Kumar, P.G. Debenedetti, and W.W. Graessley. A molecular dynamics study of intermolecular structure, thermodynamics, and miscibility in hydrocarbon polymers. *Computers in Chemical Engineering*, 22:S19–S26, 1998.

[125] C.J. Mundy, J.I. Siepmann, and M.L. Klein. Calculation of the shear viscosity of decane using a reversible multiple time-step algorithm. *Journal of Chemical Physics*, 102:3376–3380, 1995.

[126] P.T. Cummings and T.L. Varner, Jr. Nonequilibrium molecular dynamics calculation of the shear viscosity of liquid water. *Journal of Chemical Physics*, 89:6391–6398, 1988.

[127] S. Toxvaerd. Molecular dynamics of liquid butane. *Journal of Chemical Physics*, 89:3808–3813, 1988.

[128] P. Padilla and S. Toxvaerd. Self-diffusion in *n*-alkane fluid models. *Journal of Chemical Physics*, 94:5650–5654, 1991.

[129] P. Padilla and S. Toxvaerd. Structure and dynamical behavior of fluid *n* alkanes. *Journal of Chemical Physics*, 95:509–519, 1991.

[130] D.K. Dysthe, A.H. Fuchs, and B. Rousseau. Fluid transport properties by equilibrium molecular dynamics. I. Methodology at extreme fluid states. *Journal of Chemical Physics*, 110:4047–4059, 1999.

[131] D.K. Dysthe, A.H. Fuchs, B. Rousseau, and M. Durandeau. Fluid transport properties by equilibrium molecular dynamics. II. multicomponent systems. *Journal of Chemical Physics*, 110:4060–4067, 1999.

[132] R.L. Rowley and J.F. Ely. Non-equilibrium molecular dynamics simulations of structured molecules. Part I. Isomeric effects on the viscosity of butanes. *Molecular Physics*, 72:831–846, 1991.

[133] R.L. Rowley and J.F. Ely. Non-equilibrium molecular dynamics simulations of structured molecules. Part II. Isomeric effects on the viscosity of models for *n*-hexane, cyclohexane, and benzene. *Molecular Physics*, 75:713–730, 1992.

[134] R.L. Rowley and J.F. Ely. Nonequilibrium molecular dynamics simulations of *n*-butane and isobutane viscosity. *Molecular Simulation*, 7:303–323, 1991.

[135] S.H. Lee and P.T. Cummings. The rheology of *n*-butane and *i*-butane by non-equilibrium molecular dynamics simulations. *Molecular Simulation*, 16:229–247, 1996.

[136] A. Berker, S. Chynoweth, U.C. Klomp, and Y. Michopoulos. Non-equilibrium molecular dynamics (NEMD) simulations and the rheological properties of liquid *n*-hexadecane. *Journal of the Chemical Society Faraday Transactions*, 88:1719–1725, 1992.

[137] S. Chynoweth, R.C. Coy, and Y. Michopoulos. Simulated non-Newtonian lubricant behavior under extreme conditions. *Proceedings of the Institution of*

Mechanical Engineers, Part J Journal of Engineering Tribology, 209:243–254, 1995.

[138] J.H.R. Clarke and D. Brown. The rheological properties of liquids composed of flexible chain molecules: A molecular dynamics computer simulation study. *Journal of Chemical Physics*, 86:1542–1547, 1987.

[139] R. Edberg, G.P. Morriss, and D.J. Evans. Rheology of n-alkanes by nonequilibrium molecular dynamics. *Journal of Chemical Physics*, 86:4555–4570, 1987.

[140] S. Chynoweth, U.C. Klomp, and Y. Michopoulos. Comment on: Rheology of n-alkanes by nonequilibrium molecular dynamics. *Journal of Chemical Physics*, 95:3024–3025, 1991.

[141] P.J. Daivis, D.J. Evans, and G.P. Morriss. Computer simulation study of the comparative rheology of branched and linear alkanes. *Journal of Chemical Physics*, 97:616–627, 1992.

[142] P.J. Daivis and D.J. Evans. Comparison of constant pressure and constant volume nonequilibrium simulations of sheared model decane. *Journal of Chemical Physics*, 100:541–547, 1994.

[143] C.J. Mundy, J.I. Siepmann, and M.L. Klein. Decane under shear: A molecular dynamics study using reversible NVT-SLLOD and NPT-SLLOD algorithms. *Journal of Chemical Physics*, 103:10192–10200, 1995.

[144] S.T. Cui, P.T. Cummings, and H.D. Cochran. Multiple time step nonequilibrium molecular dynamics simulation of the rheological properties of liquid n-decane. *Journal of Chemical Physics*, 104:255–262, 1996.

[145] P. Padilla and S. Toxvaerd. Fluid n-decane undergoing planar Couette flow. *Journal of Chemical Physics*, 97:7687–7694, 1992.

[146] K.P. Travis, D. Brown, and J.H.R. Clarke. A direct method of determining the coupling between internal molecular motions and transport properties: Application to liquid n-butane. *Journal of Chemical Physics*, 98:1524–1530, 1993.

[147] M. Lahtela, T.A. Pakkanen, and R.L. Rowley. Nonequilibrium molecular dynamics simulations of 3-methylhexane: The effect of inter- and intramolecular potential models on simulated viscosity. *Journal of Physical Chemistry A*, 101:3449–3453, 1997.

[148] W. Allen and R.L. Rowley. Predicting the viscosity of alkanes using nonequilibrium molecular dynamics : Evaluation of intermolecular potential models. *Journal of Chemical Physics*, 106:10273–10281, 1997.

[149] G. Kaminski, E.M. Duffy, T. Matsui, and W.L. Jorgensen. Free energies of hydration and pure liquid properties of hydrocarbons from the OPLS all-atom model. *Journal of Physical Chemistry*, 98:13077–13082, 1994.

[150] P. van der Ploeg and H.J. Berendsen. Molecular dynamics simulation of a bilayer membrane. *Journal of Chemical Physics*, 94:3271–3276, 1982.

[151] K.P. Travis, P.J. Daivis, and D.J. Evans. Thermostats for molecular fluids undergoing shear flow: Application to liquid chlorine. *Journal of Chemical Physics*, 103:10638–10651, 1995.

[152] S.T. Cui, P.T. Cummings, H.D. Cochran J.D. Moore, and S.A. Gupta. Nonequilibrium molecular dynamics simulation of the rheology of linear and branched alkanes. *International Journal of Thermophysics*, 19:449–459, 1998.

[153] T. Vardag, N. Krager, and H.-D. Lüdemann. Temperature and pressure dependence of self diffusion in long liquid *n*-alkanes. *Berichte der Bunsen-Gesellschaft für Physikalische Chemie*, 95:859–865, 1991.

[154] P. Debye. *Polar Molecules.* Dover, 1929.

[155] B. Berne and R. Pecora. *Dynamic Light Scattering.* Wiley, 1976.

[156] H. Takeuchi and R.-J. Roe. Molecular dynamics simulation of local chain motion in bulk amorphous polymers. I. Dynamics above the glass transition. *Journal of Chemical Physics*, 94:7446–7457, 1991.

[157] M. Mondello and G.S. Grest. Viscosity calculations of *n*-alkanes by equilibrium molecular dynamics. *Journal of Chemical Physics*, 106:9327–936, 1997.

[158] W. Gleissle. Stresses in polymer melts at the beginning of flow instabilities (melt fracture) in cylindrical capillaries. *Rheologica Acta*, 21:484–487, 1982.

[159] W.-M. Kulicke and R. Kniewske. The shear viscosity dependence on concentration, molecular weight, and shear rate of polystyrene solutions. *Rheologica Acta*, 23:75–83, 1984.

[160] S. Chandrasekhar. *Liquid Crystals.* Cambridge University Press, 1992.

[161] P.G. de Gennes and J. Prost. *The Physics of Liquid Crystals.* Clarendon, 1993.

[162] J.C. Horton, G.L. Squires, A.T. Boothroyd, L.J. Fetters, A.R. Rennie, C.J. Glinka, and R.A. Robinson. Small-angle neutron scattering from star-branched polymers in the molten state. *Macromolecules*, 22:681–686, 1989.

[163] A.T. Boothroyd, A.R. Rennie, and C.B. Boothroyd. Direct measurement of the temperature dependence of the unperturbed dimensions of a polymer. *Europhysics Letters*, 15:715–719, 1991.

[164] B.P. Williamson, K. Walters, T.W. Bates, R.C. Coy, and A.L. Milton. The viscoelastic properties of multigrade oils and their effect on journal-bearing characteristics. *Journal of Non-Newtonian Fluid Mechanics*, 73:115–126, 1997.

[165] P.T. Cummings, B.Y. Wang, D.J. Evans, and K.J. Fraser. Nonequilibrium molecular dynamics calculation of self-diffusion in a non-Newtonian fluid subject to a Couette strain field. *Journal of Chemical Physics*, 94:2149–2158, 1991.

[166] S. Matsuoka and T.K. Kwei. in *Macromolecules. An Introduction to Polymer Science,* F.A. Bovey and F.H. Winslow, eds., page 347. Academic Press, 1979.

[167] A. Baranyai and P.T. Cummings. Steady state simulation of planar elongation flow by nonequilibrium molecular dynamics. *Journal of Chemical Physics*, 110:42–45, 1999.

[168] B.D. Todd and P.J. Daivis. Nonequilibrium molecular dynamics simulations of planar elongational flow with spatially and temporally periodic boundary conditions. *Physical Review Letters*, 81:1118–1121, 1998.

[169] B.D. Todd and P.J. Daivis. A new algorithm for unrestricted duration nonequilibrium molecular dynamics simulations of planar elongational flow. *Computer Physics Communications*, 117:191–199, 1999.

[170] A.M. Kraynik and D.A. Reinelt. Extensional motions of spatially periodic lattices. *International Journal of Multiphase Flow*, 18:1045–1059, 1992.

[171] S. Sarman, D.J. Evans, and A. Baranyai. Mutual and self-diffusion in fluids undergoing strong shear. *Physical Review A*, 46:893–902, 1992.

[172] W.C. Sandberg and D.M. Heyes. Self-diffusion in equilibrium and sheared liquids. *Molecular Physics*, 85:635–649, 1995.

[173] A. Baranyai and P.T. Cummings. Self-diffusion in strongly driven flows: a non-equilibrium molecular dynamics study. *Molecular Physics*, 86:1307–1314, 1995.

[174] D.L. Malandro and D.J. Lacks. Molecular-level mechanical instabilities and enhanced self-diffusion in flowing liquids. *Physical Review Letters*, 81:5576–5579, 1998.

[175] H.F. Trotter. On the product of semi-groups of operators. *Proceedings of the American Mathematical Society*, 10:545–551, 1959.

APPENDIX

Self diffusion in a Couette strain field

Molecular simulation calculations of self-diffusion coefficients under equilibrium conditions are usually performed either in terms of mean squared displacements and the Einstein relation or velocity autocorrelation functions and the Green-Kubo relation. When the former method is employed for chain systems, the self-diffusion coefficient is calculated in terms of the limiting slope of the mean squared displacement (MSD) of the chain centers of mass as a function of time based on the Einstein relation

$$2tD = \frac{1}{3}\langle|\vec{r}_i(t) - \vec{r}_i(0)|^2\rangle \tag{A.1}$$

where D is the self-diffusion coefficient and $\vec{r}_i$ is the position of the center of mass of molecule i. The notation $\langle ... \rangle$ is indicative of the fact that the MSD is averaged over all the molecules in the system as well as many different time origins and corresponding initial positions $\vec{r}_i(0)$. For the case of diffusion in a flow field, this approach is

inadequate since both diffusion and convection will affect the MSD. Cummings *et al.* [165] derived Einstein and Green-Kubo relations for self-diffusion in a Couette strain field. They introduced the quantity $\vec{q}_i(t)$ defined by

$$\frac{d\vec{q}_i}{dt} = \frac{\vec{p}_i}{m}, \quad \vec{q}_i(0) = \vec{r}_i(0) \tag{A.2}$$

where, physically, the vector $\vec{q}_i$ describes the unconvected position of molecule i (compare Equation A.2 with the equation of motion for $\vec{r}_i$ Equation 3.10). The y and z components of $\vec{q}_i$ are the same as the y and z components of $\vec{r}_i$, but the x components differ by the integrated streaming velocity. Cummings *et al.* derived the following Einstein relations:

$$\langle \Delta q_x^2(t) \rangle = 2D_{xx}t \tag{A.3}$$

$$\langle \Delta y^2(t) \rangle = 2D_{yy}t \tag{A.4}$$

$$\langle \Delta z^2(t) \langle = 2D_{zz}t \tag{A.5}$$

$$\langle \Delta q_x(t) \Delta y(t) \rangle = (D_{xy} + D_{yx})t. \tag{A.6}$$

Cummings and coworkers studied the LJ fluid at its triple point and observed substantial shear-enhanced diffusion in all three directions [165]:

$$\frac{D_{xx}(\dot{\gamma}^* = 1)}{D(\dot{\gamma}^* = 0)} = 2.2 \tag{A.7}$$

$$\frac{D_{yy}(\dot{\gamma}^* = 1)}{D(\dot{\gamma}^* = 0)} = 2.0 \tag{A.8}$$

$$\frac{D_{zz}(\dot{\gamma}^* = 1)}{D(\dot{\gamma}^* = 0)} = 1.8 \tag{A.9}$$

where $\dot{\gamma}^*=\dot{\gamma}(m\sigma^2/\epsilon)^{1/2}$. Several additional simulation studies of self-diffusion in atomic fluids under flow have been performed [171, 172, 173]. Malandro and Lacks [174] observed that shear strains cause the disappearance of local minima of the potential energy surface of the LJ fluid at its triple point, leading to mechanical instabilities and associated atomic displacements which gave rise to shear-enhanced self-diffusion. They observed the enhancement to decrease with increasing temperature and strain rate.

Implementing the formalism developed by Cummings and coworkers for the case of chain molecules, two methods are apparent: 1) integrate Equation A.2 for each atom individually and determine the center-of-mass positions and MSDs of each chain from the individual values of q_x, y, and z of its constituent atoms and 2) integrate Equation A.2 only for the center-of-mass of each chain, not each individual atom. In practical terms, calculation of the self-diffusion coefficients in a Couette strain field via the Einstein relations only adds one additional equation of motion (for q_x) which must be integrated. We chose to employ a fourth order predictor-corrector to integrate the equation for q_x, effectively using the multiple timestep algorithm used to integrate the sllod equations as a "black box" to provide the peculiar momenta necessary in Equation A.2.

VITA

Jonathan D. Moore was born in Winston-Salem, North Carolina, on August 11, 1972. He attended Lipscomb University in Nashville, Tennessee, from August, 1990 until May, 1994, earning a Bachelor of Science degree in Engineering Science with minors in Mathematics and Chemistry. He enrolled in the University of Tennessee in August of 1994 and received his doctoral degree in Chemical Engineering in December, 1999.